Trajectory features as surrogate measures of the nanoparticle-microenvironment interaction space

Chad Curtis

A dissertation
submitted in partial fulfillment of the
requirements for the degree of

Doctor of Philosophy

University of Washington

2019

Reading Committee:

Elizabeth Nance, Chair

Cole DeForest

David Beck

Program Authorized to Offer Degree:
Chemical Engineering

University of Washington

Abstract

Trajectory features as surrogate measures of the nanoparticle-microenvironment interaction space

Chad Curtis

Chair of the Supervisory Committee:
Elizabeth Nance
Chemical Engineering

"The use of nanoparticle platforms in the field of medicine as diagnostic tools and therapeutic agents has been a long-promised hope. Despite some successes, including FDA approval of micelle and liposomal formulations for the delivery of strongly hydrophobic anticancer drugs, the translation of these technologies has slowed; in 1995, the ratio of animal studies to FDA-approved drugs was 19:1 and the ratio of animal studies to clinical studies was 7:1. Fifteen years later in 2010, the ratio of animal studies to FDA-approved drugs was 4000:1, and the ratio of animal studies to clinical studies was 120:1. There are many factors contributing to the slow in translation of nanotherapeutic technologies including bottlenecks in funding and the number of researchers trained in translational and clinical studies. But there are some upstream causes that need to be addressed prior to consideration of clinical trials. In this dissertation, I focus on two in particular: a limited knowledge of nanoparticle-environment interactions at the cell, tissue, and organ levels; and the slowness of existing screening tools to identify potentially successful nanoformulations.

This dissertation presents a number of tools that can be used to inform systems-level models of drug-environment interactions and improve the screening of drug candidates. Using *in vitro* and *ex vivo* models we demonstrate that nanoparticle colloidal stability can be used as a screening tool for nanoparticle therapeutics to the brain. We also demonstrate the use of trajectory datasets collected via fluorescent microscopy and multiple particle tracking to distinguish nuanced aspects of the

nanoparticle-microenvironment interaction space using neural networks, including protein adhesion and nanoparticle cell uptake. We apply similar methods to investigate the role of key nanoparticle features (surface functionality, PEG grafting density, PEG chain length) in determining *in vitro* and *ex vivo* transport behavior. This method of analysis highlights the potential of nanoparticles to be used both as pre-clinical diagnostic probes without the use of complex chemistries and to guide nanoparticle design for therapeutic interventions. ”

Table of Contents

List of Figures

List of Tables

Acknowledgments

”I am grateful for the chance to reflect on ‘each life that touches ours for good.’ I am here because of the mentors, the friends, the examples, and the belief each had in me, and it humbles me as I turn my thoughts towards each of you.

First, I would like to thank each of the members of my supervisory committee– Elizabeth Nance (chair), Cole DeForest, David Beck, Ariel Rokem, and Gary Goldbaum. The mentorship through the various phases of my graduate program has been invaluable.

Thank you to every member of Nance lab for our shared time together in a common enterprise. Nance lab aspires to be a family, and we really have built one. It means a lot to have a shoulder to cry on when experiments fail, or I just need to vent about the woes of paper revisions and method development. I want to particularly thank my fellow graduate students Rick Liao, Mengying Zhang, Mike McKenna, and Andrea Joseph. Defining a new lab and bringing it to life together has been powerful and seeing you each of you grow and be more confident is an inspiration. Thank you to Dorsa Toghani, Evan Epstein, and Hugo Pontes my ever-patient undergraduate mentees for their long hours on the DLS and confocal. I am going to miss our little team, and I look forward to seeing your own career paths develop!

Thank you, Elizabeth Nance, for always being the optimist when I feel my experiments are a mess, for being more than a mentor but a friend, and for getting me through the times I most felt like throwing in

the towel. We brag about you all the time, and we are proud of our fearless leader. Talking everything from an exciting new paper, to the latest book (or 5) you read this week, to your favorite German chocolate, to a new tangential idea from a conference or class that we could implement– your enthusiasm is a constant, and it is infectious. I aspire to your level of creativity and passion in my profession.

Lastly, thank you to my family for being my rock and constant support. Thank you to my parents, Dan and Angela, for loving me and reaching out to me even when I was distant or moody. I am proud of you both and glad to claim you as my own. Mom, you always said we are all our own kind of crazy, and you helped me embrace it. Dad, your quiet dignity and long-suffering has always impressed me, and I hope I can reflect some of that in my own character. My dear wife Jenni, I love you so much, and the trial that is graduate school has been an adventure that has helped us grow closer together. Your daily love and patience with me is a source of hope in the darkest days and a joy in the good. Chloe and Adelaide, I'll thank you too, because your smiles and the unconditional love you give are heaven-sent! Thank you to Roger and Barb, for putting up with us and all our idiosyncrasies in close quarters for 4 years (I hope the countless times I left the cutting board wet didn't drive you crazy!) "

Dedication

"To Jenni, Chloe, and Adelaide, with love"

Introduction

The use of nanoparticle platforms in the field of medicine as diagnostic tools and therapeutic agents has been a long-promised hope. Despite some successes including Food and Drug Administration (FDA) approval of micelle and liposomal formulations for the delivery of strongly hydrophobic anticancer drugs [1], the translation of these nanotechnologies has slowed. As shown in Figure 1, while the number of nanoparticle studies and nanoparticle studies using animal models have increased exponentially since the 90s, the number of studies entering clinical trials and the number of nanoparticle formulations approved by the FDA have not seen similar increases. In 1995, the ratio of animal studies to FDA-approved drugs was 19:1 and the ratio of animal studies to clinical studies was 7:1. Fifteen years later in 2010, the ratio of animal studies to FDA-approved drugs was 4000:1, and the ratio of animal studies to clinical studies was 120:1. There are many factors contributing to the slow in translation of nanotherapeutic technologies including bottlenecks in funding and the number of researchers trained in translational and clinical studies [2], as well as quality control considerations in scaling up nanoparticle synthesis [3]. But there are some upstream causes that need to be addressed prior to consideration of clinical trials: a limited knowledge of nanoparticle-environment interactions at the cell, tissue, and organ levels [4]; and the slowness of existing screening tools to identify potentially successful nanoformulations [3]. Because the design feature space of nanotherapeutics is so large, we either have to identify a rational method to narrow the search space (increase fundamental knowledge) or increase the speed at which we can test potential formulations (increase throughput). Improved models must take into account drug interactions at multiple levels of

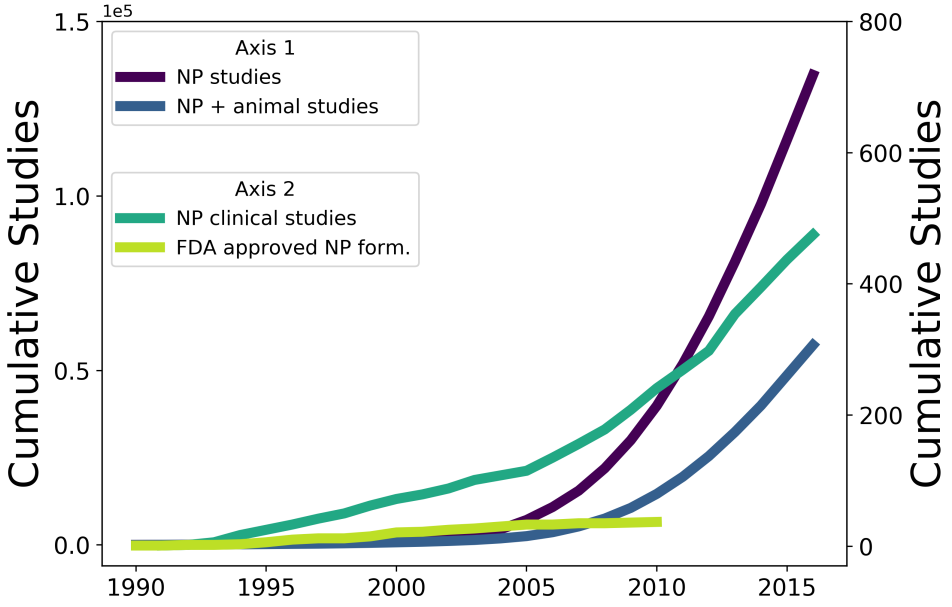

Figure 1: Cumulative nanoparticle-related publications over time in the biomedical and life sciences fields (Search terms: Nanoparticles (purple), Nanoparticles AND Animals[MeSH terms] (blue), Nanoparticles[clinical studies] (teal), FDA approved nanoparticle formulations (yellow-green)).

analysis (cell, tissue, organ, organ system), and can be guided by theoretical, computational, and machine learning approaches. Ideally, improved screening methods could be modelled on the directed evolution approaches of enzyme and protein engineering [5]. Recent advances include the use of microfluidics devices to test libraries of particle formulations simultaneously in *in vivo* like conditions [6], and barcoded nanoparticles to measure nucleic acid delivery of dozens of distinct nanoparticles at once [7]. The field of machine learning has additionally increased the power of screening studies by utilizing data that is normally thrown away to guide future iterations in the design process.

In this introduction we will review advances in two approaches to accelerating the translation of nanoparticle therapeutics: the systems approach to rational design, and the use of machine learning approaches in conjunction with nanoparticle trajectory datasets to evaluate nanoparticle transport properties.

0.1 Systems-level thinking for nanoparticle-mediated therapeutic delivery for brain diseases

Despite the significant financial investment we have made, we are still struggling to understand and adequately treat the majority of complex diseases. Neurological diseases account for 13% of the global burden of disease and cost roughly $750 billion a year to treat. Drugs that are used to treat the injured or diseased brain take 35% longer to be used in humans compared to drugs for any other type of disease [8]. Evaluating therapeutic interventions for a disease is difficult because the disease microenvironment is dynamic, heterogeneous, and variable from person to person. Delivering drugs to the diseased brain environment is also challenging, because the brain is protected by strictly regulated blood-brain barrier (BBB) and blood-cerebrospinal fluid (CSF) barriers, and has a complex microenvironment through which a therapeutic must move. Typically, less than 1% of a drug actually gets to the target organ, and often not just to the disease sites within the organ [9]. In addition, many drugs focus on suppressing one aspect of the disease, or have mechanisms that are complex and poorly understood, such that drug interactions within the body cannot be controlled or predicted. Administering more of a drug, or a cocktail of drugs, compensates for

the inefficiency in getting a drug to a target disease site, but both of these approaches may increase side effects and harm normal healthy tissue.

Nanoparticles, which consist of small (~1-100nm) tailorable platforms, can address some of the issues associated with ineffective drug delivery by increasing drug solubility [10], protecting drugs from clearance or from non-specific uptake [11], and by providing controlled or timed-release of a drug at the site of interest [1]. An increase in the development of nanoparticle-based drug delivery for the brain has yet to translate into a therapeutic standard of care in patients for any neurological disease, despite the fact that pre-clinical studies using nanotechnology overcome individual barriers to drug delivery to the brain, particularly the BBB. The growing body of data from pre-clinical and clinical trials necessitates a new approach to integrating information generated from brain-oriented fields (i.e. neuroscience, physiology, genetics, developmental biology, psychology, neurology, neurosurgery) with scalable technologies (i.e. via engineering, physics, chemistry, and materials science contributions) in a clinically relevant way.

An approach that integrates and applies information from a diverse array of fields requires systems-level thinking. The approach must account for an understanding of biological barriers to therapeutic intervention in the brain and an understanding and leveraging of nanoparticle material properties to overcome those barriers. Systems analysis is a problem-solving method that attempts to balance holistic and reductionist thinking paradigms. The systems analysis framework is based on parts of a system being best understood in the context of relationships with each other and with other systems, rather than parts of a system being evaluated in isolation. Given the genetic, lifestyle, and environmental complexity of the human race, a systems approach is important in engineering nanoparticles for application in complex human diseases, like those of the brain.

Nanotechnology is a useful information-gathering tool, therapeutic intervention, or diagnostic platform for applications in the brain. By using nanoparticles to probe the brain, it is possible to learn and quantify how accessible the brain is to a therapy in the context of each disease, and how readily a therapy can move to the diseased cells once in the brain. Both the nanomaterial contributions and the physiological contributions play a role in therapeutic outcome, and therefore do not function in isolation. For example, it is important to understand the aspects of a brain disease, i.e. BBB impairment and cell activation, that in-

fluence the ability of a nanoparticle to deliver a drug to a target cell. Greater BBB impairment can increase nanoparticle passage across the BBB into the brain parenchyma. However, increased phagocytic behavior of activated microglia in the injured brain can scavenge nanoparticles out of the brain parenchyma once the nanoparticle is across the BBB [12, 13], limiting uptake into other cells associated with a disease. It is equally important to evaluate how nanoparticle size and surface charge can lead to increased uptake across the impaired BBB, and alter cell specific uptake once in the brain.

To take into account multiple interacting aspects of physiology and nanomaterial properties, we can use a systems perspective to map and design nanotechnology platforms to treat neurological diseases. The next section will present physiological barriers to drug delivery in the brain and common neurological disease hallmarks that influence these barriers. Synthesis of pathophysiological barriers and nanoparticle physicochemical properties into a broader systems view creates an integrated approach to future work using nanotechnology to treat neurological diseases.

0.1.1 Physiological barriers to nanoparticle delivery in the brain

The brain is a complex organ that regulates respiration, motor control, memory, sleep, behavior, and how we relate to and interpret our environment. When the brain becomes sick or injured, the extent of damage and functional outcome are variable and heterogeneous, both within the brain itself and across species. Injury in the brain is often diffuse, in many cases affecting more than one region of the brain and more than one brain cell type. As humans age, the brain also deteriorates naturally, making us more susceptible to certain neurological disorders [14]. For delivery to the brain, a nanoparticle must be able to (i) avoid rapid clearance by the reticuloendothelial system (RES) and (ii) bypass or cross the BBB (Figure 2A). Once in the brain parenchyma, regardless of the administration route, a nanoparticle must (iii) penetrate within the brain microenvironment to reach diffuse disease sites, and (iv) provide intra- or extracellular release of the therapeutic agent at the site of disease (Figure 2A-C). Common disease hallmarks affect each of the aforementioned barriers. These disease hallmarks include extracellular matrix (ECM) changes [15, 16], inflammation [17, 18], oxidative stress [14, 19, 20], excitotoxicity [21, 22], cell death [23, 24], and impaired

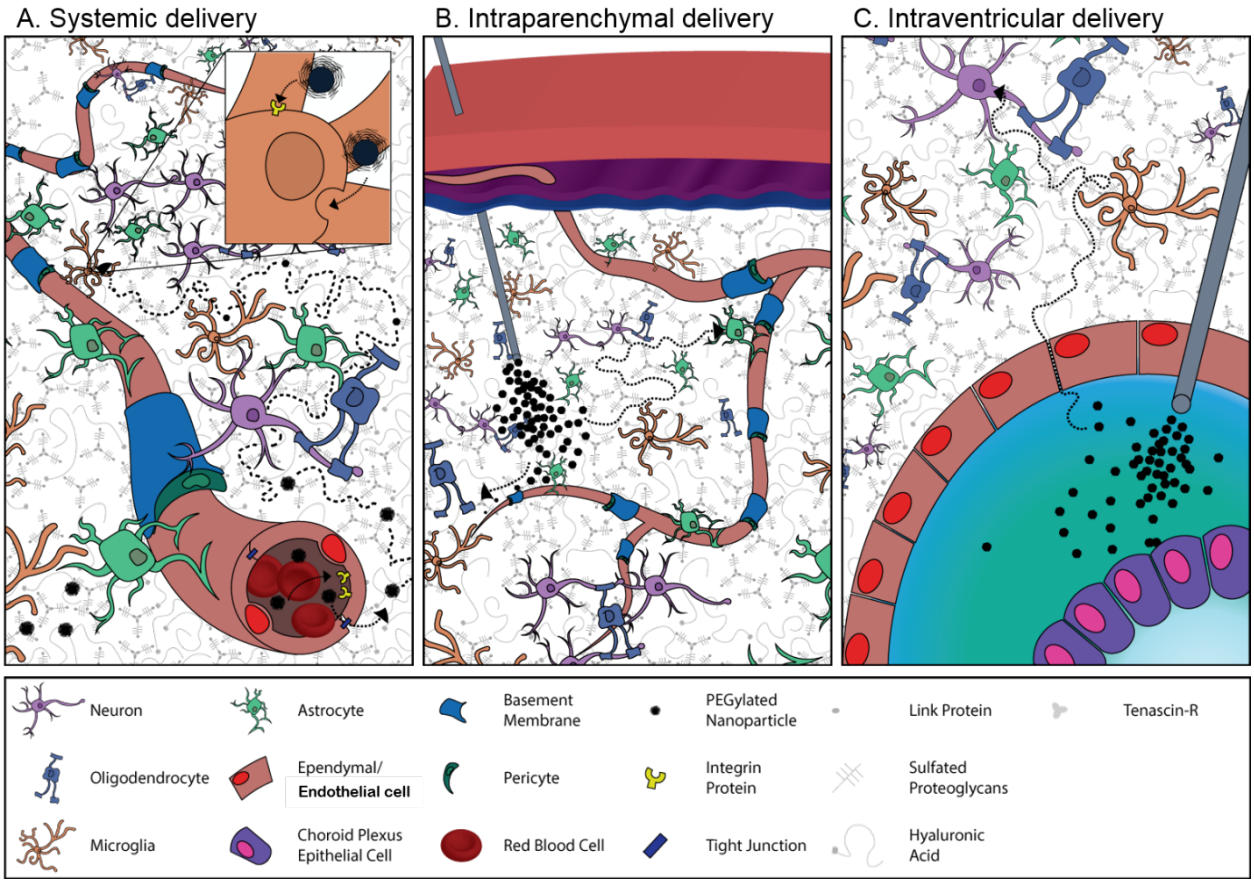

Figure 2: Barriers to nanoparticle delivery to the brain. For a nanoparticle-based therapeutic delivery system to be effective in the brain, it must be able to overcome the system of barriers in the brain. (A) Following systemic administration, a nanoparticle must avoid rapid clearance by the RES and bypass or cross the BBB. A nanoparticle can cross the BBB via receptor-mediated transcytosis or permeation across impaired tight junctions. The nanoparticle must then navigate the brain microenvironment by avoiding steric or adhesive interactions with the ECM, to reach diffuse disease sites. The nanoparticle must then provide site-specific delivery to diseased cells, either extracellularly or after internalization via non-specific fluid phase endocytosis, phagocytosis, or receptor-mediated cellular transport (inset). (B) Following local delivery, a nanoparticle must still navigate the ECS and ECM, avoid clearance along the PVS or into the ventricles, and then provide site-specific therapeutic action at a diseased cell. (C) A nanoparticle delivered directly into the CSF, i.e. intraventricular, will need to cross the ependymal layer, although this mechanism remains largely unknown, and navigate the ECS and ECM to reach target cells.

fluid flow [25, 26], which are present in almost all neurological diseases to varying extents.

0.1.1.1 Common disease hallmarks in neurological disease

Pathophysiology influences the BBB, the brain microenvironment, and cell-specific behavior, and these vary from disease to disease and across individuals with the same clinically defined disease. A systems-level perspective of how disease hallmarks can influence each barrier to nanoparticle delivery in the brain (Figure 3) can help understand how nanoparticle-based therapeutics can overcome these barriers to decrease disease burden. For example, inflammation, oxidative stress, cell death, and excitotoxicity change the brain microenvironment by increasing cell debris within the ECS, disrupting BBB function and integrity, and altering the composition and structural geometry of the ECM [27–29]. These disease hallmarks are present in cancer, acute neurological injury, neurodegenerative disease, neuropsychiatric and neurodevelopmental disease, and in CNS infection. In primary brain cancers, such as malignant gliomas (MG), medulloblastomas, and oligodendrocytomas, changes in BBB permeability and an overproduction of ECM components are seen, as well as increased inflammation, macrophage infiltration, and cell death [30]. These disease processes increase the tortuosity and decrease the volume fraction of the ECS. Increased interstitial pressure within the tumor microenvironment can also inhibit movement and distribution of a therapeutic within that environment [31]. This demonstrates the dynamic and interconnected nature of disease hallmarks that must be accounted for in nanotherapeutic design.

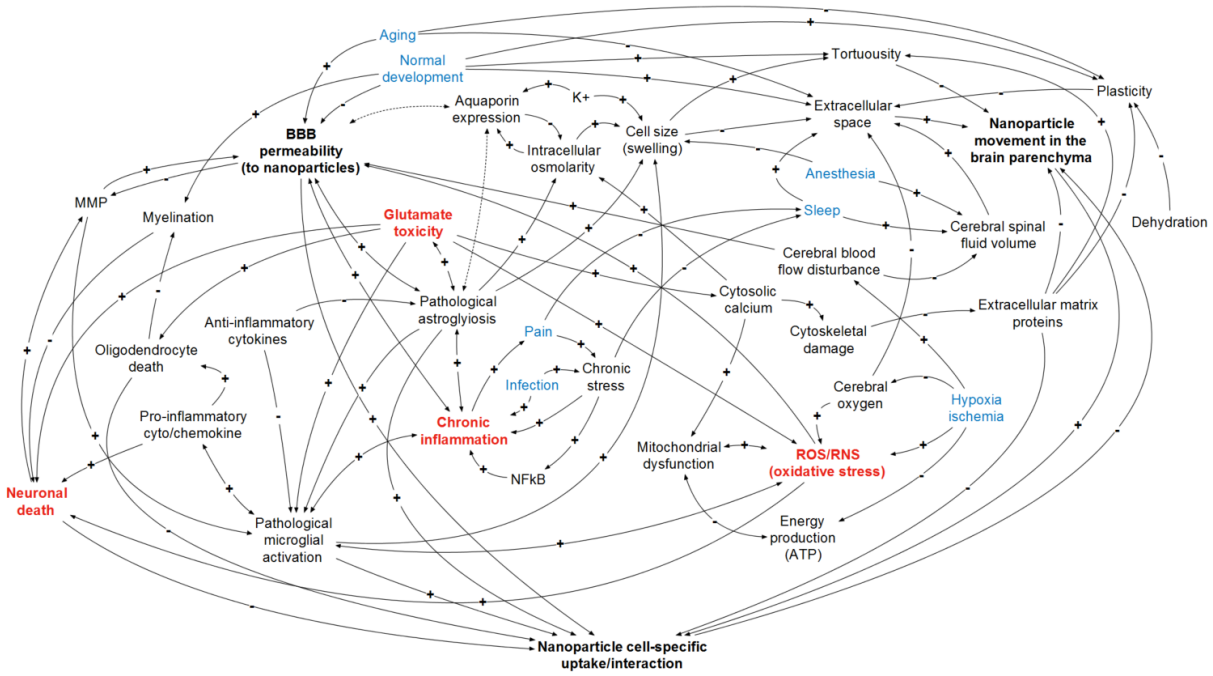

Figure 3: Neurophysiology and biology-based factors influencing nanoparticle delivery in the brain. The system of factors that change in the presence of an input (examples in blue) can positively or negatively impact common disease hallmarks (examples in red) and changes in BBB permeability, brain microenvironment, and cell behavior in the brain. These changes influence the ability of a nanoparticle to penetrate across the BBB, move within the brain parenchyma, and uptake into specific cells; however, as the map shows, none of the factors influencing nanoparticle delivery of a therapeutic can be viewed in isolation. Double-headed arrows indicate a two-way effect of similar directionality (i.e. pathological astrogliosis increases chronic inflammation, and chronic inflammation increases pathological astrogliosis). Abbreviations: ROS/RNS- reactive oxygen/nitrogen species; MMP- matrix metalloproteases; NMDA-N-methyl-D-aspartate.

0.1.2 Nanoparticle physicochemical properties for overcoming physiological CNS barriers

A variety of materials have been utilized for nanoparticle delivery to the brain, including dendrimers [32], polymers [33, 34], micelles [35], hydrogels [36], liposomes and solid lipids [37, 38], gold [39], silica [40], and silver-based inorganics [41], iron or iron oxides [42, 43], quantum dots [44], and carbon nanotubes [45, 46]. For each of these nanoparticle systems, important physicochemical characteristics that affect drug delivery and efficacy include size, surface charge, composition, molecular weight (MW), material structure, rigidity/elasticity, shape, and material porosity (Table 1). The combination of nanoparticle physicochemical properties influence absorption, distribution, metabolism, and excretion (ADME profiles) of these particles from the body [47]. In addition, the physicochemical nanoparticle properties will play a role in whether the nanoparticle can bypass the BBB, move through the brain microenvironment, and uptake into disease-specific cells, which directly influences therapeutic outcome and reduction of disease burden in the brain.

0.1.3 Synthesizing nanomaterial properties and pathophysiology hallmarks using systems-level thinking

Nanoparticle physicochemical properties and administration routes can be fine-tuned to leverage disease hallmarks to overcoming barriers in the brain. A variety of factors can determine or influence the therapeutic effect and impact on disease burden. Some factors are specific to the disease (etiology, developmental age at onset/injury, progression of the disease), and some factors are specific to susceptibility or risk of disease (genetics, environmental, diet, lifestyle, age). Regardless, common disease hallmarks, including ECM changes, inflammation, oxidative stress, excitotoxicity, cell death, and impaired fluid flow, are present in almost all neurological diseases, albeit to varying extents. The impact of these hallmarks must be taken into consideration when altering the design of a nanoparticle system to treat a certain disorder.

Rather than try to increase brain uptake in a purely iterative manner, which may result in poorer

Table 1: Examples of nanoparticle platforms and the most common physicochemical properties exhibited by nanoparticle platforms used for therapeutic delivery.

Nanoparticle	Core Material Examples	Size Range (nm)	Common Core Material Polarity	Common Shapes	Reported Young's Modulus (MPa)	Common Surface Functionalities or Coatings
Polymer	PLGA, PBCA, PLA	50-450	Hydrophobic	Spherical; wide range from PRINT or lithography techniques	3-110	Hydroxyl, carboxylate, amine acid, surfactants, PEG, zwitterions
Dendrimer	Polyamidiine, polylysine, phosphorus	1.5-14	Hydrophilic	Spherical/globular	150-700	Hydroxyl, carboxylate, amine acid (i.e. phosphoric, succicamic), PEG
Silica	Mesoporous silica	5-450	Hydrophilic	Spherical	<0.001	Carboxylate, amine, (phonsphonate, PEG, octadecyl)
Quantum dots	CdSe, ZnO, CdS, ZnS	2.0-10	Hydrophobic	Spherical, wires, rods	ZnO: $3.3x10^6$ CdSe: $1.3x10^5$	Thoils, carboxyl, PEG, methoxy, amine, mercaptopropanoic acid
Lipid (i.e. liposomes, solid-lipid (SLNs))	Phosphatidylcholine, phospholipids, cholesterol, fatty acids, waxes	50-400	Liposomes; amphipathic SLNs: Hydrophobic core	Spherical	Liposome: 2-10	Lipid end groups: triglycerides, cationic/anionic depending on composition PEG, gangliosides
Metallic	Silver, gold, iron, and iron oxides	Gold: 5-400 Silver: 1-100 Iron oxide: 4-100	Hydrophobic	Spherical, diamond	Gold: 2.5 - 1x 10^5	General: thiols, PEG; Gold: Mercapto(acetic, propionic, undecanoid, succinic) acid; Iron: galactose, mannose, folic acid
Carbon	Carbon nanotubes (CNT), fullerenes	<1-4 nm single dimension	Hydrophobic	CNTs: rod Fullerenes: Spherical cages	CNT: 0.40-4.2x 10^6	PEG, biotin, poly(vinyl pyrrolidone), esters SiO_2
Hydrogels	Chitosan, alginate, polyethylene oxides, PEG	10-1000	Hydrophilic	Spherical	15-42	Amine (chitosan), anionic (alginate), cationic/anionic depending on composition, tripolyphosphate (chitosan), polysaccharides

outcomes and slower progress, systems-level thinking maps the disease and the nanoparticle as part of the same dynamic environment. Tailoring nanoparticle properties to specific disease commonalties, i.e inflammation, in the brain could lead to more rapid and effective translation into the clinic. In brain diseases, particle properties must be fine-tuned to achieve uptake in the brain, distribution within the brain, and cell-specific interaction (Figure 4). By implementing a rational design process to nanotherapeutics, we can significantly reduce the overall search space of potential drug therapies. Considering the potential magnitude of such a search space, as explored in this review (e.g. size, surface functionality, core material), this will be key to avoid a flatline in nanotherapeutic development. In the next section, we will explore efforts to accelerate nanoparticle development in the form of increased screening tools. A complementary approach to narrowing the search space is speeding up the screening process. While there are many measures that should be monitored while developing nanotherapeutic delivery vehicles (e.g. release rates, percent activity), a key measure is nanoparticle transport properties. The next section explores advances in machine learning techniques in conjunction with multiple particle tracking datasets to increase the amount of information available to researchers from tracking studies.

0.2 Exploring the interface of trajectory datasets and machine learning in biomedical applications and the life sciences

Researchers in biomedical and life sciences fields are increasingly turning to single particle tracking (SPT) and multiple particle tracking (MPT) as a method of data collection. MPT techniques can be used to measure rheological properties [48], pore sizes [49], and other aspects of biological microenvironments. MPT can monitor and quantify the behavior of cellular receptors [50], organelles [51], viruses [52], and cells [53]. MPT has also been applied to quantify nanoparticle transport properties, a key characteristic in evaluating overall efficacy for nanotherapeutic platforms [54]. Using a variety of microscopy techniques, virtually any target of adequate size that can be labelled to distinguish it from background can be tracked to measure transport properties. MPT has become an essential component of the rational design

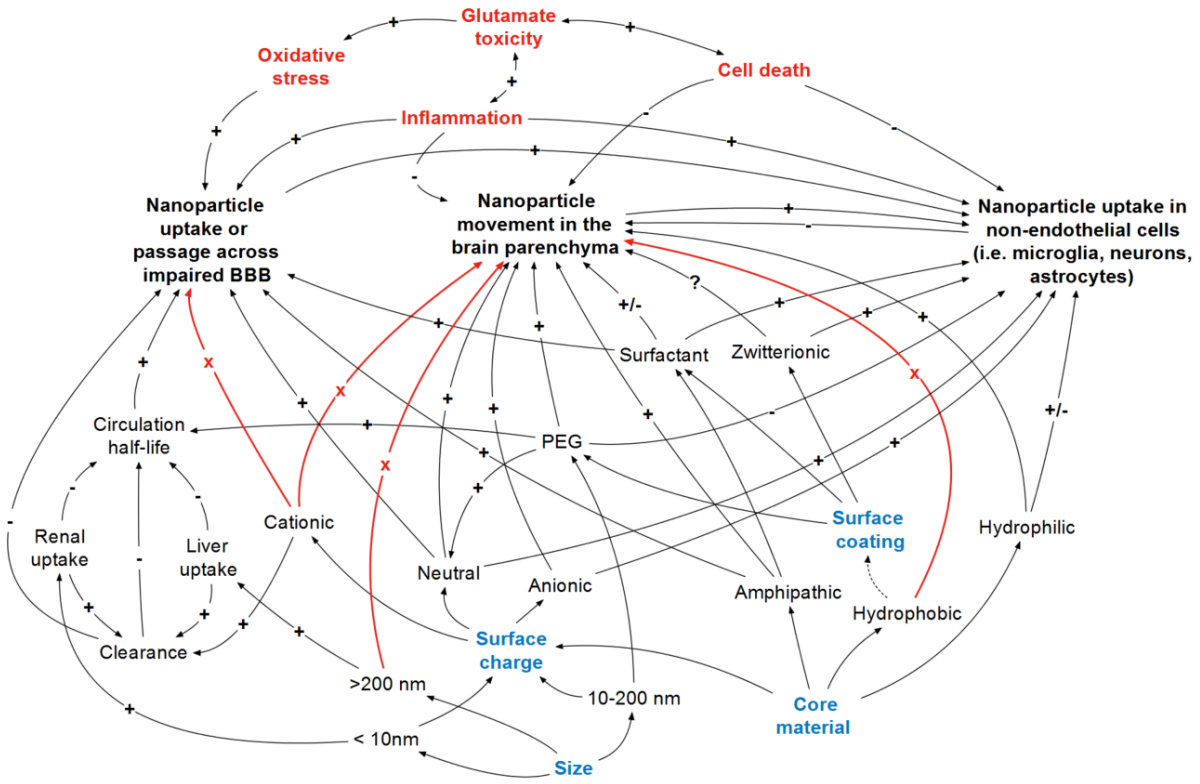

Figure 4: Predictive design mapping of nanoparticle behavior as a function of nanoparticle physicochemical properties to overcome barriers to therapeutic delivery in the brain. Nanoparticle physicochemical properties (blue), including size, core material, surface charge, and surface coating, can influence the behavior of the nanoparticle in the brain, specifically the ability of a nanoparticle to overcome barriers to therapeutic delivery. However, pathophysiological hallmarks (red) influence these barriers, potentially altering the nanoparticle behavior. By looking at the system of factors, both nanoparticle properties and disease hallmarks, nanoparticles can be designed to avoid dead ends (red arrows) that will prevent the particle from achieving a therapeutic effect in the brain. Additional factors, such as shape and particle stiffness, will also effect therapeutic delivery, but these are less well-studied in the brain.

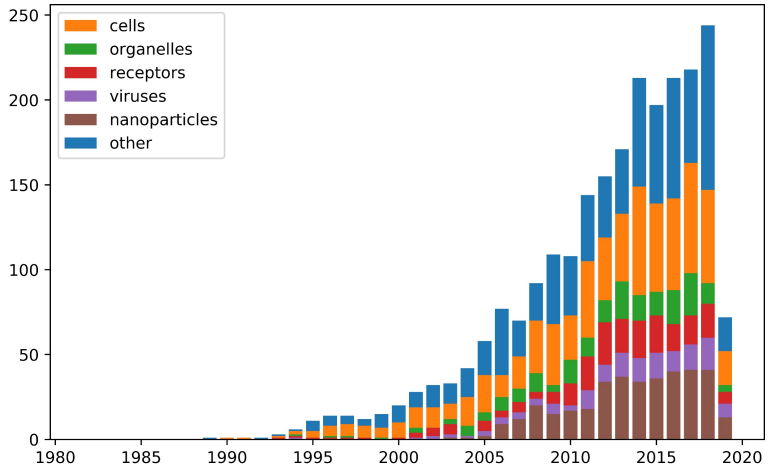

Figure 5: Literature search of biomedical publications implementing multiple particle tracking methods stratified by the object of interest (Orange: cells, Green: organelles, Red: receptors, Purple: viruses, Brown: nanoparticles, Blue: other).

of nanoparticle therapeutics and is increasingly leveraged to answer a wider variety of biomedical questions. We performed a literature review using PubMed to identify publications that have implemented particle tracking methods in biomedical and life sciences in the last 40 years, with search terms including ((("Microscopy, Video"[MeSH Terms]) AND ("Diffusion"[MeSH Terms])) OR "biological trajectories" OR "particle tracking"), and sorted the results by the unit of tracking (Figure 5). Of the 2375 papers implementing a tracking method, 15.6% were tracking nanoparticles, 28.3% cells, 9.7% cell receptors, 8.5% organelles, and 6.3% viruses. The number of papers published per year has increased from 11 papers in 1995 to 244 in 2018 (an increase of ~10 papers/year).

Despite the application of MPT to a variety of problems in biomedical fields, most papers share a common formula: MPT is used to quantify some magnitude of transport (e.g. diffusion coefficient), and an ensemble measure of central tendency is reported. In terms of the ratio of raw data to the amount reported and utilized, this is very inefficient. When researchers are collecting thousands to millions of trajectories in a single experiment and reporting a single scalar value or a single ensemble-averaged MSD profile, spatial and geometric information that does not directly contribute to the magnitude of transport is lost. However, machine learning is one toolset that can potentially be leveraged by researchers

to expand the utility of MPT datasets. Machine learning is a set of analytical tools to identify patterns and build models to describe datasets. Machine learning methods span in complexity and interpretability from simple 1D linear regression models to neural networks. James *et al.* provides an introduction and overview to machine learning methods[55]. When adding in the terms "machine learning", "classification", "data science", "random forest", "support vector machine", "regression", "neural network", and "supervised", or 30 (1.3%) of biomedical papers using MPT methods have implemented machine learning to analyze collected trajectory datasets.

In section 0.2, we will give an overview of the ways machine learning methods have been implemented using trajectory datasets in the biomedical and life sciences literature. We will provide a brief overview of novel machine learning techniques implementing trajectory datasets from the artificial intelligence and computer science fields and give suggestions about how these can be applied to trajectory datasets in biomedical applications, with particular emphasis on how these can be used to advances the screening of nanotherapeutic delivery vehicles.

0.2.1 Machine learning applied to trajectory datasets in the biomedical and life science fields

Existing use of machine learning methods with biological trajectory datasets is limited to a few use cases. The primary application classifies trajectories into their motion type. In terms of the mean-squared displacement (MSD), motion can be classified into the following types:

Table 2: Motion types and their mathematical representations

Motion type	Mean Squared Displacement
Brownian motion	$\langle r^2(n)\rangle = 4Dn\Delta t$
Anomalous diffusion	$\langle r^2(n)\rangle = 4D(n\Delta t)^a$
Directed motion	$\langle r^2(n)\rangle = 4Dn\Delta t + (vn\Delta t)^2$
Confined diffusion	$\langle r^2(n)\rangle = r_c^2[1 - A_1 e^{-4A_2 Dn\Delta t/r_c^2}]$

where $\langle r^2(n)\rangle$ is the mean squared displacement, D is the diffusion coefficient, n is the frame number, Δt is the frame speed, α is the anomalous exponent, v is the velocity, r_c is the radius of confinement, and A_1 and A_2 are shape constants [56]. Each motion type has a distinct shape, as shown in Figure 6. At the most basic level, classification by motion type can be applied algorithmically without any need for machine learning techniques. In one paradigm, a trajectory can be fit to each of the above motion models and classified based on the model with the best goodness of fit. This method was used by Li *et al.* to classify movements of secretory granules within cells into random, directed, and caged diffusion modes [57]. In a second paradigm, trajectories can be fit to one or two models and classified using user-defined thresholds on fitting parameters. Liu *et al.* classified trajectory segments based in their anomalous diffusion exponent and directional persistence [42]. Machine learning methods such as support vector machines (SVMs), random forests, and neural networks have also been used to classify trajectories by their motion type. In addition to different machine learning algorithms, each of these methods use different methods of determining input features of interest, training datasets, and output motion categories.

0.2.1.1 Support Vector Machines

In our first example, Helmuth *et al.* leverages a series of binary SVMs to classify the trajectory segments of virus particles within cells into five motion types: confined motion, slow drift, fast drift, and directed motion, and unclassified [58]. Each of these motions within cells occur due to interaction with cell com-

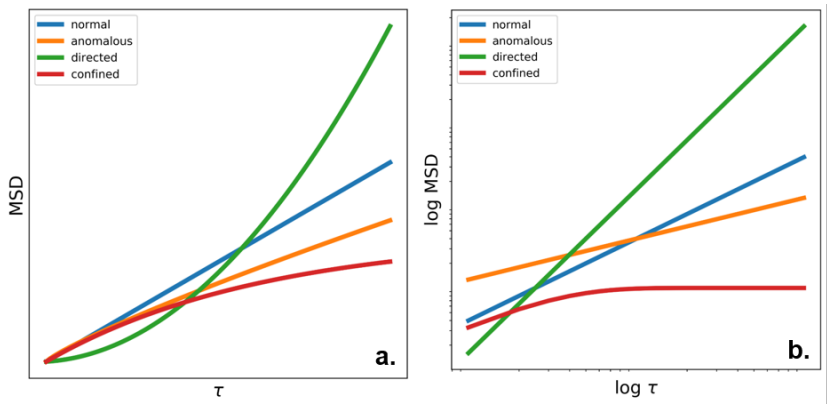

Figure 6: MSD profiles of normal diffusion, anomalous diffusion, directed motion, and confined diffusion on (a) a linear scale and (b) a log scale.

ponents. For instance, confined motion occurs due to receptor-ligand interactions causing immobilization, while fast drifting and directed motion occur when molecular motors drive virus motion. Brownian motion is lumped together with other types of motion into an unclassified category. These motion types mostly overlap with the classes of motion types described above: both confined and directed motion are present. The new categories, slow drift and fast drift, are variations of directed motion: both have a uniform velocity component of varied magnitude superimposed on an underlying diffusive component.

Helmuth's binary SVMs are based on seven geometric trajectory features (net displacement, straightness, bending, efficiency, asymmetry, point position skewness, and point position kurtosis), some of which are defined in Figure 7. Figure 7 demonstrates how geometric features vary between two extremes, a straight line and perfect circular motion, with directed, anomalous, and confined motion as intermediates. Helmuth *et al.* doesn't explain whether these features are exhaustive or how these were selected but does specify that features must not be dependent on rigid-body rotations and translations of entire trajectory parts. Similar sets of geometrical features are used in MPT machine learning applications, such as the set of nine features proposed by Wagner *et al.* used in random forests [56]. Helmuth *et al.* performs an exhaustive feature selection step by training each SVM classifier on each possible combination of features [58]. The classifier with the best performance is selected. The final classifiers implement 3-6 of the original seven features to predict motion type. These simpler models that have smaller parameter spaces reduce

model complexity and increase robustness of the resulting predictors.

0.2.1.2 Random Forests

In a second example, Wagner *et al.* performed an analysis of trajectory segments similar to Helmuth *et al.* using random forests instead of support vector machines [56, 58]. Trajectories of nanoparticles diffusing in lung fibroblast cell populations were classified by motion type into normal diffusion, anomalous diffusion, confined diffusion, and directed motion. These are a slightly different scheme than Helmuth et al.'s system of classification [58]. Wagner *et al.* distinguishes between sub-diffusive motion types: confined diffusion and anomalous diffusion [56]. Helmuth et al., on the other hand, distinguishes between 3 magnitudes of convective component motion: slow drift, fast drift, and directed motion [58]. These motion types were selected by a previous knowledge of the biological mechanisms involved. This is a good reminder that machine learning methods cannot be applied blindly, but must be accompanied by theoretical knowledge of the phenomena being observed. In addition to SVMs and random forests, neural networks have also been used to classify motion types of biological trajectory datasets [59].

0.2.2 Machine learning techniques from AI fields: Feature extraction methods

Trajectory datasets aren't limited to MPT nor are they unique to biomedical applications. The field of AI includes a rich variety of applications implementing machine learning algorithms to classify behavior based on trajectory data. In the following two sections, we will highlight a few of these methods and suggest how they can be applied to trajectory dataset in biomedical settings. In section 3, we will highlight a series of alternate feature extraction methods (e.g. feature selection, dimensionality reduction) that have been implemented on a variety of types of trajectory datasets. As trajectory datasets are highly dimensional (in practice, the number of features corresponding to the number of frames), finding a way to express the same information in a smaller dimensional space is usually necessary—not only for feasible computational

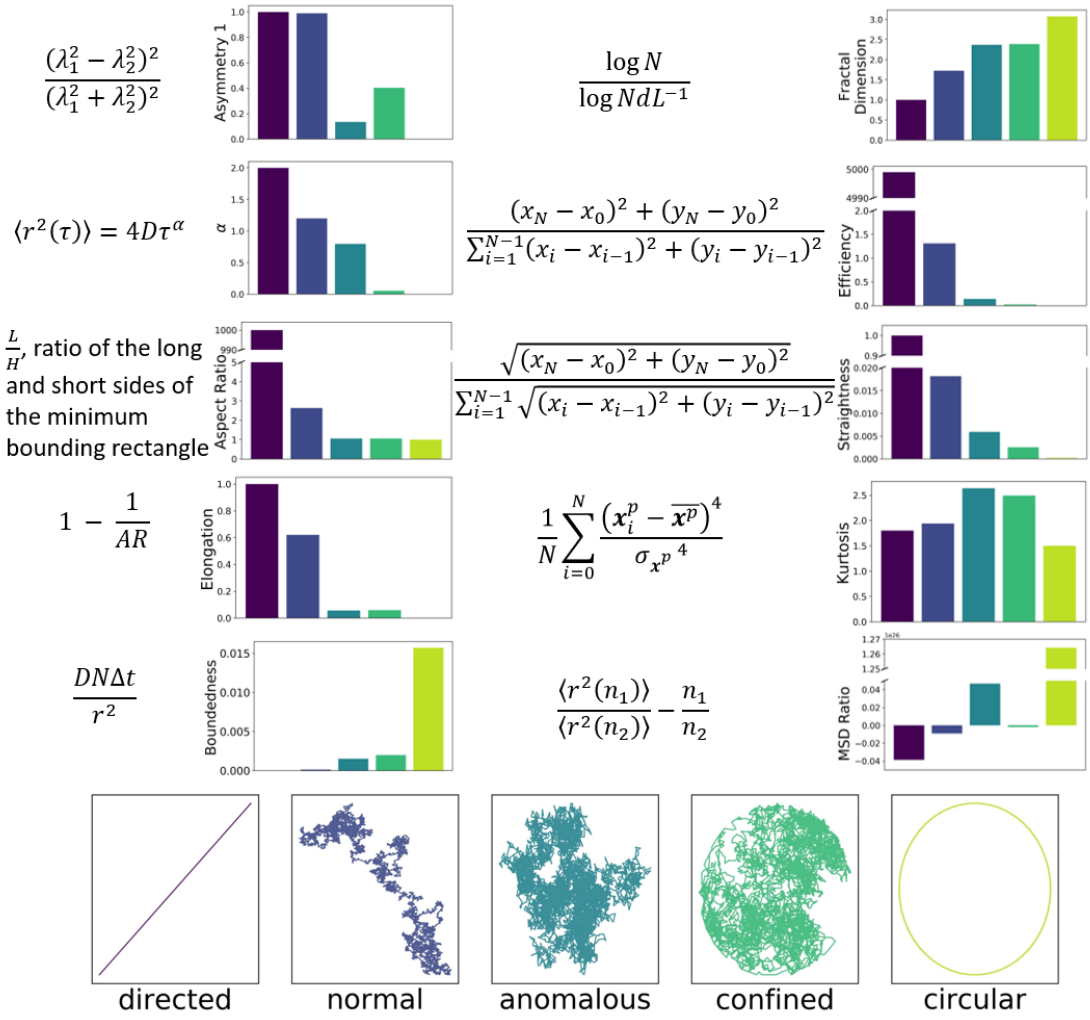

Figure 7: Definitions and conceptualization of geometric features. (a) Common geometric features used in trajectory machine learning methods including asymmetry, anomalous exponent, aspect ratio, elongation, boundedness, fractal dimension, efficiency, straightness, kurtosis, and MSD ratio; their definitions; and calculated values of the above geometric features for directed motion, normal diffusion, anomalous diffusion, confined diffusion, and circular motion. (b) Direction motion, normal diffusion, anomalous diffusion, confined diffusion, and circular motion trajectories on which the feature calculations in (a) were calculated.

times, but to address the "curse of dimensionality", the reduction in predictive power when the number of features increases due to poor sampling of the entire feature space [55]. For example, if 10^2 observations are adequate to sample a 1-dimensional feature space, then $(10^2)^2$ or 104 observations are required for a 2-dimensional feature space and $(10^2)^{30}$ or 1060 observations are required for a 30-dimensional feature space. Researchers have found creative ways of addressing this problem, as illustrated below.

0.2.2.1 Fourier transform for feature extraction

Naftel & Khalid demonstrate the importance of feature reduction when performing machine learning on trajectory datasets [60]. In theory, raw trajectory datasets could be fed directly into a machine learning model without any feature extraction step; where raw *xyz* coordinates are directly used as inputs. The drawback here is three-fold: first, using such a high-dimensional parameter space results in slow convergence times. Training such machine learning models becomes unfeasible very quickly. Second, the curse of dimensionality: large feature spaces result in sparse training datasets. At minimum, users must provide p+1 observations per *p* features (in this case, frames from a trajectory dataset), otherwise there isn't a unique solution. Third, including raw *xyz* information in a machine learning algorithm may not be desired. Algorithms should be location-blind, so that whether a particle happened to be farther left or farther right in the original frame of reference doesn't impact its predicted class.

In the papers cited in the previous section, this problem was usually solved by a number of scalar geometric transformations of the data (Figure 7). However, there is no guarantee that this approach comprehensively captures all aspects necessary to define motion types. As of now, there is very limited literature on choosing the best feature space for trajectory datasets. Naftel & Khalid highlight one method of solving this problem by using parametrization techniques. In this case, they suggest using the first four coefficients of the discrete Fourier transform as inputs to a machine learning model (Figure 8) [60]. Naftel & Khalid used this method to classify trajectories from three sources: Australian sign language videos, video surveillance footage from a shopping center, and real-time tracking data of lab members walking in the laboratory. Trajectories were classified using an unsupervised machine learning approach called a self-organizing map (SOM). When compared with a K-Nearest Neighbor (KNN) classifier using point-

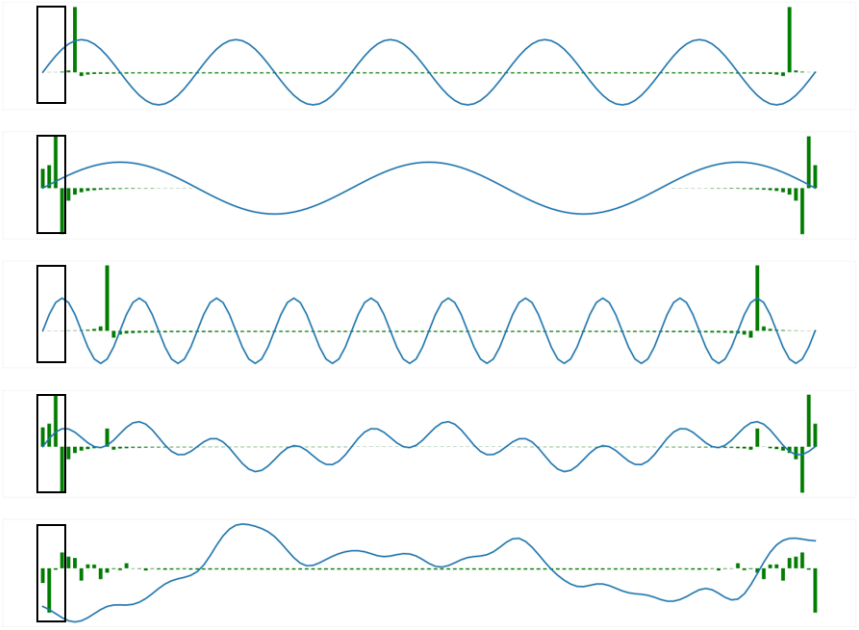

Figure 8: Example feature extraction using 1D Fourier transform on 1D trajectory datasets. Feature extraction with (a) sinusoidal curve, (b) sinusoidal curve with 0.5x frequency, (c) sinusoidal curve with 2x frequency, (d) sinusoidal curve with 0.5x and 2x frequencies superimposed on each other, and (d) random walker.

based inputs in the spatial domain, the SOM classifier using DFT inputs from the frequency domain proved superior, with an overall accuracy 93.7% compared to 83.0% from the KNN. The SOM method does have the disadvantage of excluding higher frequency information, but can be adjusted by increasing or decreasing the number of Fourier coefficients as appropriate for the given dataset. Implementing a feature subset selection method, such as LASSO regression, prior to training a neural network could home in on the frequencies most important in a given dataset. Similar parametrization techniques can be translated into biological settings to get improved classification accuracy. Alternate approaches include wavelet transformations [61], adaptive piecewise constant approximations [62], and Chebyshev polynomials [63].

0.2.2.2 Histogram of oriented displacements and temporal pyramids

Another novel approach of feature extraction from trajectory datasets was demonstrated by Gowayyed et al., who used the movement of joints to classify human movement into distinct actions [64]. Joint movements were captured from human subjects using a Kinect sensor. Gowayyed *et al.* used the Microsoft Research Action3D action classification system , which consists of twenty types: high arm wave, horizontal arm wave, hammer, hand catch, forward punch, high throw, draw x, draw tick, draw circle, hand clap, two hand wave, side-boxing, bend, forward kick, side kick, jogging, tennis swing, tennis serve, golf swing, pick up, and throw [65]. Each 3D trajectory of each joint was decomposed into three 2D trajectories in the *xy*, *xz*, and *yz* planes. Gowayyed *et al.* then assembled a set of features called a histogram of oriented displacements (HOD) by binning each step within the trajectory by its direction angle (Figure 9). The contribution of each step to the histogram is scaled by its length. As a raw HOD loses temporal information, a temporal pyramid is constructed by dividing the trajectory into a series of equally sized segments and constructing an HOD on each segment. The final feature dataset is a concatenation of each HOD from each segment. Using linear SVMs for classification, Gowayyed *et al.* report a classification accuracy of 91.3% in the test dataset using a 50-50% split, compared to a maximum accuracy of 88.2% accuracy using the state-of-the-art method using Multiple Kernel Learning [66]. Directionality can be vital information in joint classification because there is a shared frame of reference among datasets: up is up and down is down. However, this is not the case in most biological applications where camera orientation with respect to the sample is often arbitrary. Most methods of feature extraction used in biomedical applications examined in section 0.2 ignore directionality because there is no shared frame of reference. This method of feature extraction using histograms of oriented displacements can potentially be useful where directionality is important. For example, directionality could be important when tracking chemotaxis or other orientation-dependent cell migration behaviors or for tracking anisotropic diffusion of nanoparticles in tissues but should be applied with care in other cases. For example, an HOD feature extraction on trajectories from nanoparticles diffusing in a homogeneous medium would not be appropriate because there is no shared frame of reference for each trajectory.

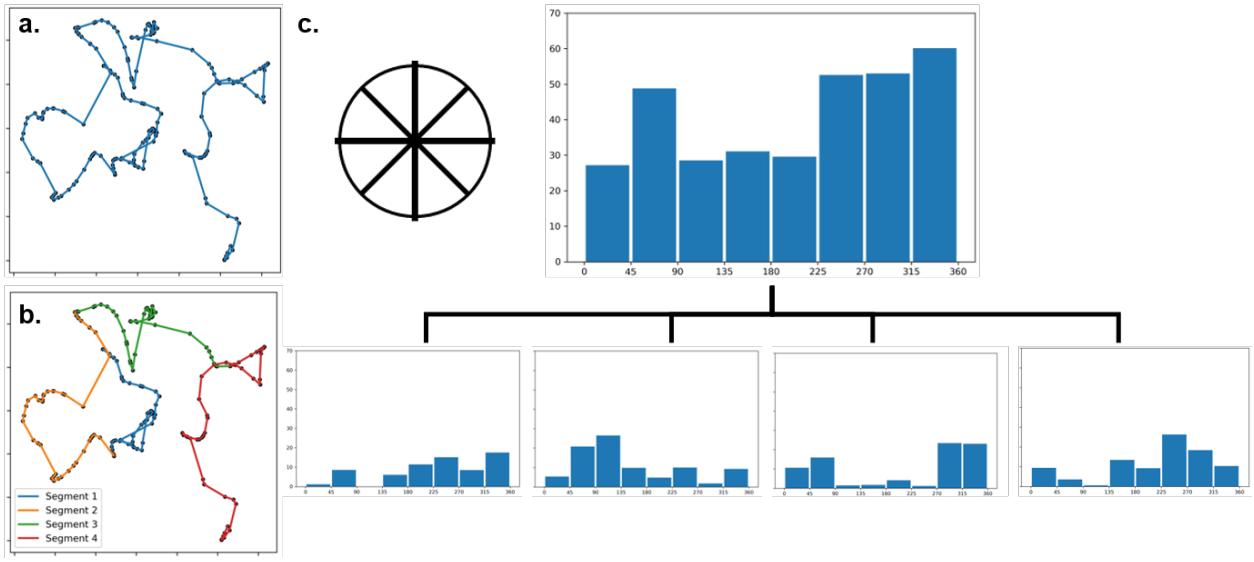

Figure 9: Illustration of histogram of oriented displacements (HOD) and a temporal pyramid feature extraction scheme. (a) Trajectory of random motion, (b) Trajectory of random motion broken down into four segments with equal numbers of frames, (c) HODs organized into a temporal pyramid. (Top) Each unit step in (a) is binned by its direction (Bottom) Each trajectory in (b) is binned by its direction.

0.2.3 Other machine learning techniques from AI fields

The machine learning methods from AI fields have thus far been primarily focused on alternate feature extraction techniques. In Section 0.2.3, we will look at alternate ways of analyzing trajectory datasets whose novelty isn't primarily associated with the feature extraction step. In this section, we will examine two neural network configurations specifically tailored for time-series datasets (convolutional neural networks and recurrent neural networks).

0.2.3.1 Recurrent neural networks for time series datasets

One machine learning strategy that is especially suited for motion trajectories and other sequence-based datasets are recurrent neural networks (RNNs). In contrast to linearly structured neural networks, nodal connections in RNNs can be fed forward as well as backward giving them memory of previous states (Figure 10). RNNs have been used on a variety of sequenced data, including handwriting, speech, and

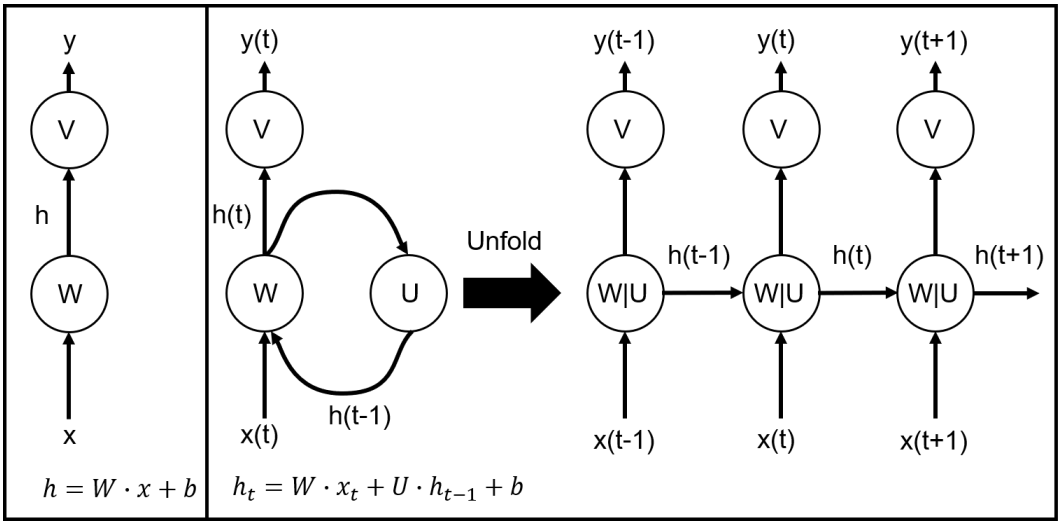

Figure 10: Comparison of linear neural network with a recurrent neural networks. Whereas the flow of information in a linear neural network is unidirectional (left), recurrent neural networks have memory properties due to their use of feedback loops (right).

music recognition. Learning with an RNN involves stepping forward both through layers and through time. Using this configuration, no form of feature extraction or parameterization must be performed before prior to feeding inputs into the neural network. However, in most workflows some analog of subset selection must be performed by subsampling from the overall trajectory to reduce convergence times. One example of using RNNs with trajectory datasets was demonstrated by Shah & Romijnders who predicted the success of three-point shots from basketball trajectories [67]. RNNs were fed 12 frames worth of XYZ coordinates (about half a second of data) at various distances for the hoop. In all cases except 2 feet away from the hoop, the RNN model outperformed the general linear and gradient-boosted models, achieving a 0.930 receiver operating characteristic area under cover compared to 0.875 and 0.942 at 2 feet, 0.906 compared to 0.721 and 0.848 at 4 feet, and 0.843 compared to 0.558 and 0.71 at 8 feet.

It is actually surprising that RNNs have not yet found application in biological trajectory datasets, as they are specifically made to handle time series data. This is likely not only due to novelty of the method. Because RNNs are computationally expensive, researchers will typically compensate by using only a small subset of the original raw trajectories e.g. Shah & Romijnders only used 12 frames for classification of

basketball trajectories. For application to biologically related datasets where diffusion is a primary transport mechanism, users would have to choose whether to sacrifice temporal resolution by sub-sampling at evenly spaced intervals within trajectories or spatial resolution by selecting a smaller but connected portion of each trajectory.

0.2.3.2 Convolutional neural networks

Dabiri & Heaslip sought to minimize human interference inherent in feature extraction steps by feeding trajectories directly into a convolutional neural network (CNN) which can operate directly on trajectory datasets [68]. Deep learning methods simultaneously operate on multiple levels of complexity, from the raw data low-level and high-level features. In essence, feature extraction steps are performed by machine learning algorithms rather than determined by humans. Dabiri & Heaslip use Global Positioning System (GPS) trajectories obtained from the GeoLife project to predict transportation mode (walk, bike, bus, driving, train).

CNNs take advantage of the spatial information built into consecutive values of the inputs: rather than connecting each node in a layer to all nodes in the previous layer, CNNs only connect neurons to a small region of the previous layer. This also helps prevent overfitting by reducing the number of weights. CNNs apply a series of stacked learnable filters to the inputs of each layer in the network, conceptually similar to applying an image processing filter. Each neuron is connected to a small region of the previous layer. The output is calculated as the dot product of the weights and biases of the filter with the inputs from the previous layer.

CNNs provide another approach that circumnavigates the problem of feature selection from trajectory datasets. CNNs have the disadvantage of being computationally expensive. Dabiri & Heaslip report a 25-minute training time for 62 epochs for a single neural network using a system equipped with a Core i7 2.50 GHz processor and a 16.0 GB memory [68]. CNNs also require a lot of care when selecting hyperparameters. However, when trained well with regularization techniques implemented to prevent overfitting, their accuracy is very competitive with other methods.

0.2.4 Future directions

The most urgent applications in the field are a wider examination of feature extraction methods. Thus far in the biomedical literature, the most common approach is to use some sort of geometry-based approach but with no formal guidance in feature selection. We have introduced a number of alternate feature extraction steps, including Fourier transforms, histogram of oriented displacements, and spatial goals. These are by no means all-encompassing and may require modification for trajectory datasets that are primarily diffusion-based.

Second, novel neural network architectures have just barely begun to be used with trajectory datasets in biological applications. Two types in particular, convolutional neural networks and recurrent neural networks, are particularly suited for time series datasets and have yet to be applied to MPT datasets. These should be benchmarked to existing methods to assess what improvements they offer to traditional approaches.

Finally, the range of questions that scientists can ask with MPT datasets can be greatly expanded. As demonstrated in section 0.2, machine learning methods have been primarily used to classify motion types of trajectory datasets. While useful, this question is limited to cases where a model already exists: the method is essentially reduced to a goodness of fit problem. One reason machine learning methods are powerful is that they can go beyond existing models to find patterns that may not be immediately apparent to researchers. For instance, there is no model describing how nanoparticle surface functionality correlates to nanoparticle motion. But a machine learning approach may be able to distinguish nanoparticle surface functionality based on nanoparticle trajectories without an existing model between the two variables. We have examined some of the unique classification problems being asked in the computer science and AI fields, including differentiating between human action types, predicting whether a 3-point shot is successful, and classifying driving styles. Similarly nuanced questions can be asked of trajectory datasets of cells, cell receptors, and nanoparticles.

The techniques that have been introduced in section 0.2 show promise in further advancing screening techniques available to researchers developing nanoparticle therapeutics. By increasing the number

of questions that can be answered using MPT, researchers can not only use MPT to screen a nanotherapeutic's transport properties, but they can also potentially assess a variety of factors at the particle-environment interface.

0.3 Thesis Outline

In Chapter 1 entitled *"Colloidal stability as a determinant of nanoparticle behavior in the brain,"* we investigate one key aspect of nanoparticle interactions with biological environments, namely, aggregation kinetics. Nanoparticle stability is highly media-dependent and can be different as they navigate across biological barriers. We seek to show how nanoparticle aggregation measured *in vitro* via dynamic light scattering measurements can be used to predict behavior in both an *in vitro* gel model of the brain and an *ex vivo* tissue slice model. Investigating the colloidal stability of nanoformulations in *in vivo* like conditions is one screening tool that can accelerate nanoparticle translation. This demonstrates one aspect of how nanoparticles can be used to examine biological phenomena over a range of observational scales.

In Chapter 2 entitled *"Predicting in situ nanoparticle behavior using multiple particle tracking and artificial neural networks,"* we demonstrate how nanoparticle trajectory datasets collected via fluorescent microscopy and multiple particle tracking can be used to distinguish nuanced aspects of the nanoparticle-microenvironment interaction space using neural networks, including protein adhesion and nanoparticle cell uptake. This method of analysis highlights the potential of nanoparticles to be used as pre-clinical diagnostic probes without the use of complex chemistries.

In Chapter 3 entitled *"Design parameters of PEGylated brain-penetrating nanoparticles,"* we use similar analytical methods as outlined in Chapter 2 to explore key design parameters in nanoparticle design in the context of the brain including surface functionality, PEG chain length, and PEG grafting density. Trajectory datasets can thus be used in a feed forward configuration in a diagnostic setting and a feedback configuration to guide nanoparticle design.

In Chapters 4 and 5 we summarize all methods used throughout the paper and summarize additional work performed tangent to this project.

1

Colloidal stability as a determinant of nanoparticle behavior in the brain

1.1 Introduction

When administered systemically, a nanoparticle must remain stable in blood, overcome the BBB, and then navigate the extracellular space (ECS) to selectively act on or uptake in disease cells. Nanoparticle stability has been evaluated in serum [69], blood [70–72], and saline [73, 74] as a function of size, surface charge, and surface functionality. Size and surface coating are also physicochemical factors that have been explored for nanoparticle uptake across the intact and impaired BBB [49, 75–78], in addition to shape

and particle rigidity [79, 80]. By crossing the BBB, nanoparticles can provide cell-specific uptake, including targeted delivery to lysosomes within neurons [81], and selective targeting of microglia and astrocytes to suppress inflammation and oxidative stress [78, 82, 83]. However, once across the BBB, nanoparticles are exposed to a physical and chemical environment that is unique to the brain. Physically, nanoparticle size is a particularly important parameter for penetration within the brain ECS [4]. Pore sizes within the brain have been estimated to be anywhere from 30-65 nm [84] to 20 – 225 nm in width [49], based on the methods of probing the ECS. Yet, there is a significant decrease in the ability of a nanoparticle to move within the brain parenchyma at sizes larger than 100 nm, suggesting an upper limit on nanoparticle size for effective drug delivery to the brain [49]. Size has also been shown to influence nanoparticle compartmentalization in brain cells [85]. Additionally, surface charge and surface functionality, including relative hydrophobicity, can be predominant factors in determining a particle's ability to effectively diffuse within the brain extracellular matrix [49, 86, 87].

Importantly, all prior measurements to assess the impact of physicochemical properties on brain uptake and penetration within the brain parenchyma assume particles remained stable (no agglomeration or aggregation) not just in blood while circulating, but also in the brain environment. Yet, there is little evidence demonstrating that nanoparticles remain stable in brain microenvironment conditions. Therefore, there is a need to perform characterization of nanoparticle size and stability as a function of ion composition, concentration, or pH in brain extracellular fluid, all factors in the brain microenvironment. For example, calcium is a unique factor in the brain due to its presence in free form and varies spatially and temporally based on local cellular activity [88, 89]. Like calcium, pH levels vary spatially and temporally in the brain [90]. Changes in pH can alter the protonation state of functional groups on the nanoparticle surface, which can also change nanoparticle stability. Each of these factors could alter a nanoparticle's biological identity in the brain ECS, which could influence diffusive capability and cellular uptake of a therapeutic platform [91].

This study sought to systematically characterize nanoparticle behavior in representative brain microenvironment conditions to determine the predictive ability of colloidal stability on diffusive capability. Poly(ethylene glycol) (PEG)-coated and carboxyl-coated polystyrene (PS-PEG and PS-COOH respec-

tively) nanoparticles from 60- to 2000 nm were used to evaluate nanoparticle behavior in conditions present in the brain microenvironment. PEG sterically stabilizes nanoparticles, and provides stealth capabilities that reduce the interaction with the surrounding environment [92]. In the context of aggregation kinetics, the comparison of PS-COOH and PS-PEG particles is useful in demonstrating the differences between electrocratically and sterically stabilized nanoparticles. Additionally, nanoparticles are normally characterized at room temperature in low concentration sodium chloride (NaCl) solutions or saline solutions [93], and higher temperatures at physiological conditions could destabilize nanoparticles. Sterically stabilized nanoparticles can be sensitive to changes in temperature of just 1-2°C [94]. Therefore, this study evaluated the aggregation kinetics, colloidal stability, and diffusive capability of nanoparticles with varying size, surface charge, and surface coating in a range of brain interstitial fluid ion concentrations and compositions, pH conditions, and temperature.

1.2 Results and Discussion

1.2.1 Nanoparticle characterization

PS-COOH nanoparticles were compared with PS-PEG nanoparticles due to the widespread use of PEGylation as a method to sterically stabilize nanoparticle formulations and shield them from macrophage uptake *in vivo* [75]. All physicochemical nanoparticle properties for PS-COOH and PS-PEG nanoparticles used in this study are reported in Table 1.1. As expected, electrophoretic measurements of PS-COOH nanoparticles gave a ζ-potential of -20 to -70 mV, depending on the size of the nanoparticle. Upon PEGylation of PS nanoparticles, all nanoparticles had an increase in measured hydrodynamic diameter of ~10-20 nm in size (Table 1.1), which is expected given the molecular weight of the PEG chain used (5 kDa) [76]. The decrease in magnitude of ζ-potential for PS-PEG nanoparticles compared to PS-COOH nanoparticles indicates that conjugation of PEG to the nanoparticle surface was successful.

Table 1.1: Physicochemical characterization of PS nanoparticles including hydrodynamic diameter and ζ-potential in 10mM NaCl at 23°C. Data was collected via DLS and ZetaSizer (n=3). All values are reported as mean ± standard error (SEM).

Particle Size (nm)	Surface Coating	Mean Hydrodynamic Diameter ± SEM (nm)	Mean ζ-potential	PDI ± SEM
60	COOH	49.0 ± 2.4	-23.3 ± 2.3	0.14 ± 0.0
60	PEG	54.3 ± 2.3	-1.4 ± 0.5	0.20 ± 0.0
100	COOH	110.3 ± 1.6	-68.8 ± 0.8	0.04 ± 0.0
100	PEG	127.2 ± 1.0	-3.1 ± 0.1	0.02 ± 0.0
200	COOH	216.1 ± 2.4	-56.2 ± 2.0	0.01 ± 0.0
200	PEG	237.0 ± 1.5	-7.6 ± 0.4	0.02 ± 0.0
500	COOH	416.1 ± 6.0	-48.5 ± 1.4	0.05 ± 0.0
500	PEG	545.2 ± 3.6	-4.4 ± 0.1	0.05 ± 0.0
1000	COOH	1167 ± 34	-73.8 ± 2.4	0.44 ± 0.3
1000	PEG	1019 ± 22	-3.4 ± 0.2	0.57 ± 0.3
2000	COOH	1091 ± 106	-47.6 ± 2.2	0.51 ± 0.3
2000	PEG	1271 ± 47	-4.2 ± 0.7	0.43 ± 0.4

1.2.2 Nanoparticle stability as a function of calcium and magnesium concentration

100 nm PS-COOH and PS-PEG colloidal stability was evaluated *in vitro* in solutions of calcium chloride ($CaCl_2$) and magnesium chloride ($MgCl_2$). In $CaCl_2$ solutions, PS-COOH nanoparticles remained stable up to 2 mM salt concentration, but form aggregates at concentrations higher than 4 mM (Figure

1.1A). PS-PEG nanoparticles remained stable in a biologically relevant range of calcium concentrations spanning 0 to 10 mM. Similar behavior for both particle types was found in $MgCl_2$ solutions; PS-COOH nanoparticles remained stable in solutions up to 4 mM $MgCl_2$ and aggregated at concentrations of 5 mM and higher (Figure 1.1B). PS-PEG particles remained stable in $MgCl_2$ concentrations at least up to 10 mM.

Cerebrospinal fluid (CSF) equilibrates with interstitial fluid (ISF), the fluid filling the extracellular space within the brain, in the ventricles and perivascular spaces within the brain [95]. ISF is a complex fluid with composition that varies regionally due to metabolic and signaling processes of cells [96], and is difficult to measure, but can be regarded as similar to that of CSF. Within ISF and CSF, calcium plays a vital regulatory role, and is a unique factor in the brain due to its presence in free form [88, 89]. Calcium is a universal messenger among multiple cell types throughout the body and is particularly important in the brain. Calcium is involved in regulating neurotransmitter synthesis and release, neuronal excitability, and phosphorylation, as well as long-term processes including memory and neuroplasticity [97]. Calcium is present at 2 mM in CSF under normal neurological conditions, but in the presence of injury or disease, calcium can become dysregulated, resulting in higher concentrations [98–100]. Calcium dysregulation is linked to brain aging [101, 102], has been implicated in toxicity in glial cell populations, neurodegeneration, neuroinflammation [103], and can be a factor in multiple diseases including Alzheimer's disease, Parkinson's disease, amyotrophic lateral sclerosis, Huntington's disease, and spinocerebellar ataxias [104]. The therapeutic implications for changes in calcium concentration in the presence of injury is of particular interest given previous findings that show calcium concentration can be a significant factor in nanoparticle aggregation [105]. In the context of nanotherapeutics, changes in calcium concentrations in both the ECS and cell cytoplasm can ultimately affect drug efficacy. Increasing calcium concentrations reduces the electrostatic double layer (EDL) repulsive energy between particles. Once a critical concentration is reached, nanoparticle aggregation is initiated. The variation between calcium and magnesium threshold concentrations that cause PS-COOH nanoparticles to aggregate can be explained in terms of the different hydration behavior of calcium and magnesium ions. Magnesium ions have more tightly held water molecules due in part to their smaller size [106]. Water molecules are less likely to dissociate from magnesium ions than calcium ions, preventing them from binding to the negatively charged PS-COOH

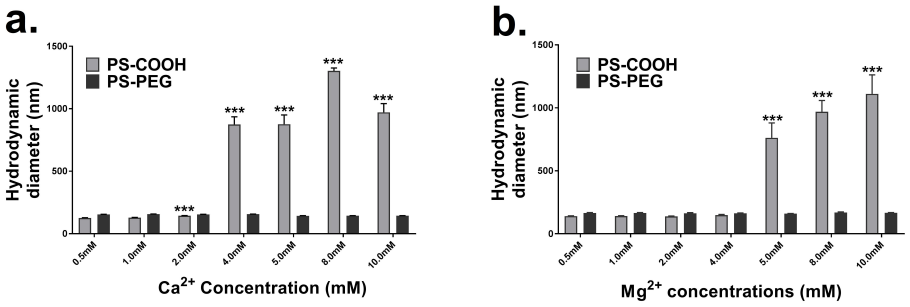

Figure 1.1: Physicochemical characterization of 100 nm PS nanoparticles in calcium solutions. (a) Hydrodynamic diameters of PS-COOH and PS-PEG nanoparticles in varying concentrations of aqueous calcium chloride solutions as measured by DLS (n=3). (b) Hydrodynamic diameters of PS-COOH and PS-PEG nanoparticles in varying concentrations of magnesium chloride solutions as measured by DLS (n=3). All values are reported as mean ± SEM. Significance as compared with 0 mM condition are indicated by * $p < 0.033$, ** $p < 0.002$, *** $p < 0.001$.

nanoparticles [107]. Both calcium and magnesium independently impact nanoparticle stability; however, both are simultaneously present in CSF. To determine the combined effects of these ions at different concentrations, additional experiments were performed in 1:1 molar solutions of salts, e.g. magnesium sulfate and calcium chloride. Nanoparticles in these mixtures exhibited behavior intermediate to the observed behavior in solutions of the separate component salts (Figure A.2). For example, PS-COOH nanoparticles that form aggregates in magnesium chloride concentrations greater than 5 mM only begin to aggregate in 1:1 magnesium chloride: magnesium sulfate solutions at concentrations greater than 8 mM.

These studies raise additional questions regarding the relevance of particle size as a significant factor in nanoparticle aggregation, and the role the cation-associated anion associated has on nanoparticle aggregation. A similar static aggregation study using 60 nm PS-COOH and PS-PEG nanoparticles showed little difference in behavior from the 100 nm nanoparticles (Figure A.3A). 60 nm PS-COOH and PS-PEG nanoparticles tested in magnesium sulfate ($MgSO_4$) also showed that, while the PS-COOH nanoparticles begin to aggregate at higher salt concentrations, the same rate of aggregation was not seen when compared with $MgCl_2$ (Figure A.3B). This indicates that the anion also plays a role in determining nanoparticle stability [108], but the result was unexpected as it contradicts predictions made with the Hofmeister

series [109]. In switching from chloride to sulfate, both the identity and the valence of the anion are varied. Polyvalent ions of either sign have a possibility of binding to the nanoparticle surface. Measured ζ-potentials in 2 mM solutions of $MgCl_2$ and $MgSO_4$ indicate a more negative charge on 100 nm PS-COOH nanoparticles in $MgSO_4$ (-19.0 ± 0.7 and -21.0 ± 0.5 respectively, p=0.08). The added negative charge could provide additional electrostatic stability.

1.2.3 Calcium-dependent aggregation of nanoparticles at multiple temperatures and pHs in ACSF

In acidic conditions (pH 5.5) and at room temperature (23°C), 100 nm PS-COOH nanoparticles experienced aggregation effects at all $CaCl_2$ concentrations in artificial CSF (ACSF) (Figure 1.2A). PS-COOH nanoparticles had a nominal size of 141.1 nm, which increased to 150.0 nm when $CaCl_2$ was increased to 0.5 mM after 10 minutes. This continued to increase in size at a rate of 4.2 ± 0.6 nm/min until 8 mM $CaCl_2$, when aggregation accelerated to 11.3 ± 1.8 nm/min. In these same conditions, 100 nm PS-PEG nanoparticles saw no significant increase in size (from 0.0 ± 0.2 nm/min to -0.4 ± 0.2 nm/min) and stayed constant over the entire range of $CaCl_2$ concentrations.

When the temperature was raised to body temperature (37°C), the aggregation profiles changed. The baseline size at 0 mM $CaCl_2$ was 20 nm higher (160.6 nm) for 100 nm PS-COOH nanoparticles, but increased linearly, similar to the 23°C profile. There was a similar acceleration to aggregation at the 8 mM threshold. 100 nm PS-PEG nanoparticles experienced an overall increase of 20 nm, indicating the potential onset of aggregation, and could result in large aggregates at long timescales. When temperature is increased, there are two effects at play that can alter stability: first, the PEG brush layer contracts; second, the hydrodynamic radii of the nanoparticles decrease. However, the compressed PEG layers also reduce the steric hindrance that sterically stabilizes nanoparticles. At high enough calcium concentrations, the PS-PEG nanoparticles also begin to aggregate.

Increasing the pH to 7.2 led to a change in behavior for both particle types (Figure 1.2B). PS-COOH nanoparticles experienced significant aggregation at a threshold of 4 mM $CaCl_2$ at 25°C (280.1 nm com-

pared to 161.1 nm at 0 mM $CaCl_2$, p>0.001). After 6 mM $CaCl_2$, particles continued to increase in size overall, but experience downward trends after the initial addition of $CaCl_2$ to the solution. When increased to body temperature, PS-COOH nanoparticles aggregated at a threshold of 2 mM $CaCl_2$, continuing to increase in overall size, but then decrease following $CaCl_2$ addition similar to the 23°C profiles. This indicates that larger aggregates >1000 nm are settling out of solution. 100 nm PS-PEG nanoparticles remained stable at 23°C, up until 6 mM where aggregation begins to occur. At 37°C, PS-PEG nanoparticles remained stable until 1 mM $CaCl_2$ with modest increases in sizes until 3 mM $CaCl_2$. Above 3 mM, PS-PEG nanoparticles began to aggregate more rapidly, reaching sizes in excess of 1000 nm at 8 mM $CaCl_2$ concentrations. In basic conditions (pH 8.5), 100 nm PS-COOH nanoparticles had a very small range of stable $CaCl_2$ concentrations (Figure 1.2C). At room temperature, PS-COOH nanoparticles remained stable up until 1 mM $CaCl_2$, but at body temperature, the addition of any $CaCl_2$ initiated aggregation. High pH causes protons to dissociate from carboxyl groups on the PS-COOH nanoparticles, generating a negative charge on the particle surface. The presence of divalent cations induces bridging effects between the PS-COOH nanoparticles, which is accelerated at higher $CaCl_2$ concentrations. 100 nm PS-PEG nanoparticles are stable over a wider range of $CaCl_2$ concentrations than PS-COOH nanoparticles in basic conditions, and aggregate sizes are four-fold times smaller: PS-COOH nanoparticles reach ~4000 nm at 10 mM $CaCl_2$, while PS-PEG nanoparticles reach ~1000 nm in similar conditions. The aggregation of PS-PEG nanoparticles is also likely due to bridging effects in the presence of calcium. The more negative charges of PS-PEG nanoparticles brought about by basic conditions can interact with calcium ions, and initiate aggregation events.

There was a demonstrated difference in colloidal stability of 100 nm PS-COOH and PS-PEG nanoparticles in ACSF at 2 mM $CaCl_2$ and pH 7.2. PS-PEG nanoparticles experienced little to no aggregation, while PS-COOH nanoparticles had a steep aggregation profile. This has important implications. First, the observed difference in diffusive ability in living brain tissue in previously published studies using PS-PEG and PS-COOH nanoparticles [49] could be in part due to the differences in nanoparticle colloidal stability. This study has shown that PS-COOH nanoparticles are colloidally unstable in ACSF at conditions similar to those in the brain, and small perturbations can worsen aggregation effects. Second, this

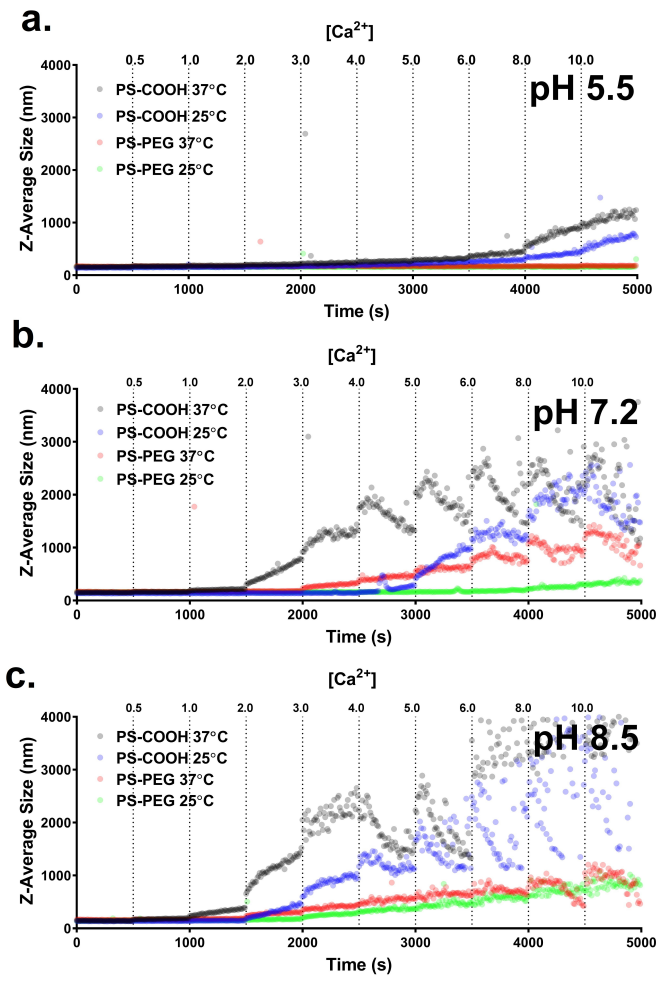

Figure 1.2: Aggregation in ACSF as a function of calcium chloride concentration. Aggregation profiles of 100 nm PS-COOH and PS-PEG nanoparticles at 25°C and 37°C in ACSF pH (a) 5.5, (b) 7.2, and (c) 8.5 at increasing calcium chloride concentrations from 0 mM to 10 mM (n=1).

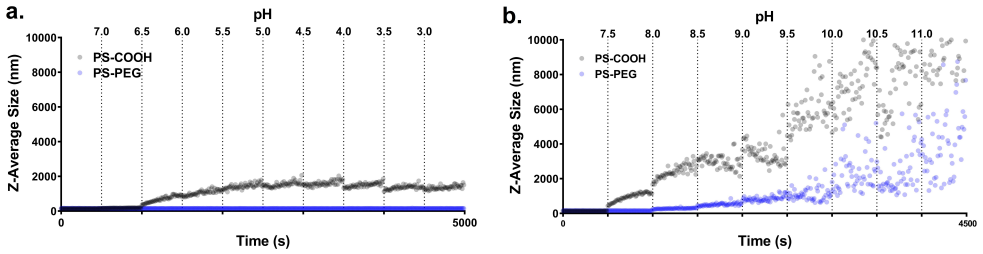

Figure 1.3: Aggregation in ACSF as a function of pH. Aggregation profiles of 100 nm PS-COOH and PS-PEG nanoparticles at 25°C and 4 mM calcium chloride in ACSF (a) at increasingly acidic conditions from pH 7.2 to pH 3.0 (n=1) and (b) at increasingly basic conditions from pH 7.2 to pH 11.0 (n=1).

study has demonstrated the importance of accounting for temperature when characterizing nanoparticles in vitro. PS-COOH nanoparticles aggregated in 2 mM $CaCl_2$ ACSF at body temperature (37°C), but did not experience significant aggregation at room temperature (137.1 nm compared to 135.7 nm at 0 mM $CaCl_2$, p=0.31). PS-PEG nanoparticles also became destabilized at higher temperatures, but to a lesser extent. Temperature can affect nanoparticle stability by changing dissociation rates for electrostatically stabilized colloids and by structural changes for sterically stabilized colloids [110], and therefore should be accounted for when performing *in vitro* characterization of nanoparticles for *in vivo* applications.

1.2.4 pH-dependent aggregation of nanoparticles in ACSF

To explore the effect of pH on nanoparticle aggregation, pH was adjusted by 0.5 pH units every ten minutes. In increasingly acidic conditions in ACSF, 100 nm PS-COOH nanoparticles remained stable up to pH 6.5, where aggregation began (Figure 1.3A). Particle sizes plateaued at 2000 nm at pH 5.0 and did not increase further with more acidic pH conditions. 100 nm PS-PEG nanoparticles remained stable at all acidic pH conditions in ACSF. In increasing basic conditions, PS-COOH nanoparticles began aggregating at pH 7.5 and continued to increase in size beyond a hydrodynamic diameter of 10 μm (Figure 1.3B). PS-PEG nanoparticles began to aggregate at pH 8.0, reaching maximum sizes of 6 μm at pH 11. PS-COOH nanoparticles had a narrow range of stability in ACSF (7.0-7.5), while PS-PEG nanoparticles had a much wider range, especially in acidic conditions (3.0-8.0). PEGylated nanoparticles are stabilized

through a steric mechanism, while the PS-COOH nanoparticles are electrocratically stabilized and are more sensitive to changes in the ionic environment. In the presence of divalent cations and a relatively high ionic strength (~160 mM compared to 10 mM in standard characterization techniques), the magnitude of the ζ-potential of PS-COOH nanoparticles is small compared to characterization measurements in 10 mM NaCl (Figure A.5). With little electrostatic repulsion present, PS-COOH nanoparticles are unstable in ACSF and can aggregate readily in response to small fluctuations in pH and divalent cation concentration. In basic conditions, the surface charge of PS-COOH nanoparticles become more negative as the carboxyl groups become deprotonated. This leads to an increase in bridging effects due to the presence of calcium, resulting in high instability in basic conditions. As pH becomes more acidic, the surface charge becomes less negative, eventually passing the point of zero charge (~pH 6.5) and triggering the onset of aggregation [111]. However, particle size does not continue to increase as pH becomes more acidic, as the low pH results in positively charged particles and the restoration of electrostatic repulsion.

Although sterically stabilized, PS-PEG nanoparticles can still be susceptible to aggregation effects as a function of pH. As pH becomes more basic, PS-PEG nanoparticles do begin to aggregate at ~pH 8. This could be due to interactions with calcium ions at unreacted carboxyl sites on the nanoparticle surface. The PS-PEG nanoparticles have a slight negative charge in pH 7 ACSF and are more negative as pH becomes more basic (Figure A.5). At more basic pH, these interactions are strong enough to cause bridging between calcium ions and PS-PEG nanoparticles. As pH shifts towards more acidic, PS-PEG nanoparticles do not aggregate, even as ζ-potentials become near-neutral, indicating that the steric stability lent by the PEG layer prevents any aggregation events from occurring.

1.2.5 Impact of calcium concentration on nanoparticle diffusion in gel model

To assess the impact of colloidal stability on nanoparticle diffusion, 100 nm PS-COOH and PS-PEG nanoparticles were tracked using high-speed multi-particle tracking (MPT) [49, 112] in an agarose gel, a representative geometric model of the brain microenvironment [113]. Diffusion coefficients for both 100

nm PS-COOH and PS-PEG nanoparticles depend on calcium concentration in the gel (Figure 1.4A, B). Representative frames from MPT videos are in Figure A.6. Diffusion coefficients of PS-COOH nanoparticles decrease as calcium concentration is increased (Figure 1.4C). At calcium concentrations exceeding 5 mM, PS-COOH nanoparticles become immobilized. As shown previously in Figure 2, 100 nm PS-COOH nanoparticles begin aggregating at calcium concentrations of 2mM. Thus, the immobility in gels is likely due to both bridging effects between nanoparticles resulting in aggregation and bridging effects with agarose molecules resulting in tethering. At 10mM calcium chloride, 100 nm PS-COOH nanoparticles are immobilized even further (diffusion coefficient 95%CI: 1.69 x 10^{-3}-1.71 x 10^{-3} $\mu m^2/s$).

PS-PEG nanoparticles also exhibit changes in diffusive behavior as calcium concentration is modified. In general, 100 nm PS-PEG diffusion coefficients decrease as calcium concentration is increased (Figure 1.4C). However, in all cases, the particles remain mobile, with diffusion coefficients of similar magnitude across the entire range of calcium concentration tested. As shown in Figure 1.2, the steric stability of PS-PEG nanoparticles improves their aggregation profiles in ACSF, but the particles do begin to aggregate at calcium concentrations higher than 2 mM in ACSF at pH 7.2 and 37°C. This reduction in aggregation can allow PS-PEG nanoparticles to retain their diffusive ability over a wider range of calcium concentrations than PS-COOH nanoparticles. Both size exclusion due to large particle aggregates and deposition in the gel could contribute to the reduced diffusive behavior of 100 nm PS-COOH NPs. To verify the impact of size exclusion on observed diffusion coefficients, and decouple the effects of size exclusion and altered nanoparticle-agarose interactions due to increased calcium levels, we performed multi-particle tracking experiments of various mixtures of PS-COOH and PS-PEG nanoparticles in ACSF without calcium chloride (non-aggregating conditions) to mimic aggregating nanoparticle at various stages of aggregation. We used an equal weight percent mixture of 100, 200, 500, 1000, and 2000 nm nanoparticles to represent early stage aggregation; an equal number percent mixture of 100, 200, 500, 1000, and 2000 nm nanoparticles to represent a later stage of aggregation; and 2000 nm nanoparticles to represent a long-term stage of aggregation. The physicochemical properties of the constituent particles are shown in Table 1.1. Larger particles will have reduced MSDs due solely to reduced Brownian motion as predicted by Stokes-Einstein, but pore size restrictions will prevent large particles from diffusing at all. This effect can be observed in Figure 1.5.

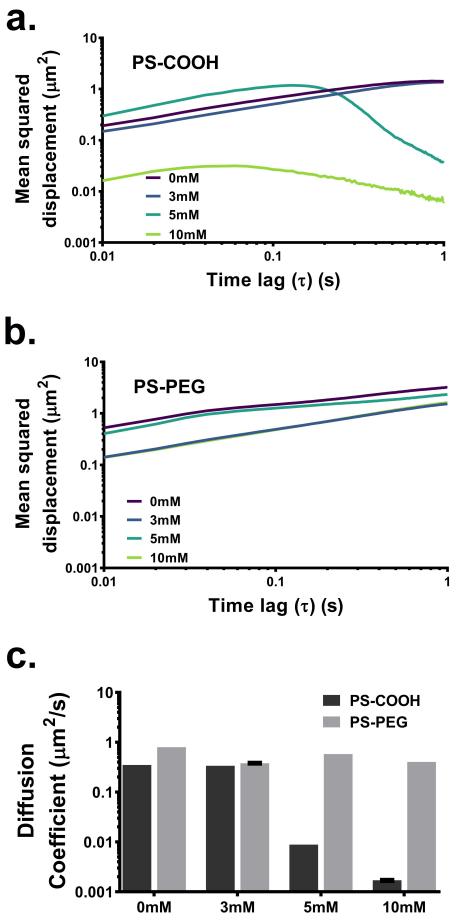

Figure 1.4: Diffusion data in agarose gels in ACSF as a function of calcium concentration. Precision-weighted MSD profiles as a function of time lag (τ) for (a) PS-COOH nanoparticles and (b) PS-PEG nanoparticles in 0.4% in ACSF agarose gels at increasing calcium chloride concentrations (0, 3, 5, and 10 mM). Data represent the precision-weighted geometric averages over videos per well (n=5) and wells per condition (n=4). Error bars at τ = 0.1, 0.5, and 1s represent 95% CIs. (c) Diffusion coefficients of PS-COOH and PS-PEG nanoparticles in agarose gels calculated at 1 s calculated as <MSD> = 4Dτ

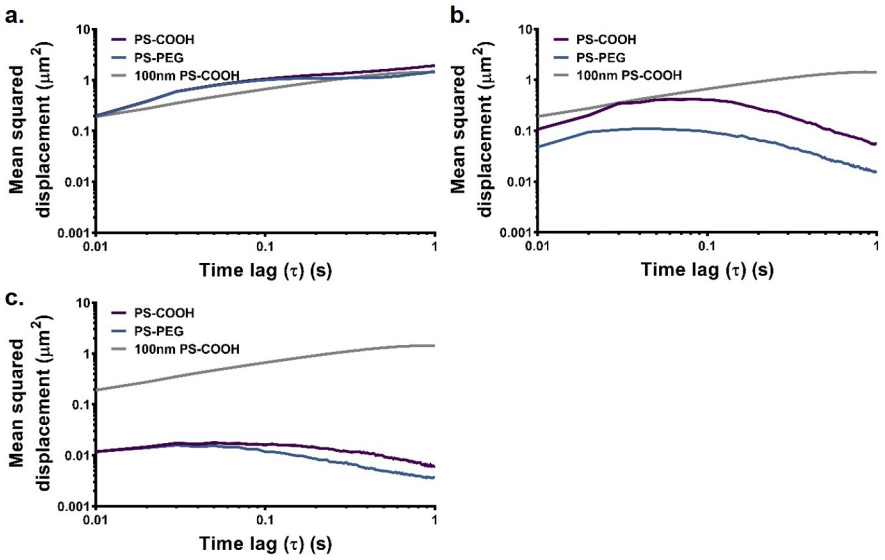

Figure 1.5: MSD profiles of PS-COOH and PS-PEG nanoparticle samples of varying average particle sizes to mimic nanoparticles in various stages of aggregation. This includes (a) equal mass fractions of 100, 200, 500, 1000, and 2000 nm PS-COOH (purple) or PS-PEG NPs (blue) in ACSF without calcium chloride, (b) equal particle concentrations of 100, 200, 500, 1000, and 2000 nm PS-COOH or PS-PEG NPs in ACSF without calcium chloride, and (c) 2000nm PS-COOH or PS-PEG NPs in ACSF without calcium chloride. Data represent the precision-weighted geometric MSD averages over videos per well (n=5) and wells per condition (n=4). Error bars at τ = 0.1, 0.5, and 1s represent 95% CIs. MSD values of 100 nm PS-COOH NPs (grey) in similar conditions is provided as a reference in all plots.

The equal-weight particle mixture is unhindered when compared with the 100 nm PS-COOH NPs in similar conditions (Figure 1.5A, diffusion coefficient 95%CI 4.799 x 10^{-1}-4.803 x 10^{-1} $\mu m^2/s$ compared to 3.555 x 10^{-1}-3.557 x 10^{-1} $\mu m^2/s$). The small number of larger particles mimicking early-stage aggregates do not affect the average behavior. The equal-number particle mixture has reduced diffusive behavior, due to a higher concentration of immobilized particles (Figure 1.5B, diffusion coefficient 95%CI: 1.389 x 10^{-2}-1.394 x 10^{-2} $\mu m^2/s$). It is only in the 2000 nm case the MSD profile essentially flatlines (Figure 1.5C, diffusion coefficient 95%CI: 1.550 x 10^{-3}-1.555 x 10^{-3} $\mu m^2/s$). Particle sizes smaller than the average pore size are a necessary but not sufficient condition for effective diffusive ability in porous media. For both PS-COOH and PS-PEG nanoparticles, the diffusive behavior decreases as the average particle size increases. In all cases, PS-COOH and PS-PEG profiles are similar (with more discrepancy in the equal number case) with PS-PEG profiles being less than the PS-COOH profiles (2000 nm PS-PEG diffusion coefficient 95%CI: 9.11 x 10^{-4}-9.15 x 10^{-4} $\mu m^2/s$). This can be partly attributed to the reduced diffusion coefficients predicted by Stokes-Einstein due to the larger size of the PS-PEG NPs.

While polydisperse samples can be introduced into the gel model, it is more difficult to systematically probe the effect of polydispersity. Ideally, one would have a set of nanoparticles with similar average particle sizes and varying polydispersity. We do not provide a systematic evaluation of polydispersity here. It is known that particles of different sizes have different deposition rates and filtration coefficients in porous media as demonstrated in an analytical model by Yang *et al.* [114]. Yoon *et al.* examined the effect of polydispersity on particle transport properties experimentally using a polydisperse sample of 1-25 μm fluorescent particles in a medium of monosize 4 mm glass beads [115]. They demonstrate that for polydisperse samples, transport properties vary with depth in the porous medium due to filtration of larger particles near the inlet. As our particles were pre-mixed prior to gelation, there should be no variation of diffusive properties as a function of depth.

An additional level of complexity introduced into a model of aggregating particles in porous media is the effect of time dependence. Both average size and polydispersity are changing with time, as shown in Figure 1.2. If the time scale of aggregation and the time scale of measurement are similar, this could make any resulting diffusion data unreliable. In order to evaluate the impact of absolute time on the collected

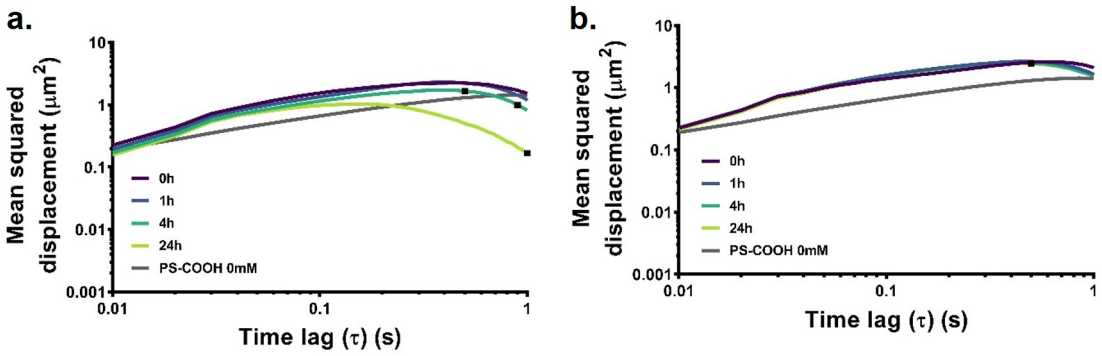

Figure 1.6: Time dependence of diffusion in agarose gels. MSD profiles of 100 nm (a) PS-COOH and (b) PS-PEG NPs in 0.4% agarose gels constituted with ACSF 5mM calcium chloride (aggregating conditions) at 0 (purple), 1 (blue), 4 (teal), or 24 h (lime) after gelation. Data represent the precision-weighted geometric MSD averages over videos per well (n=5) and wells per condition (n=4). Error bars at τ = 0.1, 0.5, and 1s represent 95% CIs. MSD values of 100 nm PS-COOH NPs (grey) in similar conditions is provided as a reference in all plots.

MSD data, we collected videos in gels of aggregating 100 nm PS-COOH and PS-PEG nanoparticles at 0, 1, 4, and 24 hours after the gels had set. The results are shown in Figure 1.6. The measured diffusion coefficients of the PS-COOH nanoparticles decrease over time (diffusion coefficient CIs: 3.788 x 10^{-1}-3.789 x 10^{-1}, 2.978 x 10^{-1}-2.979 x 10^{-1}, 2.036 x 10^{-1}-2.037 x 10^{-1}, 4.169 x 10^{-2}-4.172 x 10^{-2} $\mu m^2/s$ at 0, 1, 4, and 24 hours). This can be attributed to the greater proportion of large aggregates at later timepoints. The PS-PEG diffusion coefficients are more stable over time (diffusion coefficient CIs: 5.269 x 10^{-1}-5.270 x 10^{-1}, 4.113 x 10^{-1}-4.113 x 10^{-1}, 3.850 x 10^{-1}-3.851 x 10^{-1}, 3.856 x 10^{-1}-3.857 x 10^{-1} $\mu m^2/s$ at 0, 1, 4, and 24 hours), which can also be attributed to their shallower aggregation profiles as shown in Figure 1.2. In order to minimize the effect of absolute time as a factor in our gel model, we collected all data in gels after a 24 hour gelation period. This ensures that the gel is fully set and that aggregation is not present during video collection. In order to determine whether a nanoparticle's diffusive ability could be predicted by its aggregation behavior in an *in vitro* environment, the nanoparticle diffusion coefficients were plotted against the hydrodynamic diameters as measured by DLS in ACSF as a function of calcium concentration (Figure 1.7). There is a precipitous drop in diffusive ability in agarose gels when particle aggregates reach sizes between 1200 and 1600 nm. When nanoparticle sizes are less than 1200 nm, the diffusion coefficients

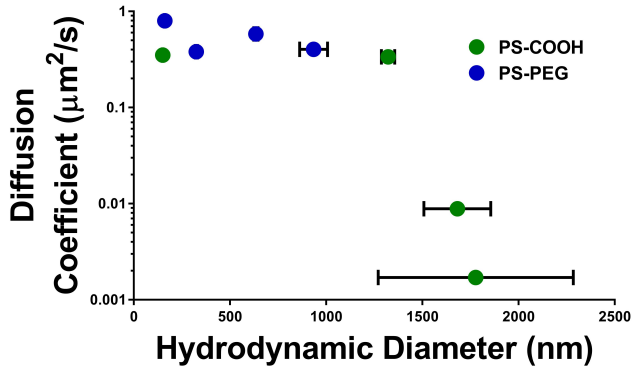

Figure 1.7: Diffusion coefficients of PS-COOH and PS-PEG nanoparticles in 0.4% agarose gels constituted with ACSF with 0/3/5/10 mM calcium chloride as a function of hydrodynamic diameter measured in ACSF with similar calcium concentrations. Error bars represent SEM.

in gels are of the same magnitude independent of the mechanism of stabilization (steric vs electrostatic). However, nanoparticle diffusive behavior cannot entirely be explained by aggregation state. Even with similar hydrodynamic diameters (150-160 nm), PS-COOH nanoparticles have roughly half the diffusion coefficient of PS-PEG nanoparticles. Instead, the division of nanoparticle behavior into two diffusive regimes demonstrates that the diffusive ability on nanoparticles in a gel model of the brain can be predicted based on its hydrodynamic diameter as measured by DLS. This could potentially be translated into a screening tool before nanoparticles are used in *ex vivo* and *in vivo* experiments. Interestingly, PS-COOH nanoparticles retained their diffusive behavior in up to 3 mM $CaCl_2$ in ACSF in agarose gels. PS-COOH retention of diffusive ability did not seem to coincide with the observed aggregate size of >1000 nm in ACSF at the same conditions. These results are indicative of potential limitations of the agarose gel model. A gel model of the brain should account for both macro- and micro-scale rheology, with a distribution of effective pore spacing within the gel that are representative of the distribution of extracellular spaces in the brain parenchyma. Pore sizes in agarose gels scale with agarose concentration according to the power law $a \sim C$ [116]. Using the model proposed by Pernodet *et al.* and confirmed via atomic force microscopy measurements, this estimates a pore size of approximately 1000 nm for 0.4%agarose gels. Other experiments using positive pressure infusion have estimated pore sizes in low-concentration agarose gels to be

between 10-100 nm [113], on which the present experiments were based. The presence of larger pores on the order of ~1000 nm could explain why even in the presence of aggregation, PS-COOH nanoparticles are able to diffuse in agarose gels, whereas in living brain diffusion, PS-COOH nanoparticle diffusion is limited [49].

1.2.6 Impact of calcium concentration on nanoparticle diffusion in a brain tissue model

In order to test whether aggregate size as measured via DLS in ACSF can be used to predict diffusive behavior in the brain, we also performed diffusion experiments in an organotypic slice model of the brain in P14 Sprague-Dawley rats. Two particle types (PS-COOH and PS-PEG) and four base particle sizes (60, 100, 200, and 1000 nm) were used. Results are shown in Figure 1.8. PS-COOH MSD profiles decreased as a function of base particle size (diffusion coefficient CIs 2.960×10^{-2}-2.962×10^{-2}, 1.656×10^{-2}-1.662×10^{-2}, 1.274×10^{-2}-1.280×10^{-2}, 7.36×10^{-4}-8.80×10^{-4} $\mu m^2/s$ for 60, 100, 200, and 1000 nm nanoparticles, respectively). PS-PEG MSD profiles similarly decreased with increasing size (diffusion coefficient CIs 1.2952-1.2954, 2.078×10^{-1}-2.081×10^{-1}, 1.0596×10^{-1}-1.0602×10^{-1}, 1.45×10^{-2}-1.51×10^{-2} $\mu m^2/s$ for 60, 100, 200, and 1000 nm nanoparticles, respectively). In all cases, PS-PEG nanoparticles had higher diffusion coefficients than their size-equivalent PS-COOH counterparts.

Similar to the results in the gel model, it is difficult to parse out all the contributors to the reduced diffusion coefficients of PS-COOH nanoparticles when compared with PS-PEG nanoparticles. Both particle-particle interactions (resulting in aggregation) and particle-microenvironment interactions (resulting in deposition) both play a role. In order to determine if differences in diffusive behavior can be accounted for by altered aggregation states when particles are administered to tissue, while ignoring many of the particle-environment factors, we plotted the hydrodynamic diameters of PS-COOH and PS-PEG nanoparticles as measured in ACSF (Table A.1) against the measured diffusion coefficients at 1s (Figure 1.9). PS-COOH nanoparticles have increased size in ACSF, indicative of aggregation, as shown in previous data in this paper. There is a linear relationship between the log diffusion coefficient measured in tissue and the log

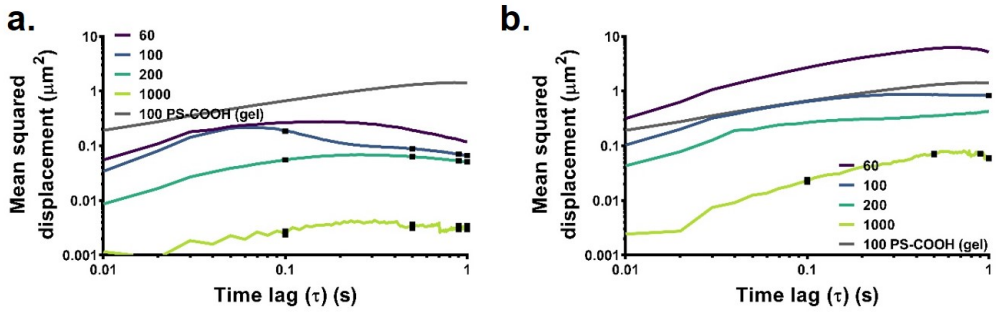

Figure 1.8: MSD profiles in cortex. Data collected using 60 (purple), 100 (blue), 200 (teal), and 1000 nm (lime) (a) PS-COOH and (b) PS-PEG NPs in the cortex region of 300μm-thick brain slices from P14 Sprague-Dawley rats. Data represent the precision-weighted geometric MSD averages over number of videos per slice (n=5) and number of slices per condition (n=3). Error bars at τ = 0.1, 0.5, and 1s represent 95% CIs. MSD values of 100 nm PS-COOH NPs (grey) in agarose gel is provided as a reference in all plots.

hydrodynamic diameter measured in ACSF (R^2 = 0.85). This suggests that the magnitude of the diffusive ability of nanoparticle formulation can be predicted with DLS measurements, particularly for aggregating nanoparticles. We noted that the thresholding phenomenon observed in the gel model was not replicated in the organotypic brain tissue model. Particles in tissue exhibit a more gradual decrease in diffusion coefficients as a function of hydrodynamic diameter when compared to the gel model. However, the same general decreasing trend in diffusion with increasing nanoparticle size is observed. Also, if we apply the threshold value suggested from the gel model (1600 nm), all particles that had hydrodynamic diameters below the indicated threshold had diffusion coefficients greater than 1.0 x 10^{-2} $\mu m^2/s$. The methods used in this paper include both *in vitro* and *ex vivo* techniques, which allows for fine-tuned control of parameters of interest and inclusion of complex biological environments. However, this approach does not account for other factors present in the brain microenvironment, including spatial and temporal changes brought about by normal function (e.g. respiration, sleep), ongoing injury, or development, the presence of proteins in the ECS, and regional differences in brain structure and function. Each of these additional functionalities can be incorporated into gels as advancements in biomaterials continues to grow [117–121]. Future studies can examine the competing kinetics of nanoparticle transport with aggregation effects. In the brain microenvironment, aggregation occurs simultaneously with particle transport through the tis-

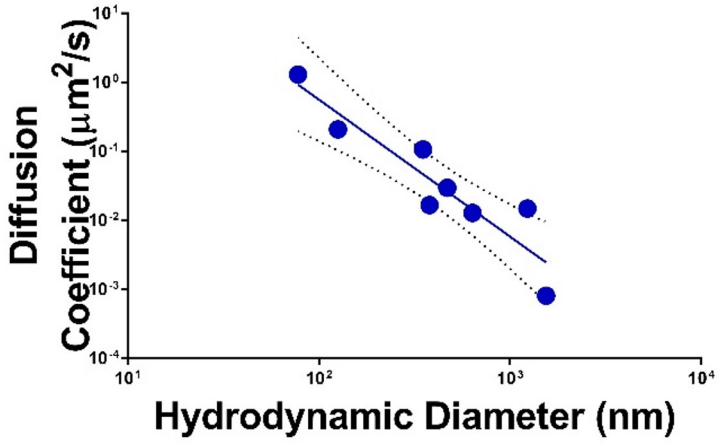

Figure 1.9: Diffusion coefficients of 60, 100, 200, and 1000 nm PS-COOH and PS-PEG NPs as measured in the cortex region of 300μm-thick brain slices from P14 Sprague-Dawley rats as a function of the hydrodynamic diameter measured in ACSF at 37°C. The data includes a linear fit (solid line) on the log transform of both the diffusion coefficients and the hydrodynamic diameters. Error bars represent 95% confidence intervals (dashed lines) of the linear fit.

sue. A theoretical model of nanoparticle diffusion in porous media with simultaneous aggregation could explore the effects of pore size, nanoparticle size, and rate of aggregation on nanoparticle diffusion. Previous studies have examined the effect of aggregate size on cellular uptake and toxicity [122], but little is known about how aggregation effects change as nanoparticles partition or permeate across a boundary and through a tissue environment. Future *ex vivo* and *in vivo* experiments could look at the effect of cellular uptake, intracellular and intra-organelle aggregation.

1.3 Conclusion

Characterization of nanoparticles in standard media, as well as in biological milieu at physiologically relevant conditions, can reduce the number of *ex vivo* and *in vivo* tests that are necessary to evaluate nanoparticle behavior in vivo. Importantly, systematic characterization of colloidal stability can be extended to pathological conditions, which can have implications for nanoparticle behavior in diseased states. For

example, it is known that calcium regulation in the brain ECS is altered in neuroinflammation, neurodegeneration [103], and brain aging [97], all of which could affect nanoparticle aggregation kinetics. In addition, nanoparticles have also been used for intracellular targeting, including mitochondria, lysosomes, and the nucleus [123]. Factors such as calcium and pH are highly variable in these intracellular compartments due to cellular control mechanisms [124, 125], indicating that stability should be assessed based on the relevant target conditions for the nanoparticle. Colloidal stability of nanoparticle formulations in physiologically relevant media can significantly affect the diffusive behavior of nanoparticles in the brain microenvironment, and by extension, delivery of therapeutic payloads to targets of interest in the brain.

In this section, we have demonstrated one example of how fundamental knowledge of nanoparticle-environment interactions (in this case, colloidal stability) can be used to guide the rational design of nanotherapeutics. Researchers do not need to carry out full-scale animal studies to determine that the colloidal instability of a potential nanotherapeutic platform will hinder its performance. Such fundamental knowledge can be used to develop better models of nanoparticle-microenvironment models as well as to build batteries of screening tests for nanoparticle platforms.

2

Predicting in situ nanoparticle behavior using multiple particle tracking and artificial neural networks

2.1 Introduction

Nanotherapeutics have shown promise in their ability to enhance the efficacy of small molecule drugs and biologics in vivo, either through improved targeting, reduced toxicity, or enhanced stability [126]. Since the FDA approval of liposomal doxorubicin in 1995 as a nanotherapeutic, 50 new nanoparticle-

based drugs have entered the market, as of 2016 [127]. Yet an unrealized promise of nanotherapeutics is the ability to decouple transport properties from their therapeutic effect. A better understanding of this relationship would allow researchers to make precision changes to nanotherapeutic characteristics to tune delivery and provide the most efficacious formulation for the target disease without needing to change the therapeutic agent. In order to achieve successful delivery, a nanoparticle formulation must be optimized to achieve localized delivery, evade immune detection, cross biological barriers, and minimize off-target effects [4]. Many studies have investigated nanoparticle transport methods using empirical approaches to measure nanoparticle transport properties in in vitro, *in vivo* and *ex vivo* models [11, 49, 128], while others have developed theoretical and computational models examining local phenomena and systems-wide behavior [129, 130]. A fourth paradigm that we seek to implement here is the use of machine learning methods on large (10^4-10^6 trajectories) experimental datasets of nanoparticle transport properties in *in vitro* and *ex vivo* models to build predictive models of nanoparticle behavior.

Multiple particle tracking (MPT) is a characterization technique used in many biological domains. MPT relies upon tracking the microscopic motion of hundreds to thousands of individual particles simultaneously in real-time using video microscopy. Investigators can use the resulting nanoparticle trajectory datasets to obtain mean-squared displacements profiles and diffusion coefficients (D_eff) as well as geometric features such as trajectory boundedness and asymmetry. MPT is responsible for a number of discoveries, including the mechanical properties of living cells [131], size selectivity of mucosal layers [132, 133], and extracellular pore size of various tissues [48, 49]. Collectively, these findings give insights into design principles that result in optimal delivery to target sites. However, these datasets mostly take the form of heuristics rather than empirical and theoretical models that can be optimized with computational approaches. This leaves a large unexplored design space and opportunity for more comprehensive and adaptive models of nanoparticle property-environment interaction systems.

The use of trajectory datasets from MPT has primarily been limited to calculating ensemble-level D_eff and MSD profiles. As MPT datasets can be quite large (10^2-10^5 trajectories per experiment), they are a clear candidate for the incorporation of data science methods to investigate trends and make predictions. In this paper, we use neural networks (NNs) to predict both nanoparticle properties and properties of

the surrounding microenvironment from input nanoparticle trajectory datasets. From experimentally generated nanoparticle trajectories, we demonstrate the ability to predict nanoparticle size, whether or not a nanoparticle has been internalized by a cell, and whether or not a particle was pre-incubated with serum prior to use. This is non-trivial, due to the heterogeneity of nanoparticle behavior and the interacting effects of nanoparticle properties and the microenvironment on nanoparticle transport. Further, we introduce a collection of MPT and downstream analysis tools in a Python-based diff_classifier package for high-throughput analysis of nanoparticle diffusion datasets.

2.2 Results and Discussion

2.2.1 Neural network predictors of nanoparticle size using MPT datasets

First, we sought to examine whether machine learning techniques can be used to distinguish nanoparticle properties from MPT trajectory datasets. We selected nanoparticle size, a nanoparticle property which can directly correlate to diffusive behavior with theory. We performed diffusion experiments in 0.4% agarose gels using three different diameters of PS-COOH nanoparticles: 100, 200, and 500nm (Figure 2.1a). Hydrodynamic size distributions of each particle type were obtained via DLS and are shown in Figure 2.1b. An initial comparison of geometric ensemble averaged mean squared displacement (MSD) profiles is shown in Figure 2.1c. For spherical particles diffusing in a free media, particle radius r is related to diffusion coefficient D by Stokes-Einstein:

$$D = \frac{k_B T}{6\pi\eta r}$$

where k_B is Boltzmann's constant, T is the absolute temperature, and η is the dynamic viscosity. In porous media such as agarose, the diffusion coefficient is referred to as an effective diffusion coefficient, D_eff, and takes into account the gel's tortuosity λ, a parameter describing the hindrance a particle experiences relative to diffusion in free media [134]:

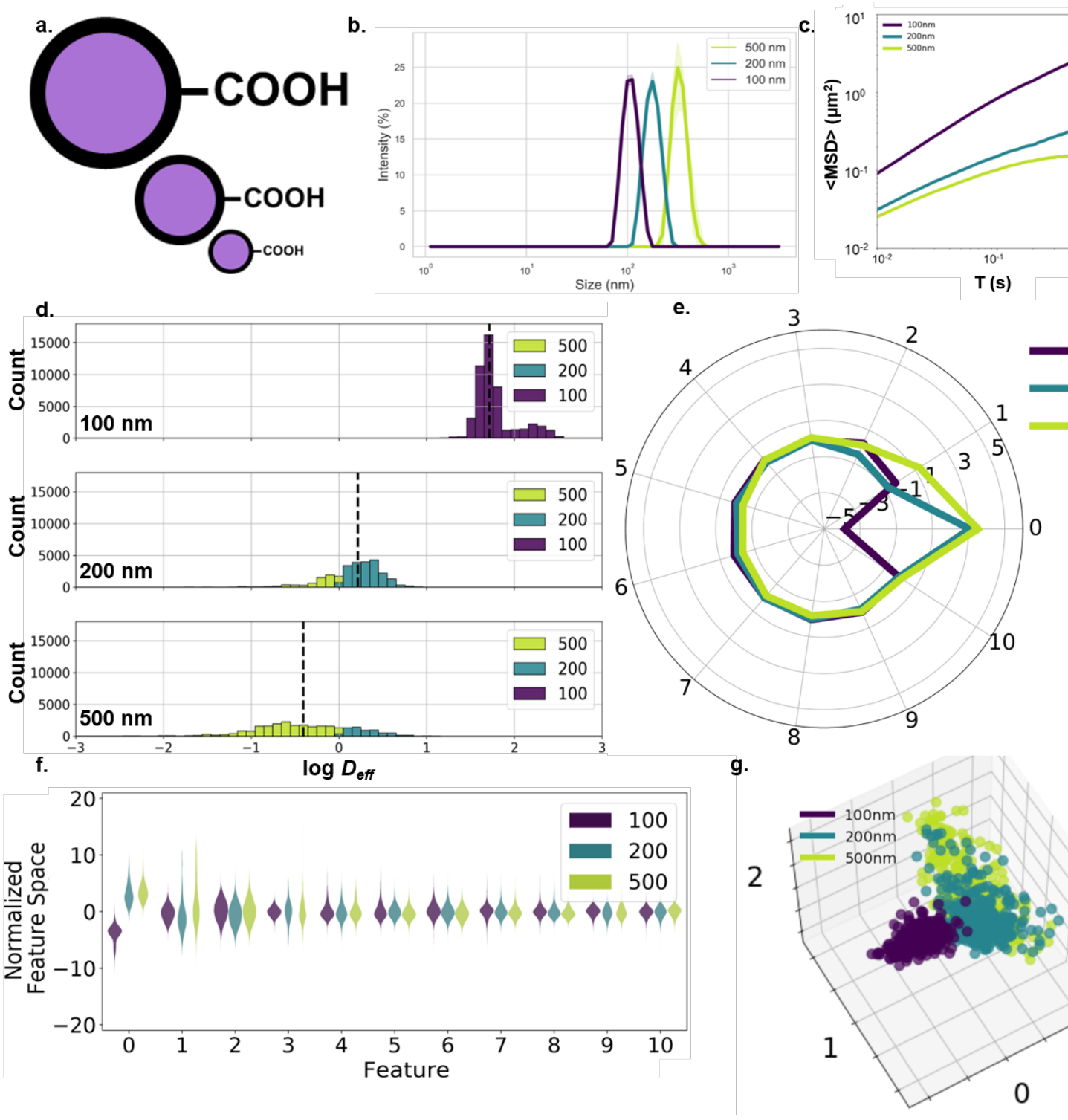

Figure 2.1: Size-dependent nanoparticle diffusion analysis. (a) 100-, 200-, and 500-nm carboxyl-modified polystyrene particles. (b) Hydrodynamic diameter (intensity mean) distributions (purple: 100nm, teal: 200nm, yellow-green: 500nm) measured in 10mM NaCl (n=3 measurements). (c) <MSD> profiles of PS-COOH nanoparticles of varying size. (d) Log Deff distributions stratified by particle size and binned by predicted particle size using the Stokes-Einstein based predictor with anomalous diffusion exponent. (e) Average component profile of PCA analysis stratified by particle size. (f) Principle component distributions of PCA analysis stratified by particle size. (g) The first three primary components of 400 randomly

$$D_{eff} = \frac{D}{\lambda^2}$$

For the purposes of our predictor, we initially assumed a tortuosity value of 1 ($D_{eff} = D$), due to the low concentration of agarose used in our studies. As expected from Stokes-Einstein, the particles' diffusive ability decreased with increasing particle size. The populations were distinct enough that particle size could be predicted with some accuracy without any additional information, using D_eff only. By using Stokes-Einstein to calculate particle size based on D_eff at a time lag of 100ms and binning trajectories into three groups (<150, 150-350, and >350nm), we built a predictor that achieved an average recall score (a non-binary version of the sensitivity, the ability of the classifier to find all positive samples) of 0.636 (Table 2.1). In the case of larger particle sizes (200nm and 500nm), the predictor overestimated D_eff. This resulted in higher recall values for 500nm nanoparticles (0.888) at the expense of lower recall values for 200nm nanoparticles (0.278).

In order to improve the performance of the predictor, we altered our analysis in two ways: first, the way the dataset was split into training and test populations was changed. Second, the assumption of no tortuosity ($\lambda = 1$) was re-examined. When selecting a training-test split, we chose to split the test dataset spatially based on the coordinates of the input trajectories in a checkerboard pattern rather than a random train-test split for two reasons: first, later predictors rely on locally averaged features. Using random train-test splits would cause contamination of the training dataset with information from the test dataset due to the use of local feature averages as inputs. Second, the spatial train-test split reflects more accurately sample-to-sample variability. Due to inherent batch-to-batch variability in gel samples (14), the predictor can be over-trained if not enough independent samples are included in the training dataset. While each square region isn't an independent sample, there are regional differences that are better accounted for by a spatial split rather than a random split. For a more accurate estimate of tortuosity, we selected λ values for the predictor by minimizing the difference between median log D_eff in each particle strata in the training dataset and the log D_eff predicted by Stokes-Einstein. This resulted in a λ value of 1.33 and a predictor that achieved an average recall score of 0.703 in the test dataset, with recall scores of 0.457 for 200nm nanoparticles and 0.744 for 500nm nanoparticles (Table 2.1). By accounting for tortuosity, the Stokes-

Einstein predictor improved overall predictive power by increasing the number of correctly identified 100nm and 200nm nanoparticles (22% and 64% increase, respectively) at the expense of mislabeling a small percentage of 500nm nanoparticles (16% decrease).

The Stokes-Einstein based predictor was further improved by calculating D_eff based on local averages over 9μm x 9μm windows rather than D_eff of individual trajectories. Each video was split spatially into 256 9μm x 9μm regions and the average features in each region were calculated. Each trajectory was then characterized by a locally averaged D_eff within its corresponding region. This minimized some of the noise inherent in MPT datasets. Using the updated local averaging/anomalous diffusion configuration, we performed a regional training-test split like the one performed previously and found a λ value of 1.26 for the training dataset. The new predictor achieved an average recall score of 0.829 in the test dataset (Table 2.1). While this exceeds the performance of a random guess (recall score of 0.333), such accurate results would not carry over to experiments with a wider range of particle sizes. For example, samples with intermediate particles sizes (such as the 200nm particles with a recall score of 0.726) are difficult to distinguish due to high variances in D_eff distributions. Additionally, the ability to resolve trajectories will also be limited at the large nanoparticle limit as the distance travelled by the nanoparticle approaches the image resolution (0.07 μm/pixel for all videos in this paper). We aimed to improve performance by accounting for factors other than the raw D_eff and incorporating a machine learning model.

Table 2.1: Classifier metrics using nanoparticle trajectories to predict particle size in agarose gels

	Sample Size		Stokes-Einstein	Stokes-Einstein (anomalous)		Stokes-Einstein (anomalous) (local avg)		Neural Network (local avg)	
	Training	Test	Overall	Training	Test	Training	Test	Training	Test
100 nm	49041	48854	0.743	0.908	0.908	1.000	1.000	1.000	1.000
200 nm	29231	27878	0.278	0.448	0.457	0.715	0.726	0.914	0.856
500 nm	28493	26459	0.888	0.721	0.744	0.723	0.762	0.931	0.852
Avg/Tot	106765	103191	0.636	0.692	0.703	0.813	0.829	0.999	0.902

In addition to generating profiles and raw D_{eff} distributions, 17 distinct features were calculated for each individual trajectory (Table B.1). A principle component analysis (PCA) was then run on the composite dataset of individual features and locally averaged features. The sampling adequacy was verified via the Kaiser-Meyer-Olkin (KMO) criterion (KMO = 0.919). PCA yielded 11 primary components to achieve 81.3% explained variance. Average component scores and component distributions from the PCA are shown in Figure 1e-f. Using the first three components, each particle type forms distinct clusters (Figure 1g). There is very little overlap between the three populations, with a distinct boundary between the 100nm population and the 200 and 500nm populations.

Using all 51 components as inputs (17 individual trajectory features and 34 locally averaged features), we built a NN classifier using the checkerboard train-test split described above. The NN classifier was able to predict particle size with a 0.902 average recall score in the test dataset, with recall scores of 1.000, 0.856 and 0.852 for the 100nm, 200nm and 500nm nanoparticles, respectively (Table 2.1). By implementing a NN using trajectory feature datasets, we were able to achieve high predictive ability in determining nanoparticle size.

The ability to resolve particle sizes at the micron level in an *in vitro* model of the brain microenvironment demonstrates one aspect of the utility of nanoparticles as probes. We were able to directly compare NN performance with expected results from theory. Similar NN predictors could be used to predict particle size of polydisperse samples in complex media environments. For example, users could track changes in particle size distributions during an aggregation event. NN predictors could prove useful in cases where size measurements are required, but nanoparticle samples cannot be extracted for measurement by standard techniques, such as dynamic light scattering. Additionally, size could be quantified in environments not suitable for size measurements, such as gels or *ex vivo* tissue slices, as demonstrated in this study.

2.2.2 Neural network predictors of nanoparticle surface functionality and protein corona in an *in vitro* agarose gel model

Next, we wanted to predict a more nuanced nanoparticle property using MPT datasets. It is known that in biological environments, the properties of the nanoparticle surface affect its ability to diffuse [48, 49, 135]. However, to our knowledge, there are no theoretical or empirical models relating the diffusive properties of a nanoparticle to its surface functionality or material properties. As surface properties are a more multi-dimensional feature space (e.g. surface charge, hydrophobicity, ligand density) and oftentimes depend on the surrounding environment, it is difficult to create a model accounting for all possible permutations [4]. We chose to examine the effect of two nanoparticle properties on their diffusive ability: surface PEGylation and adhered surface proteins. Nanoparticle PEGylation is a common method used to evade the immune system [136], as well as to improve colloidal stability [54]. PEGylation has also been shown to improve the ability of nanoparticles to penetrate complex systems, including mucus [135], vitreous [48], tumors [137], and the brain parenchyma [138]. In biological environments, nanoparticles accumulate a layer of proteins known as the protein corona [71, 139]. This can alter aggregation rates, cell internalization, and transport properties [140]. For instance, protein coatings have been demonstrated to increase the time scale over which nanoparticles interact with cells [141] and strongly reduce nanoparticle adhesion to cellular surfaces [142]. We incubated PS-COOH and PS-PEG nanoparticles in horse serum to create a protein corona on the particle surface. DLS measurements quantified a change in particle size and zeta potential. PS-COOH nanoparticles increased in size from 142.0 ± 4.2 to 2583 ± 441nm and ζ-potential increased from -40.4 ± 2.8 to -12.3 ± 1.2mV; PS-PEG nanoparticles increased in size from 163.2 ± 1.5 to 408.2 ± 87.7nm and ζ-potential decreased from -6.2 ± 2.5 to -9.4 ± 0.9mV (Figure 2.2b-c). We further confirmed protein adhesion via bicinchoninic acid (BCA) assay. An average of 47.0 ± 2.5 x 10-11μg protein was found on the surface of each PS-COOH nanoparticle compared to 10.0 ± 0.3 x 10-11 μg/particle for PS-PEG nanoparticles (Figure 2.2d). We hypothesized that the protein corona would change how the nanoparticles behaved in the agarose matrix, exhibiting higher D_{eff} than non-coated particles due to reduced interactions with agarose chains. MPT experiments resulted in profiles of similar magnitudes (Figure B.1a), with geometric ensemble-averaged D_{eff} at τ=1s of 0.74 and 1.07 μm2/s

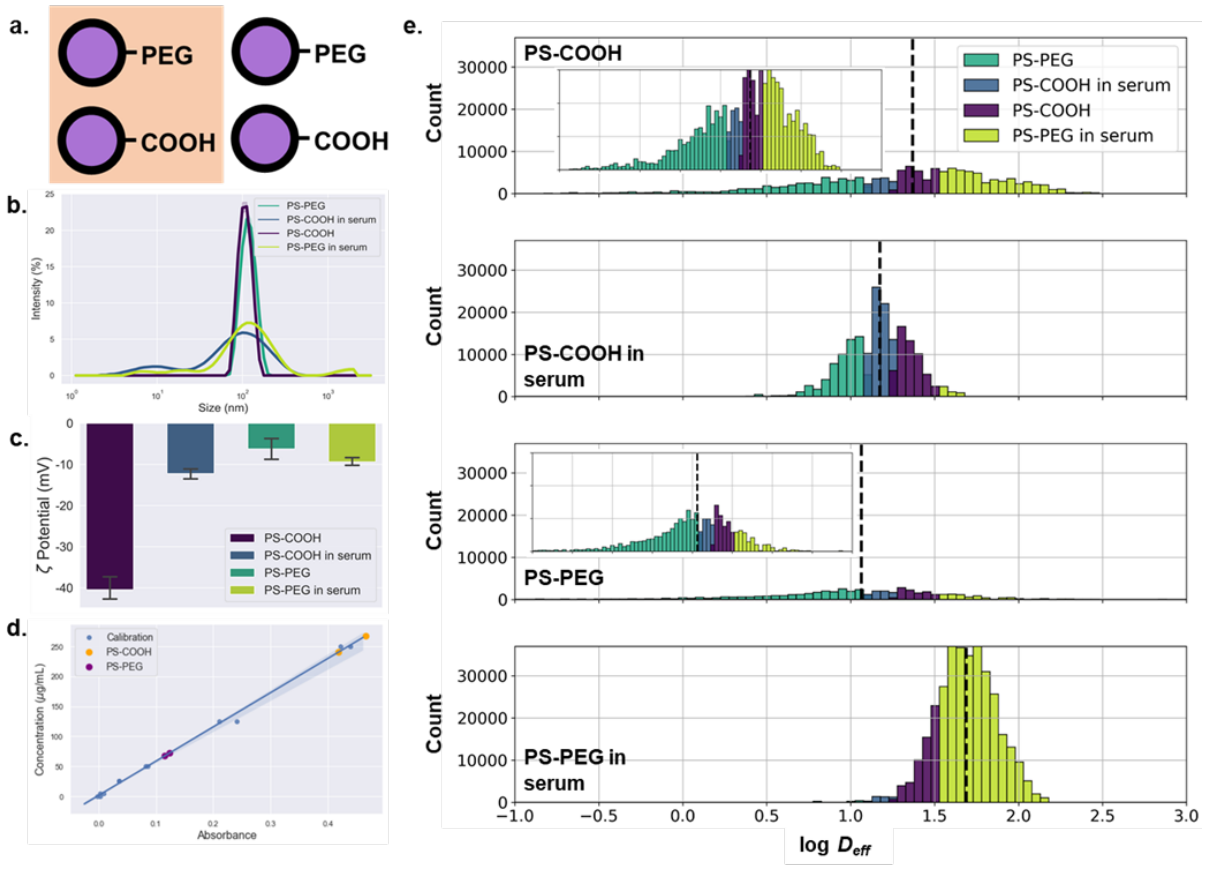

Figure 2.2: Particle surface property-dependent nanoparticle diffusion analysis. (a) Carboxyl- and PEG-modified polystyrene nanoparticles incubated with and without horse serum. (b) Hydrodynamic diameter (intensity mean) distributions (purple: PS-COOH, teal: PS-PEG, blue: PS-COOH in serum, yellow-green: PS-PEG in serum) measured in 10mM NaCl (n=3 measurements). (c) Concentration of surface-adhered proteins from horse serum-incubated PS-COOH (orange) and PS-PEG (purple) nanoparticles determined using BCA assay. UV-Vis adsorption calibration curve generated from BSA standards is shown in blue. (d) Log Deff distributions stratified by particle type and binned by predicted particle type using log median predictor.

for serum-free and serum-incubated PS-COOH nanoparticles, respectively, and 0.93 and 1.78 $\mu m^2/s$ for serum-free and serum-incubated PS-PEG nanoparticles, respectively. The serum-incubated particles had higher diffusivities when compared with particles not incubated in serum, especially in the case of PS-PEG nanoparticles. The higher diffusivities of serum-incubated particles in agarose gels align with previous *in vitro* cell experiments performed by Lesniak *et al* [142]. In non-aggregating conditions, PS-PEG and PS-COOH have been shown to have diffusive behavior of similar magnitudes [54], and our findings match these previous results.

With the resulting trajectory feature datasets, PCA was performed as described above for the size-dependent study. The sampling adequacy was verified via the KMO criterion (KMO = 0.864). The PCA yielded 13 primary components to achieve 81.2% explained variance. Average component scores and component distributions from the PCA are shown in Figure B.1b-c. Using the first three components, each particle type formed distinct clusters as shown in Figure B.1d.

Table 2.2: Classifier metrics using nanoparticle trajectories to predict particle type in agarose gels

	Sample Size		Median Predictor		Median Predictor (local avg)		Neural Network (local avg)	
	Training	Test	Training	Test	Training	Test	Training	Test
COOH	134717	135518	0.001	0.001	0.329	0.193	1.000	0.902
COOH in serum	191947	191654	0.022	0.022	0.357	0.500	1.000	0.916
PEG	52038	51917	0.065	0.066	0.166	0.290	0.998	0.741
PEG in serum	351935	352061	0.103	0.103	0.828	0.821	1.000	0.981
Avg/Tot	730637	731150	0.048	0.048	0.420	0.451	0.998	0.885

Using a trained NN, we predicted particle type (PS-COOH, PS-COOH in serum, PS-PEG, and PS-PEG in serum) with an average recall score of 0.885 in the test dataset (Table 2.2). This demonstrates the predictive power that can be leveraged when using trajectory features other than just D_eff, as implemented in the Stokes-Einstein size predictors in the previous experiment. A predictor based on log median D_eff using locally averaged trajectory features is not able to parse out these differences, with an average recall

score of 0.427 (Table 2.2). As the profiles are of similar magnitude for all four particle types (Figure 2.2).

The fact that such nuanced nanoparticle properties such as surface functionality and protein adsorption can be resolved using an indirect measurement technique such as MPT is very promising. This leaves room to probe additional nanoparticle properties, such as the effect of nanoparticle composition, shape, density, and porosity on nanoparticle transport behavior. Additionally, this method can be extended to provide systems-wide predictive models that account for a host of particle parameters.

2.2.3 Neural network predictors of nanoparticle surface functionality and protein corona in an *ex vivo* brain tissue slice model

While we have demonstrated the ability to differentiate between nanoparticle properties using MPT datasets and NNs, we wanted to test to what extent such predictive ability was preserved in a more physiologically relevant model. Agarose gels can capture some aspects of the tissue microenvironment, such as ionic composition and viscoelastic properties, but they are not dynamic and neglect interactions with cells and proteins. We hypothesized that MPT could also be used to detect the extent of these interactions, given that protein adsorption has been shown to decrease nanoparticle interactions cell membranes [142]. Both a computational and experimental approach were used to test this hypothesis. Computationally, we used a random walker model where nanoparticles were capable of adhering to cells, modeled as squares, to demonstrate the impact that adhesion interactions of varying strength have on ensemble-averaged MSD profiles (Figure 2.3b). Adhesion interactions are represented as the probability a random walker will "stick" when encountering a surface while diffusing. When this sticking probability increased (10%, 20%, 30%, 50%, 75%, 90%, 99%), the D_{eff} decreased by a factor of 0.00, 0.01, 0.02, 0.02, 0.05, 0.27, and 5.56, respectively, when compared to particles with a sticking probability of 1%. We repeated this experiment with a 2-fold narrower spacing between "cells," and it resulted in an even stronger effect. In this scenario, D_{eff} decreased by a factor of 0.00, 0.00, 0.04, 0.05, 0.18, 0.47, and 14.07 when compared to particles with a sticking probability of 1%.

To capture some of the biological effects ignored by the agarose gel model, an *ex vivo* rat brain slice model

was used. Unlike in the gel experiment, we saw a bifurcation between PS-COOH and PS-PEG particles. We calculated geometric ensemble-averaged D_{eff} at τ=1s of 0.0093 and 0.018 μm2/s for serum-coated PS-COOH and serum-free PS-COOH, respectively, and D_{eff} of 0.61 and 0.22 μm2/s for serum-coated PS-PEG and serum-free PS-PEG, respectively (Figure 2.3d). In tissue, the PS-COOH particle types with and without serum were more immobile compared to gel studies. Here, we calculated D_{eff} of 0.0093 and 0.018 μm2/s for serum-coated PS-COOH and serum-free PS-COOH, respectively, in tissue, and 1.07 and 0.74 $\mu m^2/s$ for serum-coated PS-COOH and serum-free PS-COOH, respectively, in gels. This has been shown in previous experiments, as PS-COOH nanoparticles are subject to both electrostatic and hydrophobic interactions with various components of the brain microenvironment, hindering their diffusive ability [54]. Contrary to experiments run in gel, the protein corona did not uniformly increase ensemble nanoparticle diffusive behavior. On average, serum-incubated PS-COOH nanoparticles had lower MSD profiles than their serum-free counterparts, while incubation with serum increased the diffusivities of PS-PEG nanoparticles (Figure B.2a). To explain this diverging behavior in nanoparticle diffusion, fluorescence activated cell sorting (FACS) was used to evaluate the cellular uptake profiles of each type of nanoparticle (Figure 2.3c; example raw FACS data found in Figure B.3). It was determined that 8.7 ± 0.8% of Cd11b+ macrophages took up PS-PEG nanoparticles, compared to 2.0 ± 0.3% for serum-incubated PS-PEG nanoparticles. The opposite effect was observed for PS-COOH nanoparticles, where 12.2 ± 1.7% of macrophages took up the serum-free PS-COOH nanoparticles compared to 21.3 ± 1.0% uptake for serum-incubated PS-COOH particles. Particles confined in cells and internal cellular compartments have restricted trajectories and reduced D_{eff}, suggesting that any differences we observed in *ex vivo* particle behavior could in turn be caused by cellular internalization [56].

The sampling adequacy was verified via the KMO criterion (KMO = 0.907). The PCA yielded 12 primary components to achieve 80.9% explained variance. Average component scores and component distributions from the PCA are shown in Figure B.2b-c. We plotted the first three components against each other in Figure B.2d, where we saw significant overlap between the four populations, and the serum-incubated PS-PEG population was difficult to distinguish. Using all 51 components as inputs, we built a NN classifier that was able to predict particle type with a 0.591 average recall score in the test dataset (Table 2.3).

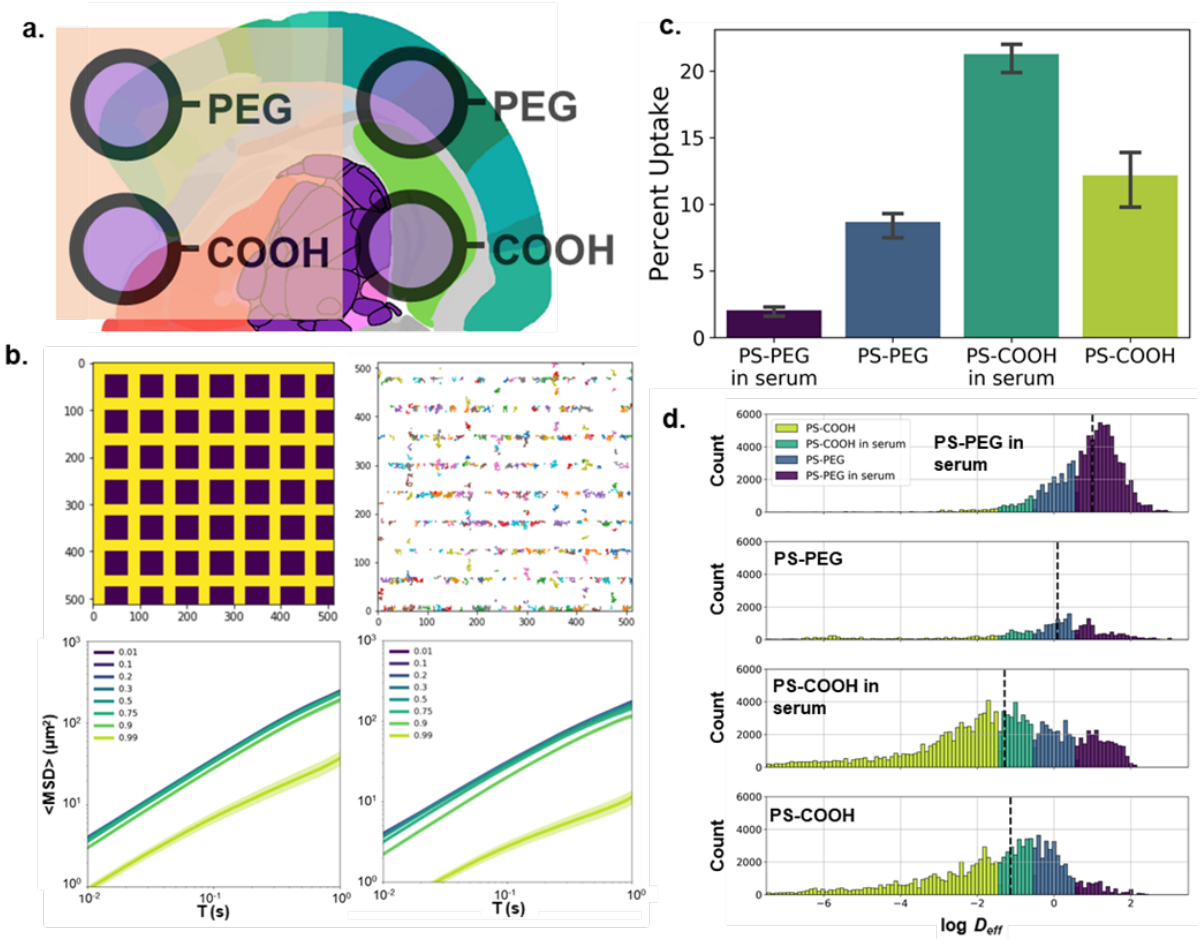

Figure 2.3: Particle surface property-dependent nanoparticle diffusion analysis in an organotypic brain slice model. (a) Carboxyl- and PEG-modified polystyrene nanoparticles incubated with and without horse serum were allowed to diffuse in rat brain slices. (b) (top left) 2D computational diffusion model varying the "stickiness" of cellular surfaces (purple squares: cells). (top right) Example nanoparticle trajectories. (bottom left) <MSD> profiles as a function of cell "stickiness". Stickiness was quantified as the probability a particle remains adhered to a cell's surface when in contact with the cell boundary (distance between cells: 20 pixels), (bottom right) <MSD> profiles as a function of cell "stickiness" (distance between cells: 10 pixels) (c) FACS results quantifying cell uptake of nanoparticles in microglia stratified by particle type (n=3 slices per condition, purple: PS-PEG in serum, blue: PS-PEG, teal: PS-COOH in serum, yellow-green: PS-COOH) (d) Log Deff distributions stratified by particle type and binned by predicted particle size using log median predictor.

Our ability to predict particle type accurately was significantly reduced in comparison to the results in gels. This is partly due to the more significant inter-sample variation in particle behavior. A major contributor to the poor performance of the NN classifier was the inability to distinguish the PS-PEG population, which had a recall score of 0.283. This method does outperform a classification based on binning by median D_{eff} (Figure 2.3d) with an average recall score of 0.110 in the test dataset. While it is reassuring that the predictor can still make accurate predictions despite intra-sample variability, it also raises concerns whether this prediction would be reproducible across slices outside of the training dataset.

Table 2.3: Classifier metrics using nanoparticle trajectories to predict particle type in organotypic brain slice model

	Sample Size		Median Predictor (local avg)		Neural Network (local avg)		Neural Network (local avg) (avg 3-1 train-test)		Neural Network (COOH only) (local avg) (avg 3-1 train-test)		Neural Network (PEG only) (local avg) (avg 3-1 train-test)	
	Training	Test	Training	Test	Training	Test	Training	Test	Training	Test	Training	Test
COOH	88001	86429	0.082	0.075	0.773	0.593	0.807	0.473	0.886	0.536	NA	NA
COOH in serum	138913	142066	0.176	0.172	0.842	0.687	0.878	0.548	0.936	0.640	NA	NA
PEG	35969	36864	0.142	0.171	0.438	0.283	0.517	0.065	NA	NA	0.658	0.258
PEG in serum	95111	93907	0.029	0.023	0.879	0.800	0.878	0.641	NA	NA	0.967	0.908
Avg/Tot	357994	359266	0.107	0.110	0.838	0.591	0.770	0.432	0.911	0.588	0.812	0.583

In order to test the ability of our NN to predict particle type in slices not included in the training dataset, we selected a new training/test configuration. We trained our NN on 3 of 4 slices for each particle type and reserved one slice as a test dataset. This was repeated four times, such that each slice was used once as a test dataset. In this case, we were able to retain some of our predictive ability. We generated a range of average recall scores of 0.402-0.513 in the test dataset, but we had a complete loss of predictive ability of serum-free PS-PEG nanoparticles, with a range of recall scores of 0.039-0.105 (Table B.2). If we limit our predictions to incubation status (serum-free or serum-incubated), this configuration provides predictive ability for the test datasets with 0.480-0.706 average recall scores for PS-COOH nanoparticles, and 0.479-0.690 average recall scores for PS-PEG nanoparticles. When predicting serum status in the PS-PEG particle population, our NN configuration still could not resolve serum-free particles, with recall scores of 0.071-

0.535. Our results indicate that while there are measurable differences between particle populations, the amount of inter-sample variability hinders the utility of such predictors. We could resolve this further with very large training datasets, but this is not likely to be a cure-all, as serum-free PS-PEG particles had low recall scores even without accounting for intra-sample variability. As we have demonstrated that there are significant differences in cell uptake between serum-free and serum-incubated nanoparticles, NN predictors could be improved by incorporating information relating to nanoparticle-cell interactions. For instance, complementary histology can be included in input datasets to improve predictive ability.

2.2.4 Neural network predictors of gel stiffness using MPT datasets

Next, we sought to demonstrate that nanoparticle probes can also be used to predict aspects of their surrounding environment. If we could demonstrate that subtle differences in the surrounding tissue microenvironment could be differentiated solely with MPT trajectory datasets, this could potentially be used as a powerful preclinical diagnostic tool. We first chose a simple and controllable model with a tunable parameter: agarose gels with varying agarose concentrations to adjust gel stiffness and porosity. Low concentration agarose gels have been used as a model of brain tissue because they have similar infusion properties [143] and pore sizes [113] to the brain microenvironment. By varying agarose concentration, we can mimic changes in the brain microenvironment that may occur in disease states [144] or aging processes [145]. To model this computationally, we used a random walker model with increasingly densely packed "sticky" particulates to demonstrate the impact of varyingly dense microenvironments on diffusive ability (Figure 2.4b). Particulate concentrations were increased 4-, 8-, 12-, 16-, 20-, 24-, 28-, 32-, and 36-fold in each simulation resulting in 0.09-, 0.20-, 0.32-, 0.71-, 1.15-, 2.01-, 3.45-, 5.81-, and 6.82-fold decreases, respectively, in ensemble-averaged D_eff. This general trend is likely to hold in *in vitro* experiments. We chose a range of agarose concentrations from 0.4 to 1.2 weight % agarose that encompass concentrations found to mimic infusion properties of the brain (25). We chose 0.2% agarose intervals to test the resolution limits of our NN predictors. An oscillatory rheological analysis was performed on each weight % agarose gel to verify the storage moduli increased with increasing agarose concentration (Figure B.5d). An initial comparison of profiles generated from MPT experiments performed in each gel is shown in Figure B.4a. As

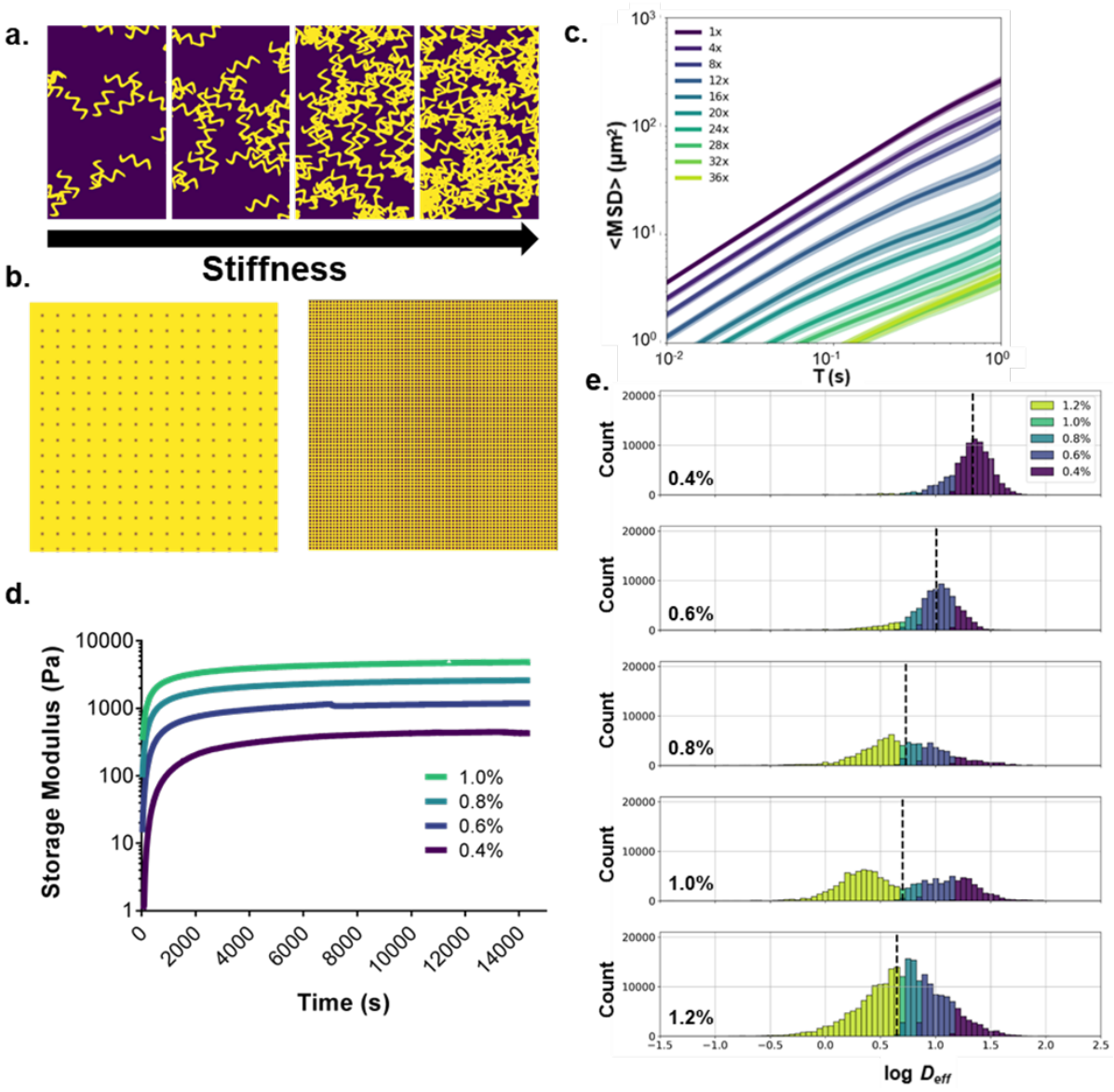

Figure 2.4: Diffusion analysis for the prediction of agarose gel concentration. (a) Schematic representation of the relationship between agarose concentration and gel stiffness. (b) Computational model of diffusion in agarose gel of increasing agarose concentration. Agarose is modeled as 2D squares with sticky surfaces. (c) Computational model generated <MSD> profiles for increasing agarose concentrations. Concentrations represent multiples of the base agarose concentration (256 squares/512 x 512 μm^2) (d) Oscillatory rheological analysis of agarose gels of varying weight percent (e) Log Deff distributions stratified by agarose gel concentration binned by predicted agarose gel concentration using log median predictor.

expected, the nanoparticles' diffusive ability decreased with increasing agarose concentration, with calculated geometric ensemble-averaged D_eff at τ=1s of 0.51, 0.43, 0.23, 0.22, and 0.17 μm2/s for 0.4%, 0.6%, 0.8%, 1.0%, and 1.2% agarose gels, respectively (Figure 2.4d). However, these differences are much smaller in magnitude compared to the differences caused by particle size. Similar to the particle size experiment, we built a baseline predictor using theory with which we could compare the NN predictive ability. The D_eff of nanoparticles diffusing in porous media is related to the volume fraction of polymer gel by the following obstruction scaling model:

$$\frac{D_g}{D_\circ} = e^{\left[-\Pi\left(\frac{r_s+r_f}{k_s a \Phi^{-0.75} C_\infty^{-0.25}(1-2X)^{-0.25}+2r_f}\right)^2\right]}$$

where D_g is the D_eff in the gel, $D_\circ$ is the D_eff in water, r_s is the nanoparticle radius, r_f is the radius of the polymer chain, k_s is a constant of proportionality, α is the equivalent bond length of the monomer, φ is the volume fraction of polymer in the gel, C_∞ is the characteristic ratio of the polymer, and χ is the Flory-Huggins interaction parameter [146]. Using the percent agarose values and the calculated D_eff of the nanoparticle trajectories at τ=100ms, we fit the model using a nonlinear curve fit. We calculated percent agarose concentrations for each trajectory in the whole dataset and binned trajectories into five groups: <0.5%, 0.5-0.7%, 0.7-0.9%, 0.9-1.1%, and >1.1%. This predictor achieved an average recall score of 0.218 (Table 4). If we reduce the resolution and only look at the 0.4, 0.8, and 1.2% samples, we get an average recall score of 0.367, which is not competitive with a random guess, which has an average recall score of 0.333.

If, in addition to reduced resolution, we use locally averaged D_eff, we obtain an average recall score of 0.488. The predictor had the most difficulty predicting intermediate agarose concentrations (e.g. 0.228 for trajectories in 0.8% agarose). Predicting viscoelastic properties of the surrounding media proves to be a more difficult problem than predicting particle size and leaves room for ongoing exploration using a NN classifier on input trajectory datasets.

A PCA yielded 14 primary components to achieve 81.7% explained variance. Average component scores and component distributions from the PCA are shown in Figure B.4b-c. Using the first three compo-

nents plotted against each other, distinct regions can be observed (Figure B.4d), but the intermediate gel viscosities, particularly the 0.6% and 0.8%, are difficult to distinguish visually.

Table 2.4: Classifier metrics using nanoparticle trajectories to predict agarose gel concentration

	Sample Size		Obstr. Model	Obstr. Model (reduced res.)	Obstr. Model (local avg.)	Obstr. Model (reduced res.) (local avg.)	Neural Network (local avg.)		Neural Network (local avg.) (reduced res.)	
	Training	Test	Overall	Overall	Overall	Overall	Training	Test	Training	Test
0.4	44643	45388	0.409	0.420	0.622	0.712	0.910	0.695	0.992	0.834
0.8	42941	41812	0.060	NA	0.235	NA	0.843	0.486	NA	NA
0.6	46913	45652	0.164	0.316	0.121	0.228	0.805	0.329	0.974	0.569
1	63001	65820	0.151	NA	0.027	NA	0.880	0.395	NA	NA
1.2	122390	121818	0.304	0.365	0.502	0.524	0.972	0.702	0.996	0.837
Avg/Tot	180610	181437	0.218	0.367	0.302	0.488	0.882	0.521	0.987	0.747

Using all 51 components as inputs, we built a NN classifier that was able to predict agarose concentration with a 0.521 average recall score in the test dataset (Table 2.4). The predictor was able to resolve trajectories in both high and lower agarose concentrations, with recall scores of 0.695 and 0.702 in 0.4% and 1.2% agarose, respectively. However, the NN predictor lost power at intermediate agarose concentrations, with recall scores of 0.486, 0.329, and 0.395 for 0.6, 0.8, and 1.0% agarose concentrations, respectively. If we reduce the resolution and only include 0.4, 0.8, and 1.2% samples, we achieved an average recall score of 0.747 in the test dataset. This predictor still suffers at intermediate concentrations with a 0.569 recall score for 0.8% agarose, but the NN is still able to outperform the obstruction model predictor. This demonstrates the potential power of using trajectory datasets to predict aspects of the surrounding environment. Additional factors that could be probed are changes in surface charge and hydrophobicity of gel components, heterogeneity of gels, and the composition of the surrounding media.

2.2.5 Neural network predictors of nanoparticle surface functionality and cell uptake status using MPT datasets

Next, we wanted to attempt to build a predictor that would be able to distinguish both nanoparticle properties and aspects of the surrounding environment simultaneously. Nanoparticle behavior is a function of the surrounding environment, and if we hope to build predictive models that are useful in more complex environments, it is important that we can capture these interactive effects. We sought to demonstrate the ability to predict particle internalization into a cell by using trajectory feature datasets using two different particle types, PS-COOH and PS-PEG. Even without accounting for the complex biology involved, we can predict distinct diffusive behavior due solely to geometric constraints. For example, Brownian motion confined to a circle of radius r_c^2 can be modeled by:

$$\langle r^2(n) \rangle = r_c^2[1 - A_1 e^{-4A_2 Dn \quad t/r_c^2}]$$

where D is the D_eff, n is the frame, δt the shutter speed, and A_1 and A_2 are shape constants [56]. Nanoparticles in cells will likely not only be confined within the cell membrane but will also be internalized into organelles, resulting in hindered diffusive behavior [147]. As observed previously, surface charge impacts both interactions with cells and cell uptake profiles. We sought to build a predictor that would be able to determine whether a particle has been internalized based on its trajectory features.

In this experiment, BV-2 cells were exposed to PS-COOH or PS-PEG nanoparticles for 1 h prior to imaging. Using binary images generated from brightfield images of cells taken directly after tracking experiments (Figure 2.5b-c), trajectories were labelled as either "in cells" or "out of cells." Ensemble-averaged MSDs of PS-COOH and PS-PEG nanoparticles stratified by cell internalization are shown in Figure B.6a. Nanoparticles in cells consistently had lower D_eff than their uninternalized counterparts. We calculated 0.00088 and 0.69 $\mu m^2/s$ geometric ensemble-averaged D_eff for PS-COOH nanoparticles "in cells" and "out of cells," respectively, and 0.0025 and 1.08 $\mu m^2/s$ for PS-PEG nanoparticles "in cells" and "out of cells," respectively. MSD profiles of non-internalized PS-COOH and PS-PEG cells are of similar magni-

tude. We performed a PCA on the composite dataset of individual features and locally averaged features. The sampling adequacy was verified via the KMO criterion (KMO = 0.948). The PCA yielded 13 primary components to achieve 80.7% explained variance. Average component scores and component distributions from the PCA are shown Figure B.6b-c. Using the first three components, each particle type forms distinct clusters (Figure B.6d), where there is overlap between the four populations, but each population can be resolved visually.

Using all 51 components as inputs we built a NN classifier that was able to predict particle type/cell internalization with a 0.686 average recall score in the test dataset (Table 2.5). Internalized PS-PEG nanoparticles were the most difficult to resolve, with a recall score of 0.412 in the test dataset. This is likely due to three causes: (1) there are very few internalized PS-PEG nanoparticles, and thus a small training dataset (Figure 2.5d), (2) there is less of a binary behavior of PS-PEG nanoparticles "in cells" and "out of cells," and (3) any immobilized PS-PEG nanoparticles in cells are difficult to distinguish from immobilized PS-COOH nanoparticles in cells. While PS-COOH internalized particles are almost uniformly immobile and the non-internalized PS-COOH particles are free to move, the internalized PS-PEG nanoparticles have broader distribution in diffusive behavior (Figure 2.5d). Thus, the internalized PS-PEG nanoparticles can be mistaken by the network for both PS-PEG nanoparticles out of cells and PS-COOH nanoparticles in cells.

We would also like to note that our ability to label particles as internalized and non-internalized is imperfect. Without a highly accurate reference standard, there will be trajectories falsely labelled as internalized due to imperfectly resolved cellular edges and variable particle behavior at cellular interfaces. Other trajectories will be falsely labelled as non-internalized due to thin cellular features that are lost in image processing steps (Figure 2.5c). This will inevitably limit the accuracy of our NN classifier. We were able to improve the performance of our NN classifier by excluding particles near cellular interfaces. When we excluded particles within 10 pixels (0.7 μm), we achieved an average recall score of 0.702 and a recall score of 0.434 for internalized PS-PEG nanoparticles in the test dataset. When we excluded particles within 20 pixels (1.4 μm), we achieved an average recall score of 0.719 and a recall score of 0.439 for internalized PS-PEG nanoparticles in the test dataset. By excluding particles at the interface, we minimize errors due

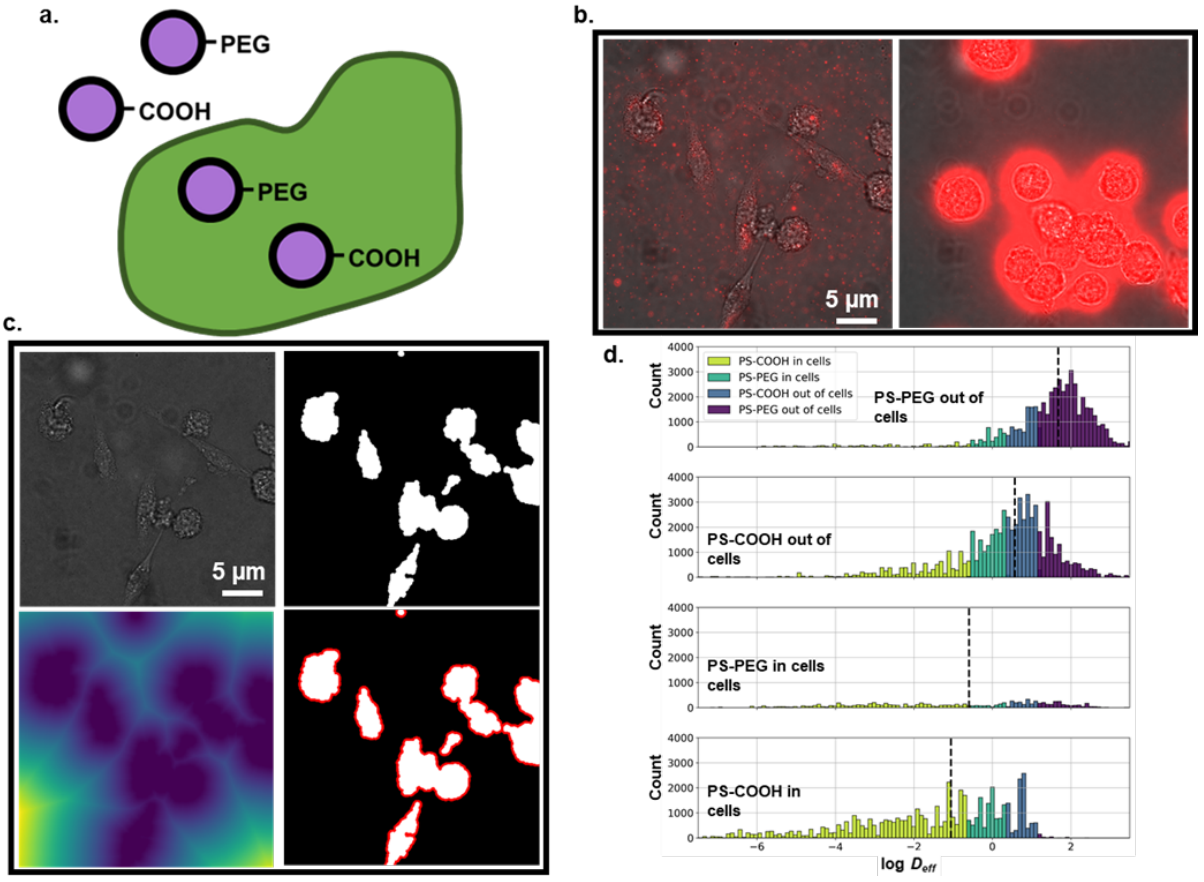

Figure 2.5: (a) Particle type- and cellular internalization-dependent diffusion analysis. (b) (left) Example frame of PS-PEG nanoparticle diffusion in BV-2 microglial cell culture. (right) Example frame of PS-COOH nanoparticle diffusion in BV-2 microglial cell culture. (c) Demonstration of cell image analysis. (top left) Raw image. (top middle) Binarized image. (top right) Euclidean distance transform of binarized image (bottom left). Binarized image with area 10 pixels from cell surfaces highlighted in red. (bottom middle) Binarized image with area 20 pixels from cell surfaces highlighted in red. (d) Log Deff distributions stratified by agarose gel concentration binned by predicted agarose gel concentration using log median predictor (purple: PS-PEG out of cells, blue: PS-COOH out of cells, teal: PS-PEG in cells, yellow-green: PS-COOH in cells).

to variable behavior at cell interfaces and inaccurate binarization of the cellular images.

Table 2.5: Classifier metrics using nanoparticle trajectories to predict particle type and cellular internization status in microglial cell culture

	Sample Size		Median Pred. (local avg.)		Neural Net. (local avg.)		Neural Net. (local avg.) (>10 px)		Neural Net. (local avg.) (>20 px)		Neural Net. (local avg.) (>20 px) (COOH only)		Neural Net. (local avg.) (>20 px) (PEG only)	
	Training	Test	Training	Test	Training	Test	Training	Test	Training	Test	Training	Test	Training	Test
COOH out of cells	65458	65174	0.157	0.170	0.838	0.699	0.898	0.719	0.907	0.734	0.984	0.926	NA	NA
COOH in cells	48825	49832	0.207	0.208	0.935	0.787	0.966	0.804	0.977	0.837	0.982	0.852	NA	NA
PEG out of cells	56517	57097	0.159	0.154	0.946	0.847	0.965	0.850	0.973	0.865	NA	NA	0.985	0.979
PEG in cells	9810	9334	0.276	0.210	0.623	0.412	0.709	0.434	0.754	0.439	NA	NA	0.766	0.724
Avg/Tot	180610	181437	0.200	0.185	0.836	0.686	0.885	0.702	0.903	0.719	0.983	0.889	0.875	0.852

By implementing a NN, we were able to achieve high predictive ability in determining cell internalization based on trajectory datasets. This could be expanded to include internalization in cellular substructures such as lysosomes and vacuoles. In cases where cell stains are available, using this information can allow for more powerful predictive models. For example, instead of predicting cell internalization, investigators could predict whether particles were sequestered in organelles, diffusing in the cytosol, associated with the cell membrane, or embedded in the extracellular matrix. Additional questions could probe the relationship of nanoparticle diffusion to cell type, phenotype, and protein distribution.

2.3 Conclusions

Traditional applications of MPT have an excessively large amount of overhead. For example, a single experiment examining 4 different conditions and 3 replicates per condition can run upwards of 1 terabyte of data. From that terabyte of video, thousands to millions of trajectories are collected, all to report an often ensemble-averaged D_eff value per condition. These large datasets are a prime target for machine learning methods. Trajectory datasets have been used in biological settings, for example, to classify motion types. Additionally, applications outside biomedical fields, including mapping new environments,

learning interactive behaviors from pedestrian trajectories, and training self-driving cars from driver data, suggest there are many methods left untried in this area. Using a range of experiments, we have sought to push the boundaries of the level of information that can be extracted using MPT techniques. In some well-defined cases such as particle size, *in vitro* cell uptake, and *in vitro* protein corona, we were able to achieve powerful predictive models using neural networks. *ex vivo* slice studies exhibited some utility as well, but variability from slice to slice and from animal to animal limited their applicability. We suggested additional ways that these weaknesses can be overcome, for instance, by combining cell histology datasets with trajectory datasets. The use of trajectories as a form of biological marker can potentially become a powerful diagnostic tool without the need of expensive or complicated reagents. Future experiments could seek to implement nanoparticle movement as a surrogate for tissue breakdown, disease severity, tissue age, altered cellular behavior, or protein expression.

3

Tuning design parameters of PEGylated brain-penetrating nanoparticles using artificial neural networks

3.1 Introduction

Nanoparticles have been lauded for their promise in addressing common barriers to effective drug delivery: a lack of sustained or controlled release, biological barriers, and non-specific and off-target effects [148–150]. Yet the translation of nanoparticles from benchside to commercially available drugs has been

slow, partially attributable to a limited knowledge of particle-environment interactions. Efforts to both increase knowledge of nanoparticle behavior in biological environments and improve nanotherapeutic screening times can address this issue [4].

Many studies have examined how one nanoparticle property affects one biological feature or conversely how varying one biological feature changes one nanoparticle behavior. For example, studies have examined how nanoparticle size, surface charge, shape, and surface chemistry affect cell uptake [151–153], nanoparticle distribution [154, 155] and cytotoxicity [156, 157]. A common modulator of nanoparticle behavior is the surface ligand polyethylene glycol (PEG). PEG can be used to improve nanoparticle stability and bequeath stealth properties [158]. Investigators have quantified the effects of PEG grafting density, PEG chain length, and PEG type on pharmacokinetics [159], biodistribution [160], cellular uptake [161–163], and the development of the protein corona [158, 164]. Additional studies have investigated intermediate transport properties of nanoparticles such as how the presence of PEG modifies nanoparticle diffusive behavior in the brain [49], and the role of calcium in changing nanoparticle behavior [54].

In this paper, we sought to further investigate how various aspects of nanoparticle formulations (surface charge, PEG chain length, and PEG surface coverage) affect the ability of nanoparticles to diffuse in the brain. We use a previously developed agarose gel model of the brain that mimics stiffness and pore sizes found in the brain [54]. Furthermore, we sought to apply machine learning techniques to multiple particle datasets to demonstrate that various nanoparticle types can be distinguished solely on geometric trajectory features.

3.2 Results and Discussion

3.2.1 Diffusion studies: Surface charge

We first investigated the effect of surface charge on the ability of a nanoparticle to diffuse in a gel model of the brain. Surface charge effects on diffusion have been documented in a variety of media, including biofilms [165], vitreous [48], mucous [135], and brain tissue [49]. While the effects of surface charge

have been investigated with a variety of techniques, there is still no consensus as to the effects of surface charge on diffusive properties nor the underlying causes [166]. It has been hypothesized that negative surface charges increase diffusion coefficients by reducing interactions with negatively charged cell surfaces while positively charged particles are hindered due to adherence to cell surfaces [49]. It has also been demonstrated that surface charge impacts the colloidal stability of nanoparticles in biological media thus altering diffusion coefficients through an indirect mechanism [54].

Table 3.1: Nanoparticle characterization via dynamic light scattering and NMR

Particle Type	Hydrodynamic Diameter (nm)	Potential (mV)	PEG Surface Density (mol/100nm2)
Functionality	—-	—-	—-
PS-COOH	110.3 ± 2.8	-68.8 ± 1.4	-
PS(COOH)-PEG	124.2 ± 3.3	-2.0 ± 0.1	-
PS-NH2	98.2 ± 10.4	44.4 ± 1.8	-
PS(NH2)-PEG	149.7 ± 5.1	-2.0 ± 0.1	-
Chain Length	—-	—-	—-
PS-PEG(1k)	114.8 ± 1.5	.1.1 ± 0.3	-
PS-PEG(10k)	139.7 ± 3.4	-2.3 ± 0.4	-
Grafting Density	—-	—-	—-
PS-PEG(0.1x)	105.3 ± 3.1	-18.0 ± 1.0	-
PS-PEG(0.15x)	109.2 ± 0.03	-10.1 ± 1.2	-
PS-PEG(0.2x)	90.8 ± 1.9	-9.8 ± 0.4	1.5 ± 0.4
PS-PEG(0.4x)	91.6 ± 3.1	-6.9 ± 1.7	3.7 ± 0.6
PS-PEG(0.5x)	117.7 ± 1.5	-5.1 ± 1.0	5.1 ± 0.7
PS-PEG(0.6x)	92.7 ± 4.7	-3.4 ± 0.2	5.6 ± 0.6
PS-PEG(0.75x)	122.0 ± 0.9	-4.8 ± 0.5	8.8 ± 0.9
PS-PEG(1x)	119.8 ± 0.3	-5.8 ± 0.9	8.5 ± 0.9

Based on these previous studies, we hypothesized that (1) positively charged PS-NH_2 nanoparticles would have little diffusive ability due to adherence to negatively charged agarose chains (ζ-potential of 44.4 ± 1.8, Table 3.1) and (2) that PS(NH_2)-PEG nanoparticles would have diffusive abilities similar to PS(COOH)-

PEG nanoparticles, as both particle types have near-neutral surface charges (ζ-potentials of -2.0 ± 0.1 and -2.0 ± 0.1 mV, respectively). We investigated nanoparticle behavior in 0.4% agarose gel model of the brain constituted with ACSF with 2mM or 3mM calcium chloride. Calcium chloride is a main contributor to colloidal instability of negatively charged nanoparticles such as PS-COOH [54], and we wanted to include both aggregating and non-aggregating conditions.

MSD profiles are shown in Figure 3.1a and e. In 2mM calcium chloride, PS-COOH, PS(COOH)-PEG, and PS(NH_2)-PEG all had diffusion coefficients of similar magnitude at τ=1s (0.10, 0.11, 0.036 μm2/s, respectively), while PS-NH_2 nanoparticles were immobilized (3.8 x 10^{-4} μm2/s). When comparing PS(COOH)-PEG nanoparticles to PS(NH_2)-PEG nanoparticles, it was observed that PS(NH_2)-PEG nanoparticles exhibited an average diffusion coefficient ~2x lower than that of PS(COOH)-PEG nanoparticles. Given the large differences in behavior between the two base particles (PS-COOH and PS-NH_2), this is likely due to charge interactions. In order to investigate the role of calcium on nanoparticle diffusive behavior, we performed similar studies in 0.4% agarose gels constituted with 3mM calcium chloride. In this experiment, PS(COOH)-PEG and PS(NH_2)-PEG MSD profiles remained largely unmodified (0.11 and 0.15 μm2/s for PS-(COOH)-PEG in 2mM and 3mM calcium chloride, respectively, and 0.036 and 0.049 μm2/s for PS(NH_2)-PEG in 2mM and 3mM calcium chloride, respectively). UnPEGylated PS-NH_2 nanoparticles remained immobilized (3.8 x 10^{-4} and 7.7 x $10^{-}4$ μm2/s in 2mM and 3mM calcium chloride, respectively), while PS-COOH nanoparticles lost their diffusive ability and were also immobilized (0.10 and 2.7 x 10^{-4} μm2/s in 2mM and 3mM calcium chloride, respectively). This reproduces previous results demonstrating the effect of calcium on PS-COOH colloidal stability and, in turn, diffusive behavior.

To demonstrate that differences between these populations can be distinguished using geometric trajectory features and a neural network, we performed a PCA analysis on a composite dataset composed of individual trajectory features and locally averaged features. The PCA analysis using the 2mM CaCl2 dataset yielded 12 primary components to achieve 81.8% variance. Average component scores and component distributions are shown in Figure 3.1f and h.

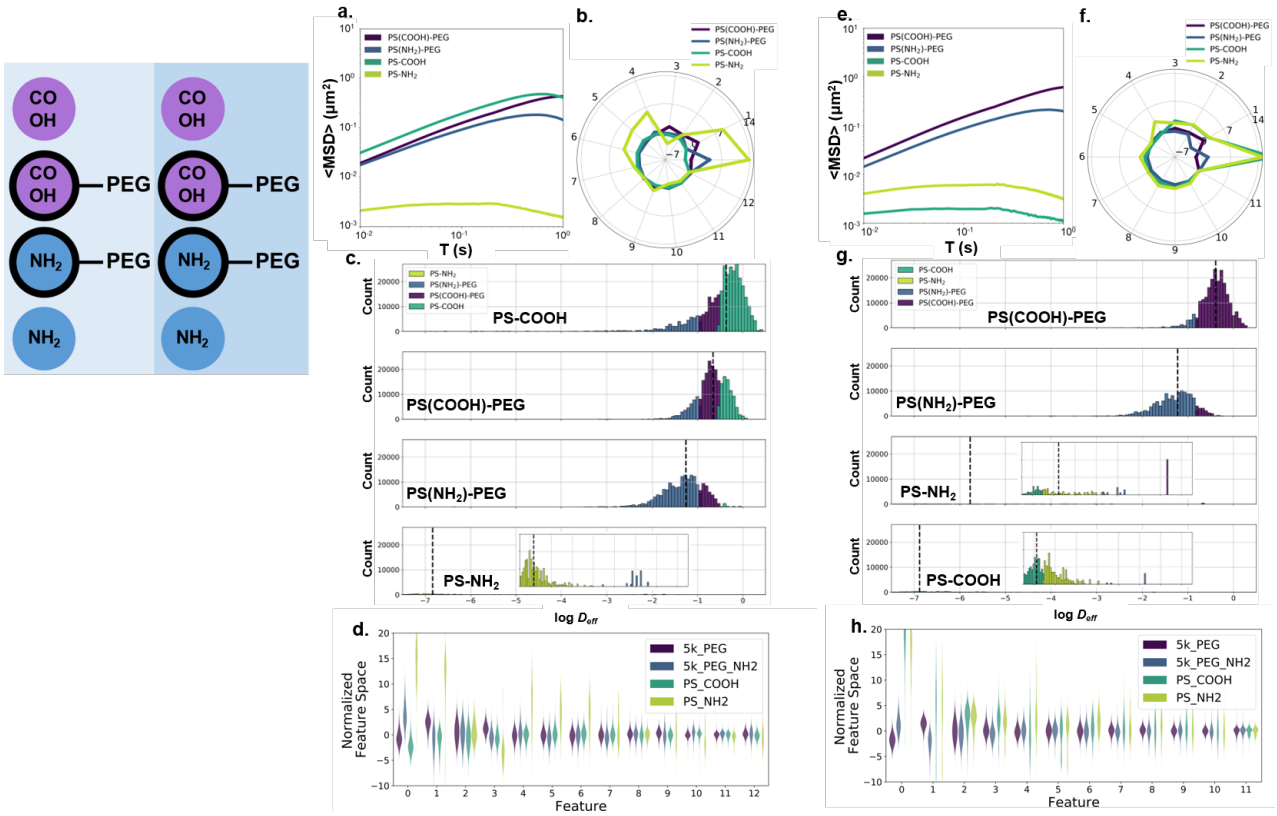

Figure 3.1: Surface functionality-dependent diffusion analysis for nanoparticles in agarose gels constituted with (a.-d.) ACSF (2mM CaCl2) and (e.-h.) ACSF (3mM CaCl2). (a., e.) Geometric ensemble-averaged precision-weighted MSD profiles of 100nm PS-NH_2(yellow-green), PS-COOH (teal), PS(NH_2)-PEG (blue), and PS(COOH)-PEG (purple) NPs in 0.4% agarose gel constituted with (a.) ACSF with 2mM CaCl2 and (b.) ACSF with 3mM CaCl2 (n=2 wells, 5 videos per well). (b., f.) Average component profile of PCA analysis stratified by surface functionality. (c., g.) log mean Deff distributions in the test dataset stratified by surface functionality binned by predicted surface functionality via median log mean Deff predictor. (d., h.) Principle component distributions of PCA analysis stratified by surface functionality.

Table 3.2: Classification metrics for particles of varying surface functionality in agarose gels constituted with ACSF (2mM $CaCl_2$)

	Sample Size		Log Median Predictor		Neural Network Predictor	
	Training	Test	Training	Test	Training	Test
PS-COOH	352129	352051	0.62	0.63	1	0.98
PS(COOH)-PEG	246757	249701	0.47	0.49	1	0.96
PS(NH_2)-PEG	189917	191174	0.81	0.78	1	0.94
PS-NH_2	5761	6010	0.83	0.78	1	0.94
Average/Total	794564	798945	0.68	0.67	1	0.95

Table 3.3: Classification metrics for particles of varying surface functionality in agarose gels constituted with ACSF (3mM $CaCl_2$)

	Sample Size		Log Median Predictor		Neural Network Predictor	
	Training	Test	Training	Test	Training	Test
PS-COOH	9225	9384	0.60	0.59	0.95	0.86
PS(COOH)-PEG	219202	218205	0.91	0.91	1.00	0.97
PS(NH_2)-PEG	135944	138066	0.88	0.89	1.00	0.96
PS-NH_2	2068	2536	0.38	0.30	0.72	0.36
Average/Total	366439	368191	0.69	0.67	0.92	0.79

Using all 51 components as inputs, we built a neural network classifier that was able to predict particle type in the test dataset of the 2mM dataset with a 0.95 average recall score (Table 3.2). Our neural network classifier outperformed a simple predictor based on binning by median log mean diffusion coefficients at τ=1s, which achieved a recall score of 0.67 in the test dataset. The log median predictor suffers because of the significant overlap in log diffusion coefficient distributions (Figure 3.1c), but the inclusion of additional geometric and tracking parameters in a neural network classifier can better resolve the differences

between particle populations. Similar improvements are seen when predicting particle type in the 3mM calcium chloride dataset. Our neural network predictor achieved a 0.79 average recall score in the test dataset (Table 3.3) compared to an average recall score of 0.67 using the log median diffusion coefficient predictor. Similar neural network classifiers could be used to distinguish between heterogeneous particle populations used in cocktail drug delivery platforms.

3.2.2 Diffusion studies: PEG grafting density

Next, we chose to investigate the effect of PEG grafting density on the ability of a nanoparticle to diffuse in a gel model of the brain. The previous surface functionality study demonstrated the order of magnitude difference in diffusion coefficients of PS-COOH and PS(COOH)-PEG nanoparticles. We next wanted to investigate the effect of PEG as a continuous variable on diffusion coefficients by varying the PEG grafting density on the particle surface. Previous studies have examined the effect of PEG grafting density on a variety of upstream outputs (particle properties, protein adsorption) [167, 168] and downstream outputs (macrophage association, biodistribution, pharmacokinetics, clearance) [161, 164, 169]. We hypothesized that nanoparticle diffusion coefficients in the gel model of the brain would increase with PEG grafting density, and that individual trajectories would be distinguishable using machine learning methods.

In this experiment, we varied PEG grafting density by controlling the concentration of the limiting reagent, PEG-NH_2 in the carboxyl-amine reaction used to PEGylate PS-COOH nanoparticles. We varied PEG-NH_2 in 0.1, 0.2, 0.4, 0.5, 0.6, 0.75 and 1.0x the amount calculated for a complete reaction, including PS-COOH nanoparticles as a control. We characterized each PEGylated nanoparticle formulation using mean hydrodynamic diameters, ζ potentials, and PEG surface densities as shown in Table 3.1. All PEGylated particles had near-neutral ζ-potentials ($|\zeta|$<10mV). PEG surface densities exhibit an upward trend with respect to excess PEG as predicted.

As there is little difference between diffusion coefficients of PS-PEG and PS-COOH nanoparticles in ACSF with 2mM calcium chloride [21], we chose to perform diffusion experiments in ACSF with 3mM calcium chloride to maximize the spread in the diffusive behavior between nanoparticle types. The geometric ensemble-averaged MSD profiles of each particle type are shown in Figure 3.2c. As expected,

there is a general trend of increasing diffusion coefficients with increasing PEG surface grafting density (6.0×10^{-3}, 2.9×10^{-2}, 9.9×10^{-3}, 0.32, 0.32, 0.42, 0.82, and 0.10 μm2/s for PS-COOH nanoparticles and PS-PEG nanoparticles with 0.1, 0.2, 0.4, 0.5, 0.6, 0.75, and 1.0x PEG, respectively). While there is some variation in MSD profiles above surface coverage levels of 0.4, they are of similar magnitude. Of interest, there seems to be a dip in the diffusion coefficients of PEG particles with 1.0x PEG. PEG grafting density exhibits threshold behavior in which increasing the number of PEG molecules on the surface no longer improves diffusive behavior.

Table 3.4: Classification metrics for particles of varying PEG grafting density in agarose gels constituted with ACSF (3mM CaCl2)

	Sample Size		Log Median Predictor		Neural Network Predictor	
	Training	Test	Training	Test	Training	Test
PS-COOH	59071	60428	0.61	0.60	0.91	0.70
PS-PEG(0.1x)	50937	50558	0.26	0.25	0.72	0.52
PS-PEG(0.2x)	39916	41699	0.19	0.18	0.71	0.46
PS-PEG(0.4x)	82684	82787	0.15	0.14	0.56	0.27
PS-PEG(0.5x)	61901	62461	0.05	0.04	0.47	0.24
PS-PEG(0.6x)	104356	104215	0.09	0.10	0.59	0.26
PS-PEG(0.75x)	152656	150696	0.57	0.56	0.89	0.67
PS-PEG(1x)	93949	94043	0.31	0.31	0.74	0.50
Average/Total	645470	646887	0.28	0.27	0.70	0.45

We performed a PCA analysis on the composite dataset composed of individual trajectory features and locally averaged features. The PCA analysis yielded 16 primary components achieving 83.2% variance. Average component scores and component distributions are shown in Figure S1a-c. Using the primary components as inputs, we built a neural network classifier that was able to predict PEG surface coverage with an average recall score of 0.45 in the test dataset (Table 3.4). Our neural network classifier outperforms a predictor based on binning by median log diffusion coefficients (an average recall score of 0.27). The neural network suffers most at predicting intermediate surface grafting densities due to the varying

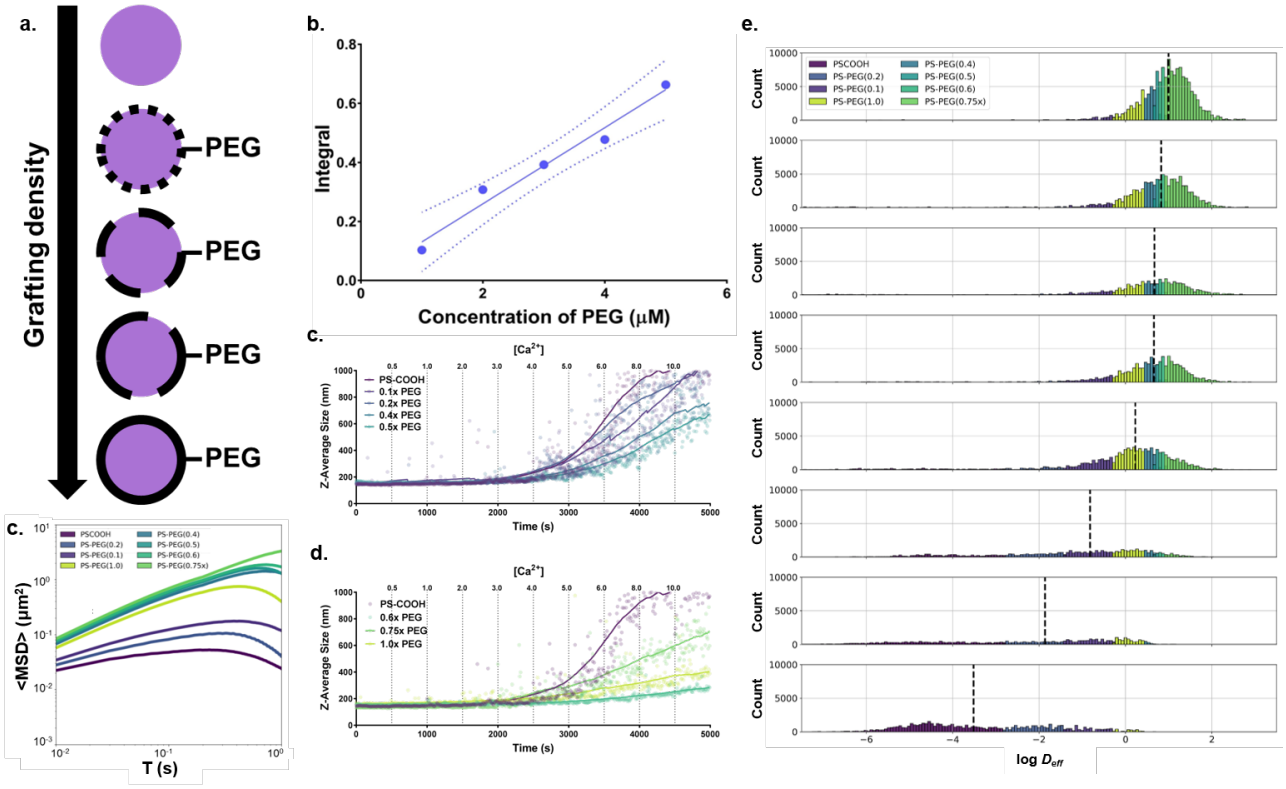

Figure 3.2: PEG grafting density-dependent diffusion analysis for nanoparticles in agarose gels constituted with ACSF (3mM CaCl2). (a.) Representation of nanoparticles with increasing PEG grafting densities. (b.) NMR calibration curve for PEG concentrations (n=3 samples per concentration). Dashed line represents 95% confidence intervals. (c.) Geometric ensemble-averaged precision-weighted MSD profiles of PS-COOH (dark purple), PS-PEG(0.1x) (light purple), PS-PEG(0.2x) (blue-violet), PS-PEG(0.4x) (blue-green), PS-PEG(0.5x) (teal), PS-PEG (0.6x) (seafoam green), PS-PEG(0.75x) (light green), and PS-PEG(1x) (yellow-green) NPs in 0.4% agarose gel constituted with ACSF with 3mM CaCl2 (n=2 wells, 5 videos per well). (d., e.) DLS hydrodynamic diameter aggregation profiles of NPs of varying PEG grafting densities with step-wise increases in CaCl2 concentrations (n=1 per condition). (f.) log mean Deff distributions in the test dataset stratified by PEG grafting density binned by predicted PEG grafting density via median log mean Deff predictor.

intensities of trajectory features. The neural network particularly struggles distinguishing between 0.5, and 0.6x PEG nanoparticles, which have overlapping diffusion coefficient distributions (recall scores of 0.24 and 0.26).

Taking into account these results, we increased the predictive ability of our neural network by binning all particles with excess PEG levels greater than 0.4 together into a high-PEG coverage group. Using this threshold binning configuration, we were able to achieve an average recall score of 0.65 (Table 3.5). Our threshold binning configuration outperformed a binned log median predictor, which achieved an average recall score of 0.48. These results demonstrate that differences in PEG grafting densities can be resolved using MPT tracking and a trained neural network.

Table 3.5: Classification metrics using alternate binning for particles of varying PEG grafting density in agarose gels constituted with ACSF (3mM CaCl2)

	Sample Size		Log Median Predictor		Neural Network Predictor	
	Training	Test	Training	Test	Training	Test
PS-COOH	59071	60428	0.61	0.60	0.93	0.65
PS-PEG(0.1x)	50937	50558	0.34	0.32	0.83	0.49
PS-PEG(0.2x)	39916	41699	0.19	0.18	0.81	0.47
PS-PEG(HI)	495546	494202	0.87	0.80	1.00	0.98
Average/Total	645470	646887	0.50	0.48	0.89	0.65

3.2.3 Diffusion studies: PEG chain length

Next, we wanted to examine the effect of PEG chain length on the ability of a nanoparticle to diffuse in an agarose gel model of the brain. Similar to PEG grafting density, PEG chain length is a continuous variable, but we can exercise more direct control over it, as PEG-NH_2 molecules with highly controlled molecular weights are commercially available. We chose three PEG molecular weights to examine: 1k, 5k, and 10k. PEG chain length has been shown to influence nanoparticle properties including colloidal

stability [170] and protein corona development [162, 170, 171], as well as effects on drug delivery including biodistribution profiles [172, 173], bioactivity [174], cell uptake mechanisms [162], cell proliferation, oral absorption [175], and first pass extraction [176]. We sought to determine the effect of PEG molecular weight on nanoparticle diffusion in a gel model of the brain and whether PEG molecular weight could be distinguished from multiple particle tracking datasets.

We were unsure how PEG chain length would impact diffusion coefficients in a gel model of the brain. The factors we assumed important were ζ potential (near-neutral ζ potentials reduce interactions with charged surfaces and prevent aggregation. PS-PEG nanoparticles synthesized with 1k, 5k, and 10k PEG had ζ-potentials of 1.1 ± 0.1, -2.0 ± 0.3, and -2.3 ± 0.4 mV, respectively), particle size (very large PEG molecules could increase overall particle size thus reducing diffusion coefficients as predicted by Stokes-Einstein. PS-PEG nanoparticles synthesized with 1k, 5k, and 10k PEG had hydrodynamic diameters of 114.8 ± 1.5, 124.2 ± 3.3, and 139.7 ± 3.4 nm, respectively), and tangling effects (long PEG ligands could become entangled with gel components) [177]. Similar to the experiments analyzing varied surface functionalities, we performed experiments in two calcium chloride concentrations (2mM and 3mM).

The geometric ensemble-averaged MSD profiles of each particle type are shown in Figures 3.3c-d. In ACSF with 2mM calcium chloride, there is little difference in MSD profiles for all four particle types (diffusion coefficients of 0.15, 0.11, 0.10, 0.10 μm2/s for PS-PEG(10k), PS-PEG(5k), PS-PEG(1k), and PS-COOH nanoparticles, respectively). PEG chain length exhibits some improvements in particle diffusive ability, with ~50% higher diffusion coefficients when comparing PS-PEG(10k) nanoparticles with PS-COOH nanoparticles. This increase doesn't occur linearly with PEG chain length. When calcium concentration in increased, PS-COOH nanoparticles lose their diffusive behavior, while particle behavior does not vary for PS-PEG(1k), PS-PEG(5k), and PS-PEG(10k) (diffusion coefficients of 0.22, 0.15, 0.15, and 2.7 x 10^{-4} μm2/s for PS-PEG(10k), PS-PEG(5k), PS-PEG(1k), and PS-COOH nanoparticles, respectively). We were unsure whether a neural network would successfully be able to distinguish between particles that had such similar MSD profiles. Were there other geometric features that could potentially be used to distinguish between particle populations? We performed a PCA analysis on the composite dataset composed of individual trajectory features and locally averaged features. The PCA analysis yielded 12 primary com-

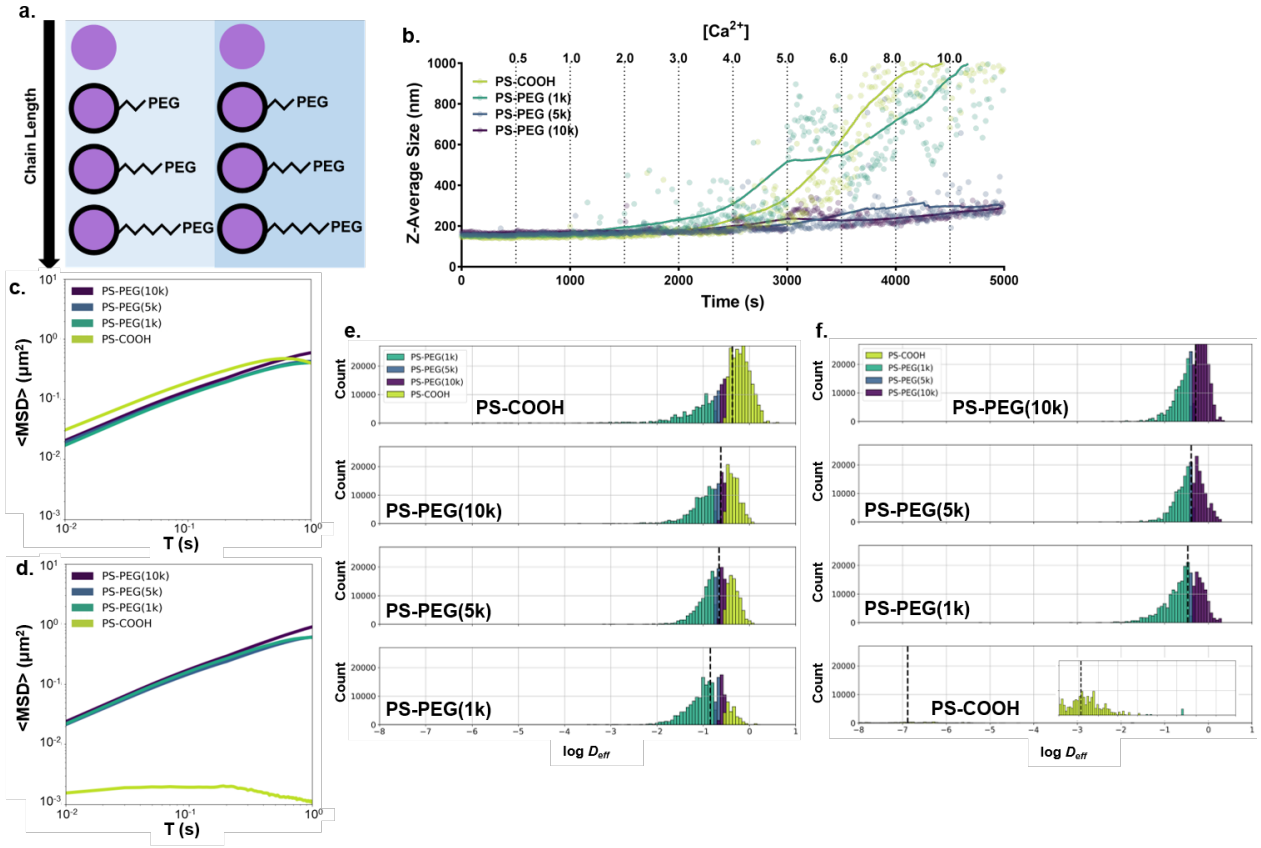

Figure 3.3: PEG chain length-dependent diffusion analysis for nanoparticles in agarose gels constituted with (c., e.) ACSF (2mM CaCl2) and (d., f.) ACSF (3mM CaCl2). (a.) Representation of nanoparticles with increasing PEG chain lengths in ACSF (2mM CaCl2) and ACSF (3mM CaCl2). (b.) DLS hydrodynamic diameter aggregation profiles of NPs of varying PEG chain lengths with step-wise increases in CaCl2 concentrations (n=1 per condition). (c., d.) Geometric ensemble-averaged precision-weighted MSD profiles of PS-COOH (yellow-green), PS-PEG(1k) (teal), PS-PEG(5k) (blue), and PS-PEG(10k) (purple) NPs in 0.4% agarose gel constituted with (c.) ACSF with 2mM CaCl2 and (d.) ACSF with 3mM CaCl2 (n=2 wells, 5 videos per well). (e., f.) log mean Deff distributions in the test dataset stratified by PEG chain length binned by predicted chain length via median log mean Deff predictor.

ponents achieving 80.9% variance. Average component scores and component distributions are shown in Figure S2a-d.

Using all 51 inputs, we built a neural network classifier that was able to predict PEG chain length in the 2mM calcium chloride dataset with an average recall score of 0.68 in the test dataset (Table 3.6). This compares favorably with a predictor based on the log median diffusion coefficients, which achieved an average recall score of 0.38. Because the diffusion coefficient distributions have significant overlap (Figure 3.3e), the only particle populations that could be distinguished with accuracy were those with the lowest and highest median diffusion coefficients in the training dataset (PS-PEG(1k) and PS-COOH, respectively) when using the median log predictor. The median log mean diffusion coefficient predictor performed better in the 3mM calcium chloride dataset (average recall score of 0.54 in the test dataset, Table 3.7) because the PS-COOH nanoparticles were immobilized, but the three overlapping PS-PEG diffusion coefficient distributions made PS-PEG(5k) nanoparticles difficult to resolve (recall score of 0.12 in the test dataset). The neural network was better able to resolve the PS-PEG nanoparticles achieving an average recall score of 0.76 in the test dataset. Despite having ensemble MSD profiles of similar magnitude, the differences between trajectory features made them distinguishable with a neural network.

Table 3.6: Classification metrics for particles of varying PEG chain length in agarose gels constituted with ACSF (2mM $CaCl_2$)

	Sample Size		Log Median Predictor		Neural Network Predictor	
	Training	Test	Training	Test	Training	Test
PS-COOH	352129	352051	0.62	0.63	1	0.98
PS-PEG(1k)	211851	249701	0.62	0.61	1	0.52
PS-PEG(5k)	246757	191174	0.13	0.14	1	0.57
PS-PEG(10k)	244724	352051	0.14	0.14	1	0.66
Average/Total	1055461	1144977	0.38	0.38	1	0.68

Table 3.7: Classification metrics for particles of varying PEG chain length in agarose gels constituted with ACSF (3mM CaCl2)

	Sample Size		Log Median Predictor		Neural Network Predictor	
	Training	Test	Training	Test	Training	Test
PS-COOH	9225	9384	0.89	0.91	1	0.98
PS-PEG(1k)	257612	255187	0.55	0.56	1	0.83
PS-PEG(5k)	219202	218205	0.10	0.12	1	0.69
PS-PEG(10k)	326581	328394	0.54	0.57	1	0.80
Average/Total	812620	811170	0.52	0.54	1	0.76

3.2.4 Diffusion studies: PEG chain length in tissue

In order to verify whether trends and predictive ability observed with PEGylated particles of varying chain lengths carried over in the brain, we performed similar experiences varying PEG chain length in *ex vivo* rat brain slices. The geometric ensemble-averaged MSD profiles of each particle type are shown in Figure 4b. As expected in previous studies, PS-COOH particles were immobile in tissue while PS-PEG particles, regardless of PEG chain length, retained diffusive ability. At short lag times, (up to τ=100ms) PS-PEG(1k), PS-PEG(5k), and PS-PEG(10k) had diffusion coefficients of similar magnitudes. But at longer lag times, the diffusion coefficients of PS-PEG(5k) nanoparticles lagged behind their PS-PEG(1k) and PS-PEG(10k) counterparts. This behavior seems to be due to a single slice with high particle counts of immobilized particles and is likely due more to slice variability than any inherent differences in particle behavior. Similar to previous experiments, we performed a PCA analysis on the composite dataset composed of individual trajectory features and locally averaged features. The PCA analysis yielded 11 primary components achieving 80.7% variance. Average component scores and component distributions are shown in Figure S2. Using all 51 inputs, we built a neural network classifier with identical parameters to the previous studies. In order to account for slice-to-slice variability, we performed an alternate train-test split structure using a leave-one-out (LOO) strategy. The neural network was trained using trajectory datasets from five

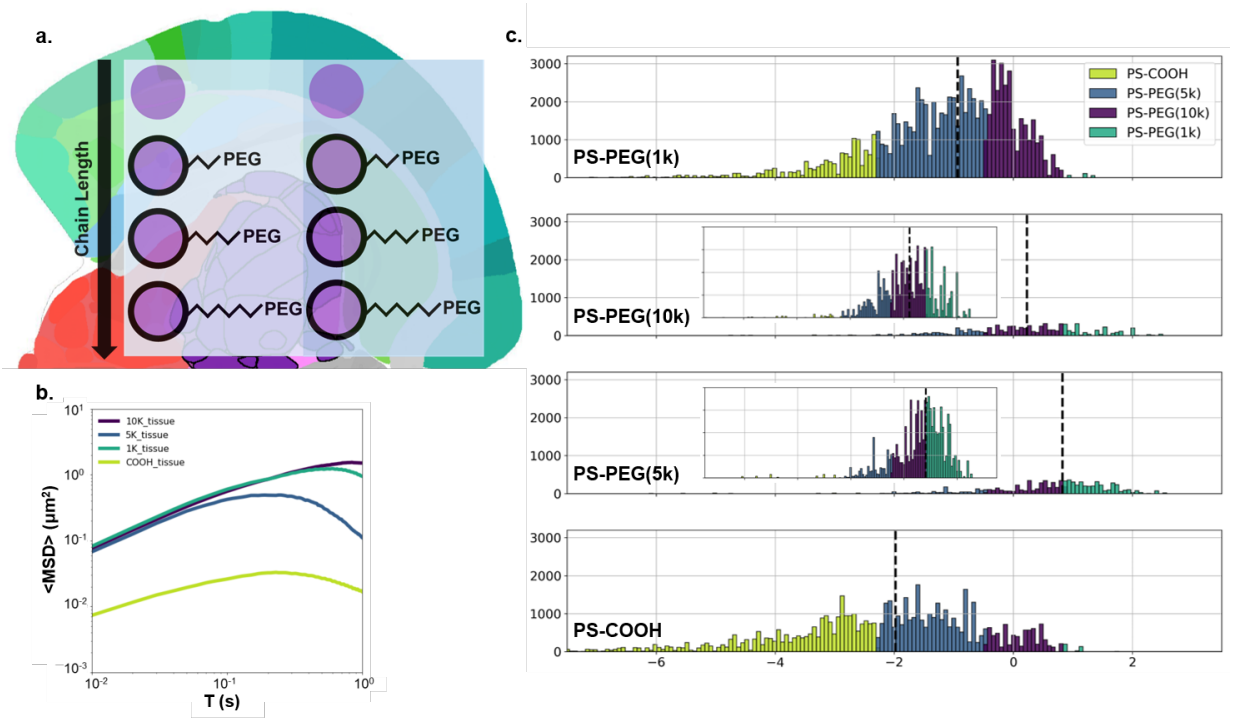

Figure 3.4: PEG chain length-dependent diffusion analysis for nanoparticles in an organotypic brain slice model. (a.) Representation of nanoparticles with increasing PEG chain lengths in a brain slice. (b.) Geometric ensemble-averaged precision-weighted MSD profiles of PS-COOH (yellow-green), PS-PEG(1k) (teal), PS-PEG(5k) (blue), and PS-PEG(10k) (purple) NPs (n=6 slices per condition, 5 videos per slice). (c.) log mean Deff distributions in the test dataset stratified by PEG chain length binned by predicted chain length via median log mean Deff predictor.

of the six slices, reserving the final slice as a test dataset. This was repeated six times for each slice and the average recall values were reported. Our neural network was able to predict PEG chain length with an average recall score of 0.55 in the test dataset (Table 3.8, scores of individual predictors shown in Tables C.1, C.2, C.3). The amount of inter-slice variability greatly hinders the strength of any potential predictor. The predictor particularly suffered when seeking to differentiate PS-PEG(5k) nanoparticles (recall score of 0.22), which couldn't be well differentiated from PS-PEG(1k) or PS-PEG (10k) nanoparticles. While our predictor outperforms a binned log median predictor trained using a similar LOO strategy (average recall score of 0.32), it is difficult to compensate for the amount of variability between samples. Any differences attributable to PEG chain molecular weight aren't as large as differences attributable to slice variability. There is some potential in improving the predictive power by increasing the number of slices used in the study, but the slice variability/PEG chain length variability ratio is still high and will still limit predictive ability. Some variability is likely due to varying damage during slice preparation and can be improved. When the amount of slice-to-slice variation exceeds the variation to behavior due to the variable of interest (e.g. PEG chain length), predictive ability will be severely limited.

Table 3.8: Classification metrics for particles of varying PEG chain length in organotypic brain slice model

	Sample Size		Log Median Predictor (Avg. LOO)		Neural Network Predictor (Avg. LOO)	
	Training	Test	Training	Test	Training	Test
PS-COOH	74862	14972	0.63	0.57	0.92	0.59
PS-PEG(1k)	180450	36090	0.25	0.20	0.95	0.70
PS-PEG(5k)	119583	23917	0.32	0.09	0.83	0.22
PS-PEG(10k)	61613	12323	0.42	0.41	0.85	0.71
Average/Total	436507	87301	0.41	0.32	0.89	0.55

3.3 Conclusions

We are able to predict nuanced properties of nanoparticle formulations based purely on MPT datasets in *in vitro* environments using neural networks. These include surface charge, PEG grafting density, and PEG chain length. This has potential impact in the use of nanoparticles as biological probes. If nuanced aspects of nanoparticles and their surrounding environment can be differentiated solely based on their trajectory features, nanoparticle transport properties can be used as a surrogate measure of biological events. Furthermore, subpopulations of nanoparticles can potentially be distinguished from each other in dynamic processes without needing any complex labelling protocols.

4

Methods

4.1 Nanoparticle preparation and characterization via dynamic light scattering

4.1.1 Nanoparticle preparation

Fluorescent carboxylate (COOH)-modified polystyrene latex (PS) nanoparticles (PS-COOH) (Fisher Scientific, Hampton, NH) were covalently modified with methoxy (MeO)-poly(ethylene glycol) (PEG)-amine (NH_2) (5kDa MW, Creative PEG Works, Winston-Salem, NC) by carboxyl amine reaction (18).

Briefly, 50-100 μL of PS-COOH particle suspension was washed and resuspended to 2- to 6- fold dilution in ultrapure water. An excess of MeO-PEG-NH2 was added to the particle suspension and mixed to dissolve the PEG. N-Hydroxysulfosuccinimide (MilliporeSigma, Burlington, MA) was added to a final concentration of 7 mM and 200 mM borate buffer, pH 8.2, was added to a 4-fold dilution of the starting volume. 1-Ethyl-3-(3-dimethylaminopropyl) carbodiimide (EDC, Invitrogen, Carlsbad, CA) was added to stoichiometrically complement the added MeO-PEG-NH2. Particle suspensions were placed on a rotary incubator for 4 h at 25°C and then washed via centrifugation (Amicon Ultra 0.5 mL 100k MWCO; MilliporeSigma) at conditions specified previously [11]. Particles were resuspended in ultrapure water to the initial particle volume and stored at 4°C until use.

100-nm fluorescent NH2-modified PS nanoparticles (Fisher Scientific) were covalently modified with methoxy (MeO)-PEG-carboxyl (COOH) (5kDa MW, Creative PEG Works) by carboxyl amine reaction using a similar method as described above.

4.1.2 Nanoparticle characterization

The hydrodynamic diameter, polydispersity index (PDI), and ζ-potential were measured for COOH- and PEG-coated fluorescent nanoparticles via dynamic light scattering (DLS) (NanoSizer Zeta Series, Malvern Instruments, Malvern, UK, n=3 measurements per sample). Particles were diluted to ~0.002% solids in filtered (0.45 μm, Whatman, Maidstone, UK) 10 mM NaCl and incubated for 24 h prior to measurement.

4.1.3 Media preparation

Artificial cerebrospinal fluid (ACSF) was prepared with the addition of the following concentrations of reagents to deionized (DI) water: 119 mM NaCl (MilliporeSigma), 26.2 mM NaHCO3 (MilliporeSigma), 2.5 mM KCl (MilliporeSigma), 1 mM NaH2PO4 (MilliporeSigma), 1.3 mM $MgCl_2$ (MilliporeSigma), and 10 mM glucose (MilliporeSigma). The solution was filtered (0.45μm) in a sterile environment and stored at 4°C. For individual experiments, aliquots of ACSF were taken and $CaCl_2$ added, then the media

was allowed to equilibrate at desired conditions (23°C/37°C and 5%CO_2) for 1 hour and adjusted to the appropriate pH (5.5, 7.2, or 8.5) with 0.2 mM HCl or 1 N NaOH.

4.1.4 In vitro particle aggregation via dynamic light scattering

Stock 1 M $CaCl_2$ and $MgCl_2$ solutions were prepared in DI water, from which 0.5, 1.0, 2.0, 4.0, 5.0, 8.0, and 10.0 mM dilutions were made. PS-COOH and PS-PEG nanoparticles were diluted in these salt solutions to achieve a concentration of 0.002%solids. Nanoparticle suspensions were allowed to sit for 24 hours before measuring their hydrodynamic diameters via dynamic light scattering (DLS) (NanoSizer Zeta Series, Malvern Instruments, Malvern, UK). Number means were reported for static studies as recommended by EU directive 2011/696/EU [93]. Z-average diameters were reported for aggregation studies. While z-average values can be inaccurate for polydisperse samples, these measurements are less vulnerable to noise, and some inaccuracy is inevitable in high time resolution measurements via DLS.

4.1.5 Aggregation kinetics via dynamic light scattering

Particle-free media was allowed to reach temperature (23°C or 37°C) in the Zetasizer followed by a three-minute equilibration period. Nanoparticles were quickly added and mixed to achieve a concentration of 0.002%solids, and hydrodynamic diameter measurements were then taken every 10 seconds for 50 measurements (total time: 8 minutes 20 seconds). The measurements were paused briefly in order to add enough 1 M $CaCl_2$ solution to achieve 0.5 mM $CaCl_2$, and another 50 measurements in 10-second intervals were taken. This process was repeated for successive $CaCl_2$ concentrations of 1, 2, 3, 4, 5, 6, 8, and 10 mM.

For pH measurements, ACSF without $CaCl_2$ was prepared as described above. Aliquots of ACSF were allowed to equilibrate at the desired conditions (23°C and 5%CO_2) for 1 h and adjusted to pH 7.2, and $CaCl_2$ was added to achieve 3 mM concentration. Nanoparticles were added and mixed to achieve a concentration of 0.002%solids. Potentiometric titrations were performed to assess pH as a function of acid/base added (see Figure A.1). Starting at pH 7.2, 0.2 M HCl or 1 N NaOH was added in 1 to 40 μL increments

and the pH read until the pH reached either 3 or 11.

For kinetic studies as a function of pH, aliquots of ACSF were allowed to equilibrate at the desired conditions (23°C and 5%CO2) for 1 h and adjusted to pH 7.2, and $CaCl_2$ was added to achieve 3 mM concentration. Hydrodynamic diameters measurements were taken every 10 seconds for 50 measurements. The measurements were paused briefly in order to add enough acid to reach the nearest 0.5 pH unit neighbor (7.0 or 7.5) as calculated from the potentiometric curve above, and another 50 measurements in 10-second intervals were taken. Measurements were paused, acid/base added, and restarted at successive pHs (7.0, 6.5, 6.0, 5.5, 5.0, 4.5, 4.0, 3.5, and 3.0 for acid; 8.0, 8.5, 9.0, 9.5, 10.0, 10.5, and 11.0 for base).

4.1.6 Protein corona assay

Protein adhesion of serum-incubated nanoparticles was determined via bicinchoninic acid (BCA) assay (ThermoFisher). Briefly, nanoparticle suspensions of each particle preparation were spun down at 100,000 g. The supernatant was discarded, and the particle pellet was resuspended in 10mM NaCl. BCA working reagent was prepared by mixing 50 parts Reagent A (sodium carbonate, sodium bicarbonate, BCA, sodium tartrate, 0.1M sodium hydroxide) with 1-part Reagent B (4% cupric sulfate). In a 96-well plate, 25μL of each nanoparticle sample was mixed with 200μL of the working reagent. The cover plate was incubated at 37°C for 30 min, and UV-Vis measurements were taken at 562 nm. In order to account for nanoparticle fluorescence, serum-incubated UV-Vis measurements were normalized to UV-Vis measurements of serum-free nanoparticles at the same concentration. Measurements were quantified using a 5-point bovine-serum albumin (BSA) calibration curve with concentrations between 5 and 250 μg/mL.

4.1.7 PEG surface coverage NMR quantification

A calibration curve was prepared using H1 NMR (Bruker AV-300) for concentrations of PEG in a lock solvent within the range of 1 and 5μL. Samples were prepared in CDCL3 (Aldrich) with 0.5% by weight 1,4-bistrimethylsilane (Aldrich) as an internal standard. The integral of the PEG peak at a shift of 2.6ppm

was measured using Bruker Topspin 4.0.02 and plotted against the concentration of PEG in solution. Samples of different particle-types were then prepared using the same internal standard. Particles were lyophilized and weighed prior to being suspended in the lock solvent. Using the relationship between integral and concentration derived from the calibration curve, the concentration of PEG in the solution of dilute particles was calculated for each particle type.

The PEG surface density, [Γ], was calculated by dividing the mass of PEG on the nanoparticles by their surface area. This value represents the number of PEG molecules per 100nm2 on the nanoparticle surface.

$$[\Gamma] = \frac{\mathcal{M}_{PEG} \times 6.02 \times 10^{23}}{(W_{NP} \div \varrho_{NP}) \div \left(\frac{4}{3}\pi\left(\frac{D}{2}\right)^{3}\right)} \div 4\pi\left(\frac{D}{2}\right)^{2}$$

where D is the diameter of the particle as determined by dynamic light scattering, ϱ_{NP} is the nanoparticle density, W_{NP} is the total mass of nanoparticles after lyophilization and $\mathcal{M}_{PEG}$ is the total moles of PEG measured via H^1 NMR [178]. The nanoparticle density, ϱ_{NP}, is assumed to be equal to the density of the polymer, 1.04 g/mL for polystyrene.

4.2 Additional characterization techniques

4.2.1 Rheological characterization of agarose gels

A rheometer (Physica MCR 301, Anton Paar, Graz, Austria) operating in oscillatory mode was used to characterize the mechanical properties of the different weight percent agarose gels (0.4, 0.6, 0.8, and 1.0%). A 25 mm parallel plate attachment (Anton Paar) was operated at a 0.5 mm gap for all experiments. Additionally, the base plate was set to 22°C 30 min prior to the experiment and held constant throughout the duration of the experimental window.

The linear viscoelastic region was first determined by performing a strain and frequency sweep on 0.4% agarose following a 4 h incubation at 22°C. For the strain sweep, the frequency was set to 1 Hz, and the

storage and loss moduli were measured at various strains (0.1 – 10%). For the frequency sweep, the strain was set at 2%, and the storage and loss moduli were measured at various frequencies (0.1 – 10 Hz). The sweeps demonstrated that at 2% strain and 2 Hz, 0.4% agarose is in the linear viscoelastic region because slight changes in strain or frequency do not change the measured storage modulus (Figure B.6).

Time sweeps were performed on all concentrations of agarose by monitoring the storage and loss moduli for 4 h upon removal from 99°C stock solution. For 0.4, 0.6, and 0.8% agarose gels, time sweeps were performed at a strain and frequency of 2% and 2 Hz, respectively. For the 1.0% agarose gel, time sweeps were performed at a strain and frequency of 0.5% and 0.5 Hz to remain within the linear viscoelastic region.

4.2.2 FACS cell uptake study

Brain slices were prepared from 30 to 40 g PND14 Sprague-Dawley rat pups. Slices were incubated with either fluorescently labelled 100nm PS-COOH nanoparticles, PS-PEG nanoparticles, PS-COOH nanoparticles incubated in horse serum, or PS-PEG nanoparticles incubated in horse serum at a concentration of approximately 0.014% solids for 2 h. Slices were treated with Accutase (Millipore) for 30 min on ice and homogenized. The tissue suspension was filtered through a tissue strainer and diluted in HBSS + 25 mM HEPES (Fisher Scientific). The suspension was spun down at 600 g at 4°C for 5 min and the supernatant discarded. The cell pellet was resuspended in FBS and mixed with a Percoll solution [30% Percoll (GE Healthcare), 3% 10x PBS, 67% HBSS + 25 mM HEPES]. The Percoll cell suspension was overlayed with 1 mL FACS buffer (45 mL HBSS, 5 mL FBS, 0.5 mL HEPES). The cell suspension was spun down at 800 g at 4°C for 30 min. The supernatant was discarded, and the cell pellet was washed 2x with FACS buffer.

The cells were stained with DAPI (Molecular Probes), FITC CD11b (BioLegend), and the CD11b isotype PE Cy7 CD45 (BioLegend). Flow cytometry analysis was performed on the LSR II instrument (BD Biosciences). Laser lines and optical emission filters were arranged as follows: DAPI: 355 nM 20 mW UV laser and 450/50 emission detector; FITC: 488 nM 100 mW blue laser and 530/30 emission filter; Texas RED: 561 nM 150 mW yellow-green laser and 610/20 emission detector. Gating was performed using DAPI,

FITC, and particle controls. Each sample measurement included 10,000 events.

4.3 Diffusion studies

4.3.1 Gel diffusion studies

0.4%agarose gels in ACSF ($CaCl_2$ concentrations of 0, 3, 5, and 10 mM, pH 7.2) were prepared by adding 40 mg agarose (low EEO, gel point for 1.5%gel, 36 $\pm$ 1.5°C, MilliporeSigma) to ACSF. The agarose-ACSF mixture was heated to 99°C and mixed well until the agarose was completely dissolved, as indicated by no visible particulates in the solution. 400 μL agarose-ACSF was added to a well in an 8-well imaging plate and PS-COOH or PS-PEG nanoparticles were quickly added and mixed until evenly distributed to achieve a concentration of 0.005%solids. Four samples were prepared per particle type-condition combination. The prepared gels were allowed to set overnight at room temperature. Prior to imaging, the gels were allowed to incubate at 37°C and 5%CO_2 for 30 min.

Five videos were collected per well at 10 Hz and 100x magnification for 6.5 s via fluorescent microscopy using a cMOS camera (Hamamatsu Photonics, Bridgewater, NJ) mounted on a confocal microscope (Nikon Instruments, Melville, NY). Nanoparticle trajectories and trajectory features were calculated via diff_classifier, a self-developed Python package [179]. A complete list of trajectory features, including a brief description and method of calculation, is provided as Supplementary Table B.1.

For polydispersity-dependent studies, gels were prepared using the method described above in ACSF without calcium chloride with either equal weight percent (20%) or equal number percent (20%) samples of 100, 200, 500, 1000, and 2000 nm PS-COOH or PS-PEG NPs. Videos were collected and analyzed using the same parameters described above.

For time-dependent aggregation studies, gels were prepared using the method described above in ACSF with 5mM calcium chloride, but gels were not allowed to set overnight. Gels set for three hours to ensure complete gelation, and videos were collected and analyzed at 0, 1, 4, and 24 hours prior to the three-hour

gelation period.

For agarose concentration-dependent studies, 0.4, 0.6, 0.8, 1.0, and 1.2-percent agarose gels were prepared, corresponding to 40, 60, 80, 100, and 120 mg agarose in 10 mL ACSF, respectively. 100nm PS-COOH nanoparticles were immediately added and mixed until evenly distributed to achieve a concentration of 0.005% solids. Two samples were prepared for each combination of particle size and gel stiffness. The prepared gels were allowed to set overnight at room temperature. Five videos were collected in each well (n=2 per particle type) using the same imaging setup described above.

For serum-treated diffusion studies, 100nm PS-COOH and 100nm PS-PEG nanoparticles were added to separate samples of horse serum (Fisher Scientific) in a 1:100 dilution. Particles were incubated in serum for 24 h at 37°C. In order to ensure similar concentrations of nanoparticles in gels, particles were centrifuged, and the pellet was resuspended in a volume of horse serum equivalent to the original starting volume. Nanoparticle hydrodynamic diameter and zeta potential were measured using methods specified above. The measured hydrodynamic diameter distributions are shown in Figure 2.2b. Serum-treated nanoparticles were loaded into 0.4% agarose gels in ACSF as described previously. MPT videos were collected at 10 Hz and 100x magnification for 6.5 s and trajectories generated via diff_classifier.

For surface functionality-dependent diffusion studies, PS-COOH, PEG-modified PS-COOH nanoparticles (PS(COOH)PEG or PS-PEG), PS-NH_2, or PEG-modified PS-NH_2 (PS(NH_2)-PEG) nanoparticles were added and mixed into 0.4% agarose gels constituted with ACSF with 2mM and 3mM calcium chloride were prepared using a similar method described above. PS-COOH nanoparticles were used as a control. Ten videos were collected in each well (n=2 per particle type) using the same imaging setup described above.

For PEG grafting density-dependent diffusion studies, PS-PEG nanoparticles synthesized with 0.1x, 0.2x, 0.4x, 0.5x, 0.6x, 0.75x, or 1.0x excess PEG were added and mixed into 0.4% agarose gels constituted with ACSF with 3mM calcium chloride were prepared using a similar method described above. PS-COOH nanoparticles were used as a control. Ten videos were collected in each well (n=2 per particle type) using the same imaging setup described above.

For PEG chain length-dependent diffusion studies, PS-PEG(1k), PS-PEG(5k), and PS-PEG(10k) nanopar-

ticles were added and mixed into 0.4% agarose gels constituted with ACSF with 2mM or 3mM calcium chloride using a similar method described above. PS-COOH nanoparticles were used as a control. Five videos were collected in each well (n=2 per particle type) using the same imaging setup described above.

4.3.2 In vitro diffusion study in microglial cell culture

BV-2 immortalized microglial cells (ATCC, CRL-2469) at passage 8 (P8) were cultured from frozen stock at a seeding density of 2 million cells/cm² in T-75 flasks (USA Scientific, Ocala, FL), yielding 70-80% confluency in 7 days. Cell culture media (CCM) consisted of 90% Dulbecco's Modified Eagle Medium (DMEM; ATCC) with 4 mM L-glutamine adjusted to contain 1.5 g/L sodium bicarbonate and 4.5 g/L glucose, 10% fetal bovine serum (FBS; ATCC), and 1% penicillin/streptomycin (Gibco, ThermoFisher). After eight days, the cells were passaged to P9 and subsequently plated into four 35 mm dishes (ATCC) at a seeding density of 700,000 cells/cm2. PS-COOH and PS-PEG nanoparticles were first prepared in filtered (0.45 μm) 10 mM NaCl solution and mixed with CCM. The cells were incubated with the particles for 30 min prior to imaging. During imaging, cells were maintained at 37°C and 5% CO_2 using Heracell TriGas (ThermoFisher) incubation chamber. Five videos per sample were collected using the described acquisition settings above.

4.3.3 Ex vivo diffusion study in organotypic whole hemisphere rat brain slices

All experiments were carried out at the University of Washington in accordance with National Institutes of Health guidelines and local Institutional Animal Care and Use Committee regulations. Brain slices were prepared from 30 to 40 g postnatal day 14 (PND14) Sprague-Dawley rat pups. Briefly, animals were administered an intraperitoneal injection of pentobarbital (150 mg/kg). After euthanasia, animals were decapitated and brains rapidly removed and immersed in cold dissecting media consisting of 500 mL HBSS (Fisher Scientific), 1% Penicillin- Streptomycin (MilliporeSigma), and 3.2 g glucose (Millipore-

Sigma). 300 μm-thick coronal slices (n=2 per rat) were prepared using a McIlwain tissue chopper (Ted Pella, Redding, CA). The tissue chopper and razor blades were washed with 70% ethanol prior to sectioning. Slices were placed in a Petri dish containing dissecting media and separated under a surgical dissection microscope. Individual slices were placed on 30 mm cell culture inserts (Fisher Scientific) in 6-well plates (Eppendorf, Hamburg, Germany), filled with 1.5 mL slice culture media containing 200 mL MEM (Fisher Scientific), 100 mL HBSS, 100 mL horse serum (Fisher Scientific), 4 mL Glutamax (Fisher Scientific), and 1% Penicillin-Streptomycin. Slices were allowed to incubate in sterile conditions at 37°C and 5% CO_2 overnight. 30 min prior to imaging, slices were incubated with nanoparticles at a concentration of approximately 0.014% solids. Slices were imaged in a temperature-controlled incubation chamber maintained at 37°C, 5% CO_2, and 80% humidity. 10 videos were collected in the cortex of each slice, and trajectories were calculated via diff_classifier [179].

For PEG chain length-dependent diffusion studies, 30 minutes prior to imaging, slices were incubated with either 100nm PS-COOH, PS-PEG(1k), PS-PEG(5k), or PS-PEG(10k) nanoparticles at a concentration of approximately 0.014% solids. Slices were imaged in a temperature-controlled incubation chamber maintained at 37°C, 5% CO_2, and 80% humidity. 10 videos were collected in the cortex of each slice and trajectories calculated using methods described above.

4.3.4 Multiple particle tracking analysis and trajectory feature extraction

Nanoparticle trajectories were extracted from microscopy videos via a lab-developed Python package diff_classifier for parallelized and reproducible MPT workflows [179]. The diff_classifier package relies on a headless implementation of an ImageJ plugin TrackMate with tracking parameters selected with a combination of user inputs and regression techniques based on input images [180]. Diff_classifier also performs trajectory feature extraction based on features from the TrajClassifier ImageJ plugin [56] (e.g. α, the anomalous diffusion exponent, and boundedness, which quantifies how much a particle is restricted in a circular confined space). Based on 17 features (Table B.1), an additional set of 34 local average and deviation parameters were calculated for 256 total 9μm x 9μm tiled rectangular regions in each video.

4.3.5 PCA Analysis

A spatial checkerboard train-test split was performed on the geometric feature datasets from each experiment. Every other square (of area 256 x 256 pixels^2 in the checkerboard pattern was assigned to either the training dataset or the test dataset. Principle component analysis (PCA) with feature scaling was carried out on the training dataset of the experimental dataset. The sampling adequacy was found to be appropriate (KMO > 0.8) [181]. Components were extracted to describe >80% of the total variance. The resulting PCA transformation was applied to the test dataset for downstream analysis.

4.3.6 Neural network predictor

In order to evaluate whether trajectories can be used to predict particle properties or parameters of the surrounding tissue microenvironment, neural networks were trained using scikit-learn's Multi-Layer Perceptron Classifier using the trajectory features as inputs. An initial grid search was performed to select the best hyperparameters of the neural network. These hyperparameters included initial learning rate, batch size, and the L2 regularization term, with 10% of the training dataset set aside for cross validation. All models used stochastic gradient descent for weight optimization, the rectified linear unit function for activations in the hidden layer, the log loss cost function, and an adaptive learning rate decreasing the learning rate by a factor of five each time two consecutive epochs fail to decrease training loss by 10^{-4}. All models were trained on on the chekcerboard training datasets described above. For slice studies, additional training and testing iterations was performed with an alternate splitting procedure, isolating data from one slice as a test dataset to test whether the trained neural network models could be extended to experiments outside the original dataset.

5

Paper summaries

Systems-level thinking for nanoparticle-mediated therapeutic delivery to neurological diseases

Curtis C.†, Zhang M.†, Liao R.†, Wood T.†, Nance E.*. Systems-level thinking for nanoparticle-mediated therapeutic delivery to neurological diseases. WIREs Nanomed Nanobiotechnol. (2016).

** *selected cover image*: Curtis C., Zhang M., Liao R., Wood T., and Nance E. Cover Image, Volume 9, Issue 2. *WIREs Nanomed Nanobiotechnol,* (2017) 9:n/a, e1463. doi:10.1002/wnan.1463

Neurological diseases account for 13% of the global burden of disease. As a result, treating these diseases costs $750 billion a year. Nanotechnology, which consists of small (~1-100 nm) but highly tailorable platforms, can provide significant opportunities for improving therapeutic delivery to the brain. Nanoparticles can increase drug solubility, overcome the blood-brain and brain penetration barriers, and provide timed release of a drug at a site of interest. Many researchers have successfully used nanotechnology to overcome individual barriers to therapeutic delivery to the brain, yet no platform has translated into a standard of care for any neurological disease. The challenge in translating nanotechnology platforms into clinical use for patients with neurological disease necessitates a new approach to: (1) collect information from the fields associated with understanding and treating brain diseases and (2) apply that information using scalable technologies in a clinically-relevant way. This approach requires systems-level thinking to integrate an understanding of biological barriers to therapeutic intervention in the brain with the engineering of nanoparticle material properties to overcome those barriers. To demonstrate how a systems perspective can tackle the challenge of treating neurological diseases using nanotechnology, this review will first present physiological barriers to drug delivery in the brain and common neurological disease hallmarks that influence these barriers. We will then analyze the design of nanotechnology platforms in preclinical in vivo efficacy studies for treatment of neurological disease, and map concepts for the interaction of nanoparticle physicochemical properties and pathophysiological hallmarks in the brain.

Exploring the interface of trajectory datasets and machine learning in the biomedical and life sciences

Curtis C., Shackelford, D., Nance, E. Exploring the interface of trajectory datasets and machine learning in the biomedical and life sciences. *In preparation*

Researchers in biomedical and life sciences fields are increasingly turning to multiple particle tracking (MPT) as a method of data collection. Despite the application of MPT to a variety of problems in biomedical fields, most papers share a common formula: MPT is used to quantify some magnitude of

transport (e.g. diffusion coefficient), and an ensemble measure of central tendency is reported. In terms of the ratio of raw data to the amount of data used, this approach has a low rate of return. However, machine learning is one toolset that can potentially be leveraged by researchers to expand the utility of MPT datasets.

In this review, we give an overview of the ways machine learning methods have been implemented using trajectory datasets in the biomedical and life sciences literature. We also provide a brief overview of novel machine learning techniques implementing trajectory datasets from the artificial intelligence and computer science fields, including trajectory pre-processing steps, feature extraction, and machine learning algorithms. These tools have been leveraged to answer a number of classification problems based on trajectory datasets, including predicting whether a 3-point shot in basketball will be successful, determining maritime vessel type, identifying suspicious behavior in surveillance video, and classifying human actions (e.g. waving, throwing, jumping). With these tools, researchers should be able to apply these analyses to virus, organelle, receptor, cell, nanoparticle, and other biological trajectory datasets. Trajectories can classified based on properties of the moving agents (e.g. cell phenotype, nanoparticle surface functionality, cell receptor activity) or aspects of the tissue microenvironment (e.g. state of inflammation or injury, internalization state, tissue type).

Colloidal stability as a determinant of nanoparticle behavior in the brain

Curtis C.†, Toghani D.‡, Wong B.‡, Nance E.* Colloidal stability as a determinant of nanoparticle behavior in the brain. *Colloids and Surfaces B: Biointerfaces* (2018) 170, 673-682.

Drug delivery to the brain is challenging due to a highly regulated blood-brain barrier (BBB) and a complex brain microenvironment. Nanoparticles, due to their tailorability, provide promising platforms to enhance therapeutic delivery and achieve controlled release and disease-specific localization in the brain. However, we have yet to fully understand the complex interactions between nanoparticles and the bio-

logical environments in which they operate. It is important to perform a systematic study to characterize nanoparticle behavior as a function of ion composition, concentration, and pH in cerebrospinal fluid (CSF). These could alter nanoparticle biological identity and influence diffusive capability and cellular uptake. In this study, poly(ethylene glycol) (PEG)-coated and carboxyl-coated polystyrene (PS-PEG and PS-COOH respectively) nanoparticles (NPs) were used to evaluate the aggregation kinetics, colloidal stability, and diffusive capability of nanoparticles in conditions relevant to the brain microenvironment. Size, surface charge, and surface coating were varied in a range of CSF ion concentrations and compositions, pH conditions, and temperatures. Small changes in calcium concentration and pH destabilize nanoparticles in CSF. However, PS-PEG NPs remain stable over a wider variety of conditions than PS-COOH NPs, and have higher diffusion capabilities in both agarose gels, an in vitro model of the brain microenvironment, and an organotypic brain tissue slice model. These results demonstrate the need for steric stabilization to maintain nanoparticle colloidal stability in a wide range of conditions. Importantly, colloidal stabilization allows for increased diffusive capability and can be used to predict diffusive behavior in the brain microenvironment.

Predicting in situ nanoparticle behavior using multiple particle tracking and artifical neural networks

Curtis C.†, McKenna M.†, Pontes H., Toghani D., Choe E., Nance E.* Predicting in situ nanoparticle behavior using multiple particle tracking and artificial neural networks. *Submitted*

While nanoparticle-based therapeutic platforms have shown promise to improve drug efficacy through improved targeting, reduced toxicity, and enhanced stability, a limitation in the field is a lack of a systems-wide model to describe nanoparticle transport in the body. In this paper, we demonstrate a machine learning approach to evaluate the ability of artificial neural networks to predict both nanoparticle properties (size, protein adsorption) and aspects of the brain microenvironment (cell internalization, viscosity, brain region) using large (>100,000) trajectory datasets collected via multiple particle tracking in in vitro

gel models of the brain and organotypic brain slices. Our neural network achieved a 0.85 recall score when predicting gel viscosity based on trajectory datasets, compared to 0.49 using an obstruction scaling model. When predicting nanoparticle size based on trajectory datasets, our neural network achieved a 0.90 recall score compared to 0.83 using an optimized Stokes-Einstein predictor. Even in cases of more nuanced output variables where mathematical models are not available, such as protein adhesion, neural networks retained the ability to distinguish between particle populations (recall score of 0.77). This demonstrates the utility of nanoparticle trajectory datasets in probing local tissue microenvironments.

Design parameters of PEGylated brain-penetrating nanoparticles

Curtis C, Helmbrecht H., Epstein E., Pontes H., Toghani D., Nance E.* *Submitting*

Nanoparticles have been lauded for their promise in addressing common barriers to effective drug delivery: a lack of sustained or controlled release, biological barriers, and non-specific and off-target effects. Yet nanoparticle therapeutics are often viewed as a hammer and every potential disease a nail: a single platform shows some success in one disease model and is used without modification to attempt to treat an unrelated disease. Broad application of a single platform to multiple diseases is difficult since the complex interactions between nanoparticles and their biological environments is not yet fully understood. In this paper we seek to address one aspect of nanoparticle-microenvironment interactions: how modifying nanoparticle surface properties affect nanoparticle diffusive ability.

PEG is a common modulator of nanoparticle behavior is polyethylene glycol (PEG). Adding a PEG surface coating has been shown to improve nanoparticle stability as well as bequeath stealth properties. Researchers have also investigated how PEG properties (grafting density, chain length, surface functionality) alters key biological interaction parameters including pharmacokinetics, biodistribution, and cell uptake. However, it has yet to be demonstrated how these factors impact nanoparticle diffusive ability. In this paper, we modulate nanoparticle surface functionality, PEG grafting density, and PEG chain length and

observed changed in diffusive ability in an agarose gel model of the brain as well as an organotypic brain slice model. Furthermore, we utilize neural network predictors to classify individual nanoparticle trajectories by their particle type. These machine learning models demonstrate that nuanced aspects of particle design such as PEG grafting density and PEG chain length can be distinguished solely based on their trajectories. This suggests the potential of MPT datasets of fluorescent probes to be used as surrogate measures of nanoparticle properties in complex environments.

diff_classifier: Particle tracking parallelization

Curtis C.† Rokem A., Nance E.*. diff_classifier: Particle tracking parallelization. *Journal Open Source Software* 4(36):989.

The diff_classifier package seeks to address the issue of scale-up in multi-particle tracking (MPT) analyses via a parallelization approach. MPT is a powerful analytical tool that has been used in fields ranging from aeronautics to oceanography allowing researchers to collect spatial and velocity information of moving objects from video datasets. Examples include:

- Tracking tracers in ocean currents to study fluid flow
- Tracking molecular motors (e.g., myosin, kinesin) to assess motile activity
- Measuring intracellular trafficking by tracking membrane vesicles
- Assessing microrheological properties by tracking nanoparticle movement.

While a variety of tracking algorithms are available to researchers, a common problem is that data analysis usually depends on the use of graphical user interfaces, and relies on human input for accurate tracking. For example, particle detection often relies on the selection of a quality threshold, a numerical quantity distinguishing between “real” particles and “fake” Particles. If this threshold is too high, false positive trajectories result in skewed MSD profiles, and in extreme cases, cause the code to crash due to a lack of convergence in the particle linking step. If the threshold is too low, trajectories will be cut short resulting in a bias towards short fast-moving trajectories and could result in empty datasets.

Due to variations in experimental conditions and image quality, user-selected tracking parameters can vary widely from video to video. As parameter selection can also vary from user to user, this also brings up the issue of reproducibility. diff_classifier addresses these issues with regression tools to predict input tracking parameters and parallelized script-based implementations in Amazon Web Services (AWS), using the Simple Storage Service (S3) and Batch for data storage and computing, respectively, and relying on the Cloudknot software library for automating these interactions. By manually tracking a small subset of the entire video dataset to be analyzed (5-10 videos per experiment), users can predict tracking parameters based on intensity distributions of input images. This can simultaneously reduce time-to-first-result in MPT workflows and provide reproducible MPT results.

diff_classifier also includes downstream MPT analysis tools including mean squared displacement and feature calculations, visualization tools, and a principal component analysis implementation. MPT is commonly used to calculate and report ensemble-averaged diffusion coefficients of nanoparticles and other objects. We sought to expand the power of MPT analyses by changing the unit of analysis to individual particle trajectories. By including a variety of features (e.g., aspect ratio, boundedness, fractal dimension), with trajectory-level resolution, users can implement a range of data science analysis techniques to their MPT datasets.

3D printed coaxial nozzles for the extrusion of hydrogel tubes toward modeling vascular endothelium

Millik S. C., Dostie A M., Karis D. G., Smith P. T., McKenna M.†, Chan N.†, Curtis C†, Nance E., Theberge A. B., Nelson A. 3D printed coaxial nozzles for the extrusion of hydrogel tubes toward modeling vascular endothelium. *Biofabrication, accepted.*

Engineered tubular constructs made from soft biomaterials are employed in a myriad of applications in biomedical science. Potential uses of these constructs range from vascular grafts to conduits for enabling perfusion of engineered tissues and organs. The fabrication of standalone tubes or complex perfusable

constructs from biofunctional materials, including hydrogels, via rapid and readily accessible routes is desirable. Here we report a methodology in which customized coaxial nozzles are 3D printed using commercially available stereolithography (SLA) 3D printers. These nozzles can be used for the fabrication of hydrogel tubes via coextrusion of two shear-thinning hydrogels: an unmodified Pluronic F-127 (F127) hydrogel and an F127-bisurethane methacrylate (F127-BUM) hydrogel. We demonstrate that different nozzle geometries can be modeled via computer-aided design (CAD) and 3D printed in order to generate tubes or coaxial filaments with different cross-sectional geometries. Finally, we show that these tubes can be functionalized with collagen I to enable cell adhesion, and human umbilical vein endothelial cells (HUVECs) can be cultured on the luminal surfaces of these tubes to yield tubular endothelial monolayers. Our approach will enable the rapid fabrication of biofunctional tubular conduits that can ultimately be utilized for engineering in vitro models of tubular biological structures.

A ferret model of encephalopathy of prematurity

Wood T., Moralejo D., Corry K., Snyder J., Traudt C., Curtis C†, Nance E., Parikh P., Juul S.* A ferret model of encephalopathy of prematurity. *Developmental Neuroscience, May 10:1-15*.

There is an ongoing need for relevant animal models in which to test therapeutic interventions for infants with neurological sequelae of prematurity. The ferret is an attractive model species as it has a gyrified brain with a white-to-gray matter ratio similar to that in the human brain. A model of encephalopathy of prematurity was developed in postnatal day 10 (P10) ferret kits, considered to be developmentally equivalent to infants of 24–26 weeks' gestation. Cross-fostered P10 ferret kits received 5 mg/kg of lipopolysaccharide (LPS) before undergoing consecutive hypoxia-hyperoxia-hypoxia (60 min at 9%, 120 min at 60%, and 30 min at 9%). Control animals received saline vehicle followed by normoxia. The development of basic reflexes (negative geotaxis, cliff aversion, and righting) as well as gait coordination on an automated catwalk were assessed between P28 and P70, followed by ex vivo magnetic resonance imaging (MRI) and immunohistochemical analysis. Compared to controls, injured animals had slower overall reflex development between P28 and P40, as well as smaller hind-paw areas consistent with "toe walking" at P42.

Injured animals also displayed significantly greater lateral movement during CatWalk assessment as a result of reduced gait coordination. Ex vivo MRI showed widespread white-matter hyperintensity on T2-weighted imaging as well as altered connectivity patterns. This coincided with white-matter dysmaturation characterized by increased intensity of myelin basic protein staining, white-matter thinning, and loss of oligodendrocyte transcription factor 2 (OLIG2)-positive cells. These results suggest both pathological and motor deficits consistent with premature white-matter injury. This newborn ferret model can therefore provide an additional platform to assess potential therapies before translation to human clinical trials.

Group B streptococcus exploits vaginal epithelial exfoliation for ascending infection

Vornhagen J., Armistead B., Quach P., Santana-Ufret V., Boldenow E., Alishetti V., Melief C., Ngo L. Y., Whidbey C., Doran K. S., Curtis C., Nance E., Rajagopal L*. Group B streptococcus exploits vaginal epithelial exfoliation for ascending infection. *J. Clinical Investigation* (2018) 15(1):14.

Thirteen percent of pregnancies result in preterm birth or stillbirth, accounting for fifteen million preterm births and three and a half million deaths annually. A significant cause of these adverse pregnancy outcomes is in utero infection by vaginal microorganisms. To establish an in utero infection, vaginal microbes enter the uterus by ascending infection; however, the mechanisms by which this occurs are unknown. Using both in vitro and murine models of vaginal colonization and ascending infection, we demonstrate how a vaginal microbe, group B streptococcus (GBS), which is frequently associated with adverse pregnancy outcomes, uses vaginal exfoliation for ascending infection. GBS induces vaginal epithelial exfoliation by activation of integrin and β-catenin signaling. However, exfoliation did not diminish GBS vaginal colonization as reported for other vaginal microbes. Rather, vaginal exfoliation increased bacterial dissemination and ascending GBS infection, and abrogation of exfoliation reduced ascending infection and improved pregnancy outcomes. Thus, for some vaginal bacteria, exfoliation

promotes ascending infection rather than preventing colonization. Our study provides insight into mechanisms of ascending infection by vaginal microbes.

A

Supplementary datasets to Chapter 1

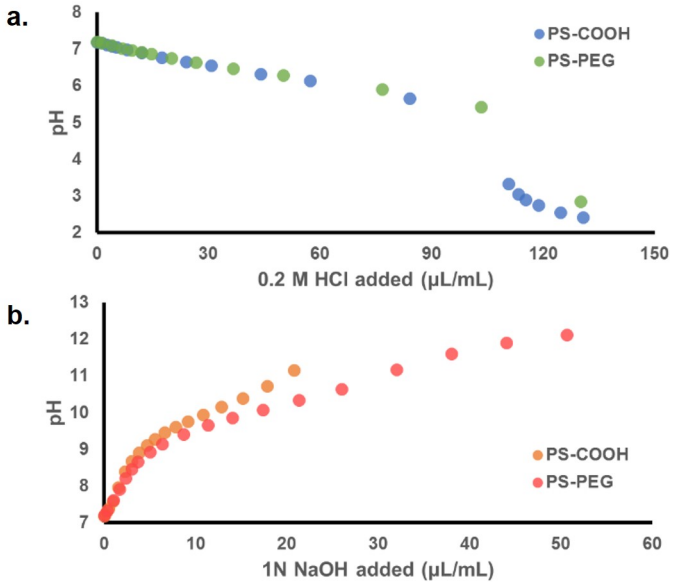

Figure A.1: Titration curves in ACSF. Titrations were performed in ACSF (4 mM $CaCl_2$, pH 7.2) with either PS-COOH or PS-PEG Nanoparticles at a concentration of 0.002% solids. For the acid curve, 0.2 M HCl was incrementally added and the pH measured. For the base curve, 1N NaOH was incrementally added and the pH measured. Measurements were taken such that the pH range 3-11 was covered. In the pH range 6-9, the PS-COOH and PS-PEG curves differ very little. Below pH 6, pH drops more rapidly in the solution with PS-COOH Nanoparticles. Above pH 9, the pH increases more rapidly in the solution with PS-COOH Nanoparticles.

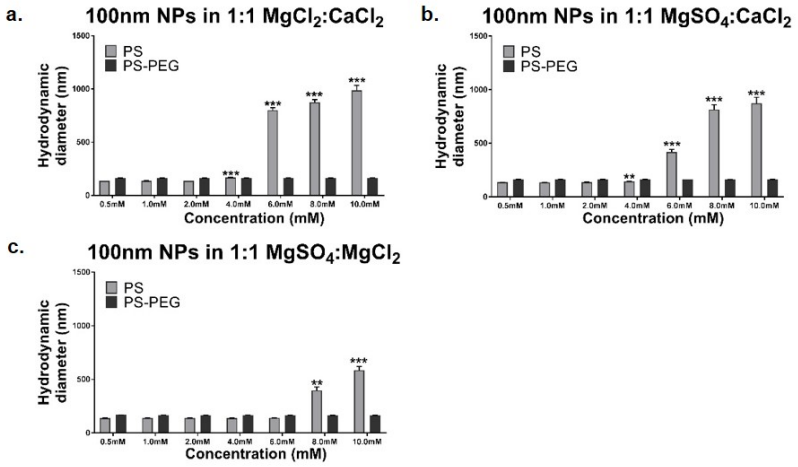

Figure A.2: Hydrodynamic diameters of 10nm PS-COOH and PS-PEG NPs in increasing concentrations of (a) 1:1 magnesium chloride:calcium chloride solution, (b) 1:1 magnesium sulfate:calcium chloride solution, and (c) magnesium sulfate:magnesium chloride solution (n=3). All values are reported as mean ± SEM. Significance as compared with 0.5 mM condition are indicated by * $p < 0.033$, ** $p < 0.002$, *** $p < 0.001$.

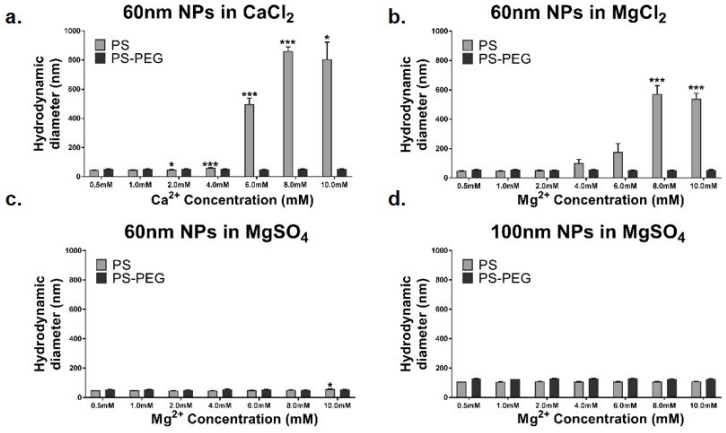

Figure A.3: Hydrodynamic diameters of 60nm PS-COOH and PS-PEG NPs in increasing concentrations of (a) calcium chloride solution, (b) magnesium chloride solution, and (c) magnesium sulfate solution (n=3). (d) Hydrodynamic diameters of 100nm PS-COOH and PS-PEG NPs in increasing concentrations of magnesium sulfate (n=3). All values are reported as mean ± SEM. Significance as compared with 0.5 mM condition are indicated by * $p < 0.033$, ** $p < 0.002$, *** $p < 0.001$.

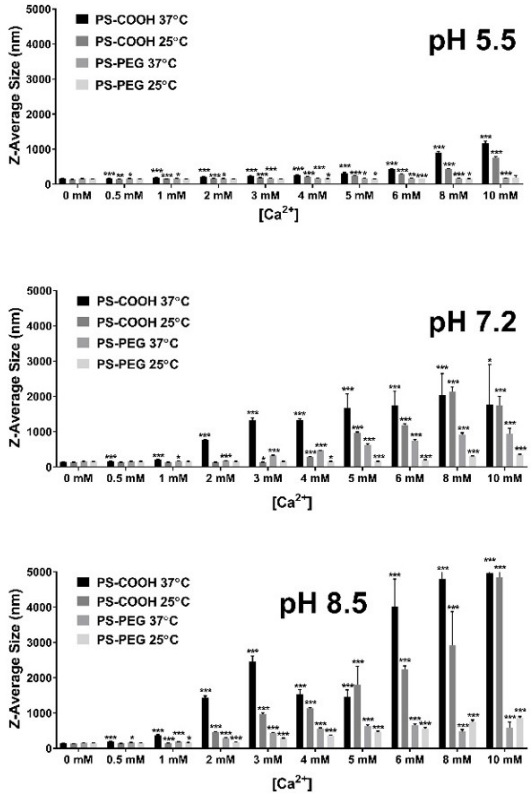

Figure A.4: Aggregation profiles of PS-COOH/PS-PEG NPs at 25°C/37°C in ACSF pH (a) 5.5, (b) 7.2, and (c) 8.5 at increasing calcium chloride concentrations (n=5). All values are reported as mean ± SEM. Significance as compared with 0 mM condition are indicated by * $p < 0.033$, ** $p < 0.002$, *** $p < 0.001$.

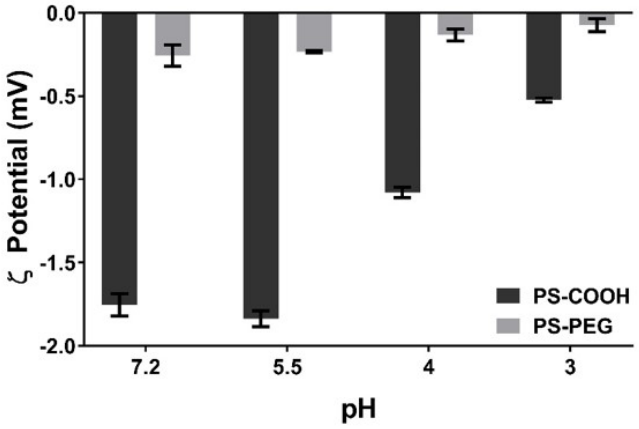

Figure A.5: Measured ζ-potentials of PS-COOH and PS-PEG NPs in ACSF with 3 mM $CaCl_2$ as a function of pH.

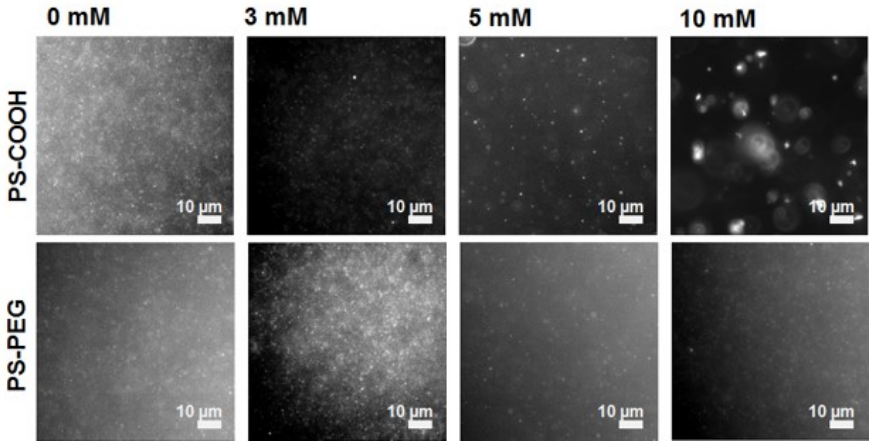

Figure A.6: Representative frames from diffusion videos in gels with two different particle types (PS-COOH and PS-PEG) and four different calcium concentrations (0, 3, 5, and 10 mM) in ACSF. Scale bars: 10 μm.

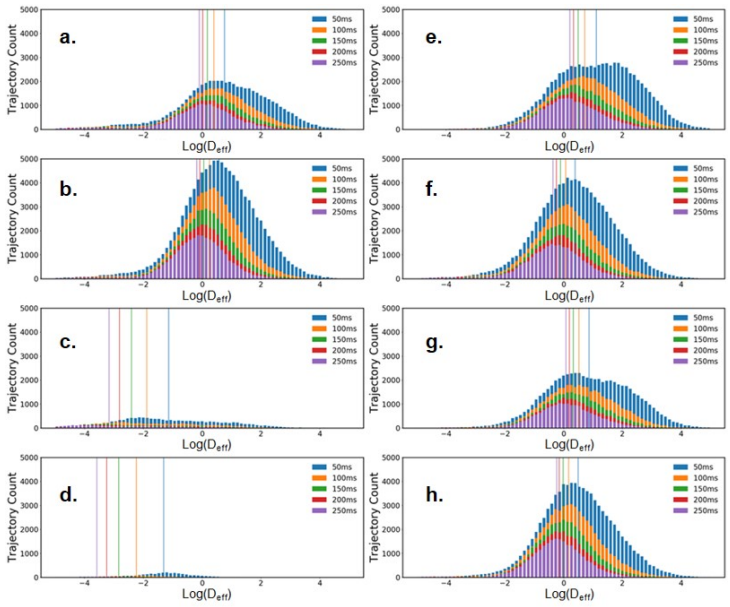

Figure A.7: Representative diffusion coefficient distributions of (a-d) PS-COOH and (e-h) PS-PEG NPs in 0, 3, 5, and 10 mM calcium chloride in 0.4% agarose gels constituted with ACSF as measured at 50, 100, 150, 200, and 250 ms time lags.

Table A.1: Mean hydrodynamic diameters of 60, 100, 200, and 1000 PS-COOH and PS-PEG nanoparticles measured in ACSF after 24 hour incubation at 37°C. Data was collected via DLS (n=3). All values reported are mean ± SEM.

Particle Size (nm)	Surface Coating	Mean Hydrodynamic Diameter in ACSF ± SEM (nm)
60	COOH	469.2 ± 42.3
60	PEG	77.7 ± 7.1
100	COOH	378.8 ± 63.5
100	PEG	125.7 ± 7.4
200	COOH	635.8 ± 20.8
200	PEG	350.3 ± 27.8
1000	COOH	1544 ± 65
1000	PEG	1233 ± 8

B

Supplementary datasets to Chapter 2

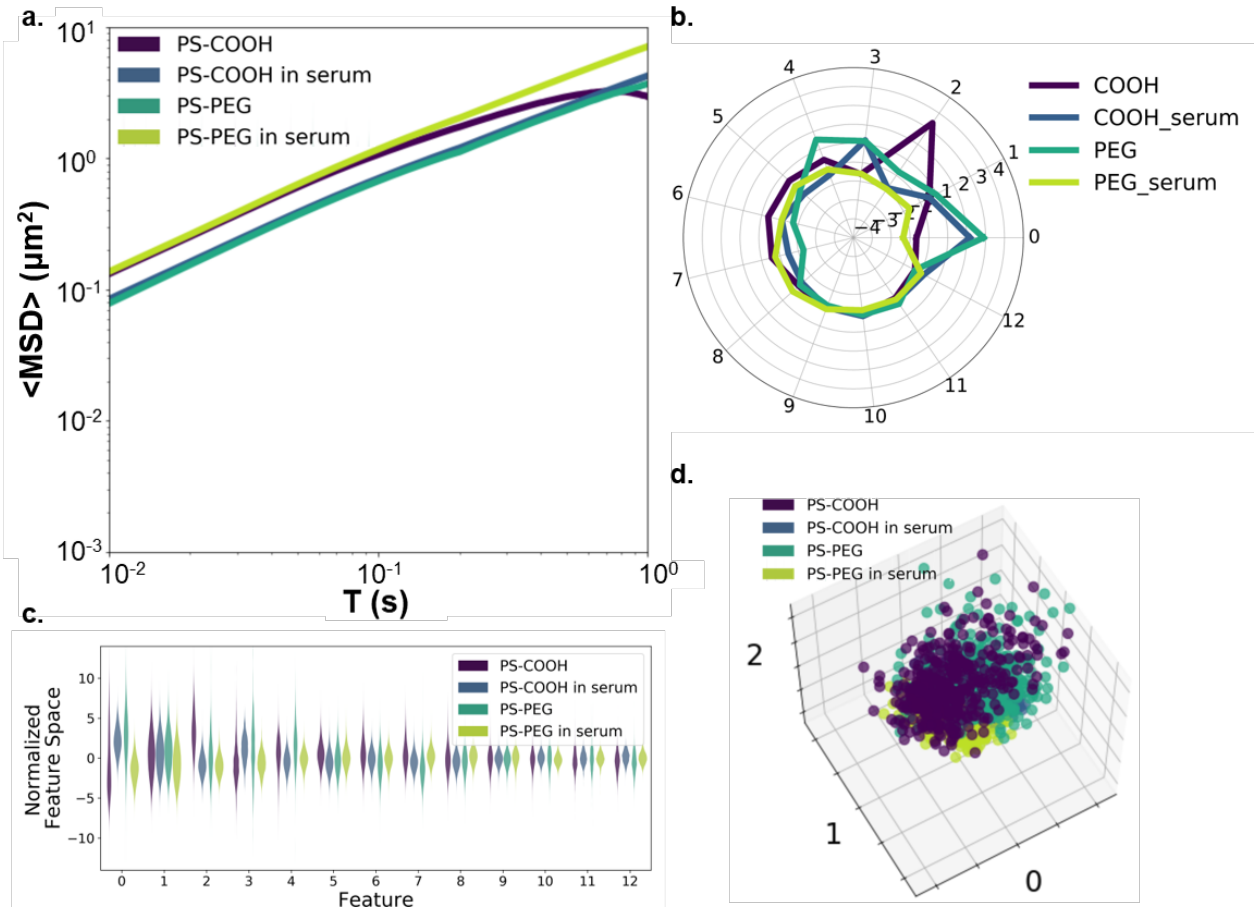

Figure B.1: (a) Ensemble-averaged precision-weighted MSD profiles of 100-nm PS-COOH NPs, PS-PEG NPs, PS-COOH NPs incubated in horse serum, and PS-PEG NPs incubated in serum in 0.4% agarose gel (n=2 wells, 5 videos per well). 95-percent confidence intervals (CIs) represented as semi-transparent shaded regions. (b) Average component profile of PCA analysis stratified by particle type. (c) Principle component distributions of PCA analysis stratified by particle type. (d) First three primary components of 400 randomly selected trajectories per particle type from entire trajectory dataset plotted against each other.

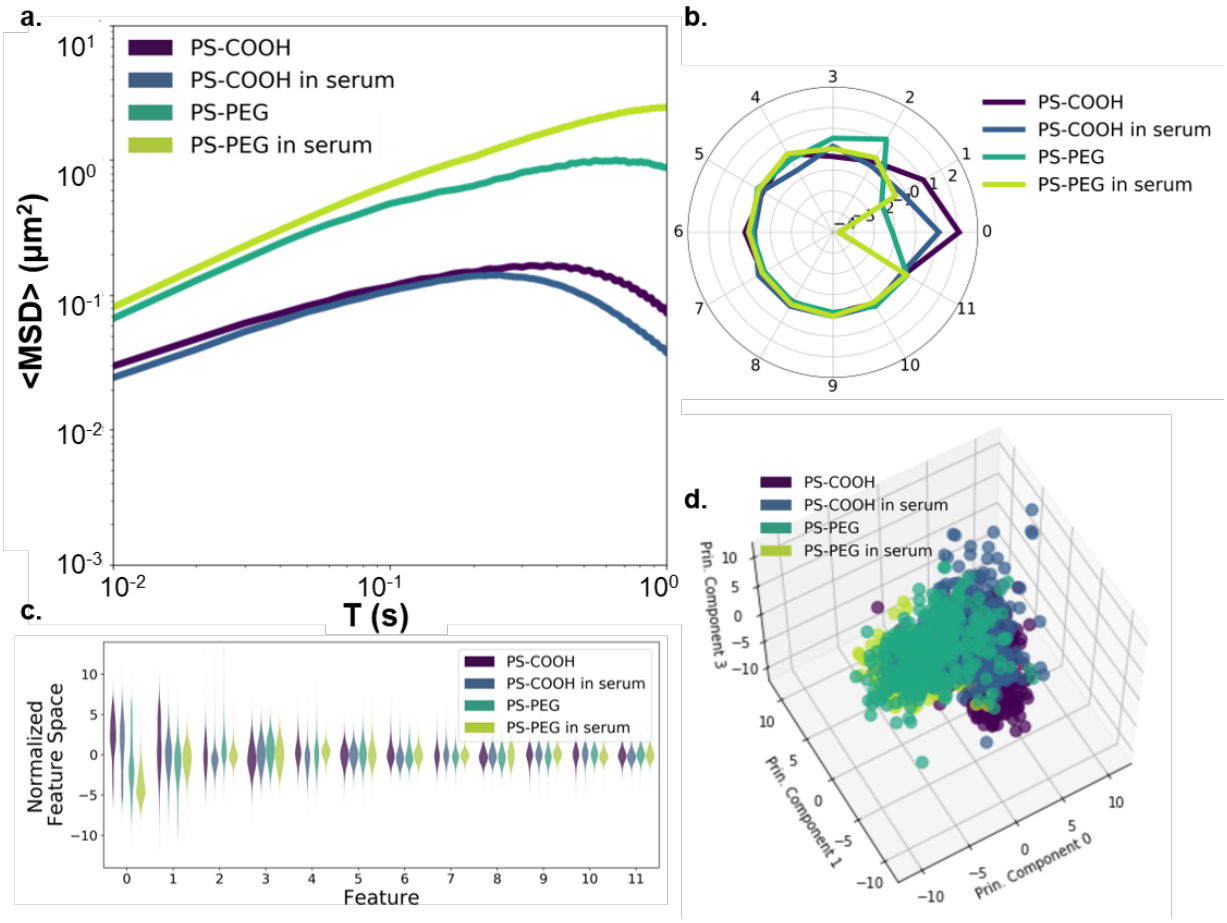

Figure B.2: (a) Geometric ensemble-averaged precision-weighted MSD profiles of 100-nm PS-COOH NPs, PS-PEG NPs, PS-COOH NPs incubated in horse serum, and PS-PEG NPs incubated in serum in cortex of 300μm-thick rat brain slices (n=2 pups, n=2 slices per pup, 10 videos per slice). 95% confidence intervals (CIs) represented as semi-transparent shaded regions. (b) Average component profile of PCA analysis stratified by particle type. (c) Principle component distributions of PCA analysis stratified by particle type. (d) First three primary components of 400 randomly selected trajectories per particle type from entire trajectory dataset plotted against each other.

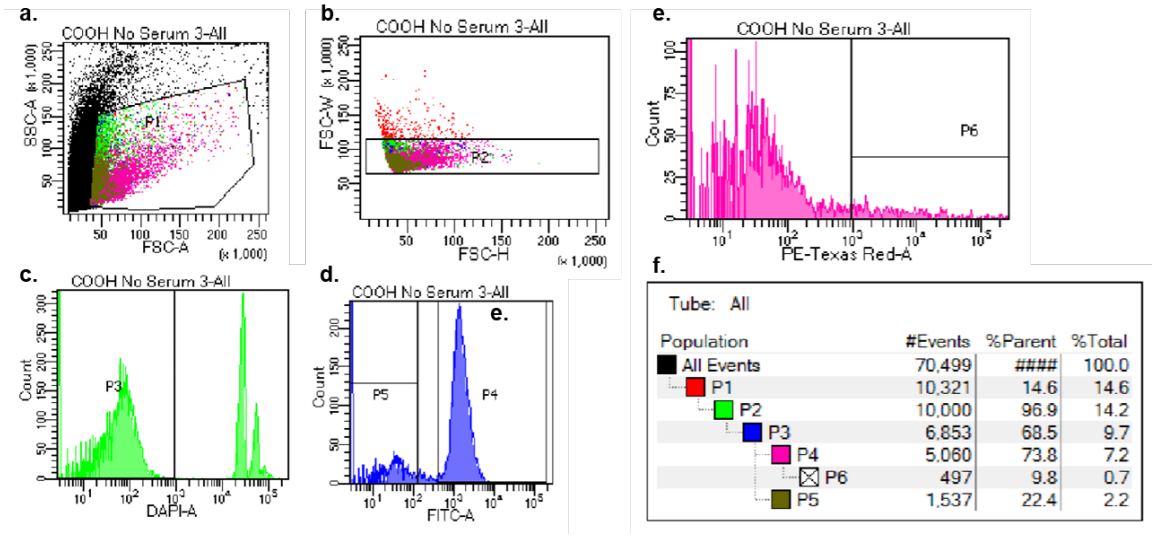

Figure B.3: Example raw FACS data for surface functionality-dependent nanoparticle cell uptake study in microglial cells in organotypic rat brain slice model. (a) Polygonal forward-scatter side-scatter gate to filter out cell debris, (b) forward scatter-height and forward scatter-width gate to filter out cell doublets, (c) DAPI gate to filter out dead cells, (d) FITC gate to filter out non-microglial cells, (e) Texas Red threshold defining PS-positive cells, and (f) population map.

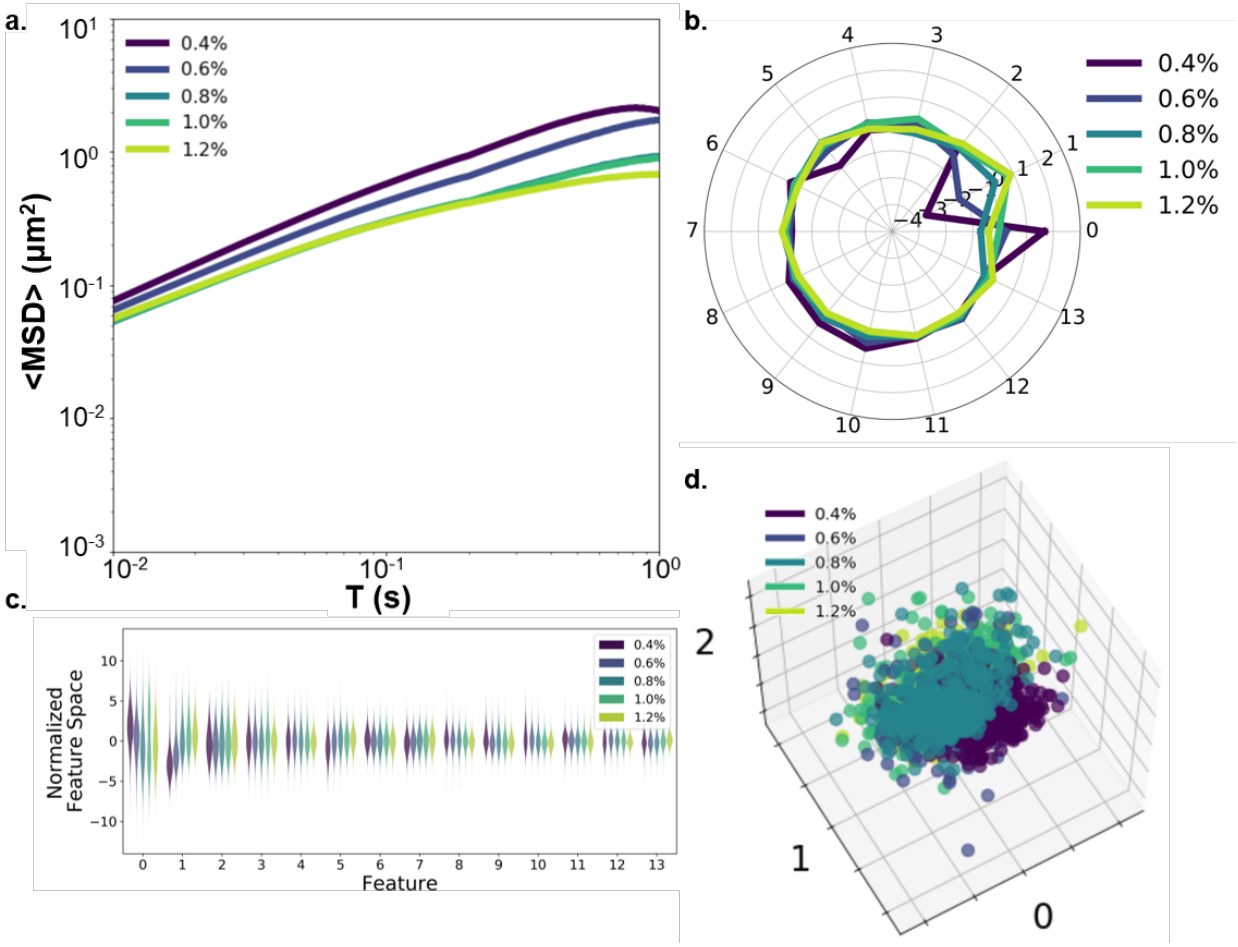

Figure B.4: (a) Geometric ensemble-averaged precision-weighted MSD profiles of 100-nm PS-COOH NPs in 0.4%, 0.6%, 0.8%, 1.0%, and 1.2% agarose gels (n=2 wells per condition). 95% confidence intervals (CIs) represented as semi-transparent shaded regions. (purple: 0.4%, blue: 0.6%, teal: 0.8%, light-green: 1.0%, yellow-green: 1.2%). (b) Average component profile of PCA analysis stratified by percent agarose. (c) Principle component distributions of PCA analysis stratified by percent agarose. (d) First three primary components of 400 randomly selected trajectories per size from entire trajectory dataset plotted against each other.

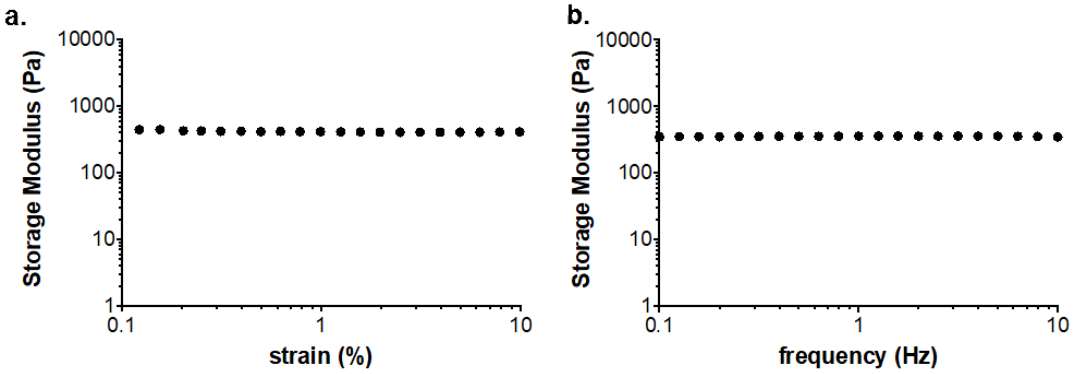

Figure B.5: The linear viscoelastic region of 0.4% agarose was determined by performing a strain (a) and frequency (b) sweep following a 4 h incubation at 22°C. For the strain sweep, the frequency was fixed at 1 Hz, and the storage and loss moduli were measured at various strains (0.1 – 10%). For the frequency sweep, the strain was fixed at 2%, and the storage and loss moduli were measured at various frequencies (0.1 – 10 Hz). The sweeps demonstrate that at 2% strain and 2 Hz, the agarose gel is in the linear viscoelastic region because minor changes in strain or frequency do not change the measured storage modulus.

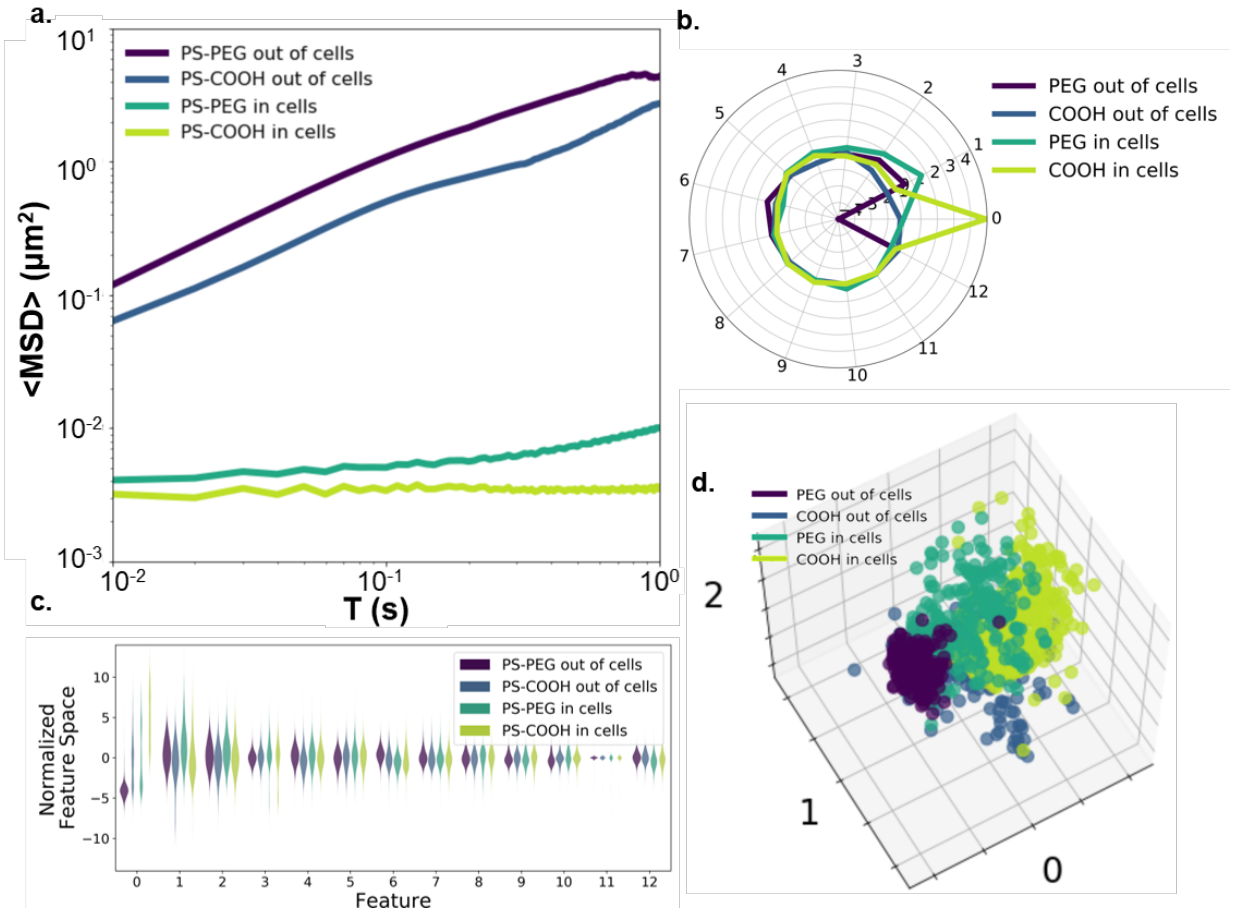

Figure B.6: (a). Geometric ensemble-averaged precision-weighted <MSD> profiles of PS-COOH and PS-PEG NPs diffusing either intra- or extracellularly (n=2 wells per condition, 5 videos per well). 95% confidence intervals (CIs) represented as semi-transparent shaded regions. (purple: PS-PEG out of cells, blue: PS-COOH out of cells, teal: PS-PEG in cells, yellow-green: PS-COOH in cells). (b) Average component profile of PCA analysis stratified by particle type. (c) Principle component distributions of PCA analysis stratified by particle type. (d) First three primary components of 400 randomly selected trajectories per particle type from the entire trajectory dataset plotted against each other.

Table B.1: Descriptions and calculations for each trajectory feature using trajectories from multiple particle tracking.

Feature	Description	How it is determined
alpha (α)	Exponent of the anomalous diffusion equation.	Non-linear least squares is used to fit raw MSD vs. lag time (τ) data to the anomalous diffusion equation: $MSD = 4D_{fit}\tau^{\alpha}$
Effective diffusion coefficient (D_{fit})	Coefficient of the anomalous diffusion equation.	Non-linear least squares is used to fit raw MSD vs. lag time (τ) data to the anomalous diffusion equation: $MSD = 4D_{fit}\tau^{\alpha}$
Kurtosis (K)	The fourth moment of the projected positions on the dominant eigenvector of the radius of gyration tensor (T).	$K = \frac{1}{N}\sum_{i=0}^{N-1}\frac{(x_i^p - \overline{x^p})^4}{\sigma_{x^p}^4}$
Asymmetry1 (a)	Characterizes the asymmetry of the trajectory. Asymmetry1 equals 0 for circularly symmetric trajectories and 1 for linear trajectories.	$a = \frac{(\lambda_1^2 - \lambda_2^2)^2}{(\lambda_1^2 + \lambda_2^2)^2}$, where λ_1 and λ_2 are the eigenvalues of radius of gyration tensor T: $\mathrm{T} = \begin{pmatrix} \frac{1}{N}\sum_{j=1}^{N}(x_j - \langle x\rangle)^2 & \frac{1}{N}\sum_{j=1}^{N}(x_j - \langle x\rangle)(y_j - \langle y\rangle) \\ \frac{1}{N}\sum_{j=1}^{N}(x_j - \langle x\rangle)(y_j - \langle y\rangle) & \frac{1}{N}\sum_{j=1}^{N}(y_j - \langle y\rangle)^2 \end{pmatrix}$
Asymmetry2 (a_2)	The ratio of the smaller to larger principal radius of gyration.	$a_2 = \frac{\lambda_2}{\lambda_1}$
Asymmetry3 (a_3)	An asymmetry feature that accounts for non-cylindrically symmetric point distributions.	$a_3 = -\log\left(1 - \frac{(\lambda_1 - \lambda_2)^2}{2(\lambda_1 + \lambda_2)^2}\right)$
Aspect ratio (AR)	The ratio of the long and short side of the trajectory's minimum bounding rectangle. Perfectly symmetric trajectories have an aspect ratio of 1, and aspect ratio increases as trajectories become more elongated	$AR = \begin{cases} \frac{\lvert x_{max} - x_{min}\rvert}{\lvert y_{max} - y_{min}\rvert}, & \lvert y_{max} - y_{min}\rvert < \lvert x_{max} - x_{min}\rvert \\ \frac{\lvert y_{max} - y_{min}\rvert}{\lvert x_{max} - x_{min}\rvert}, & \lvert y_{max} - y_{min}\rvert \geq \lvert x_{max} - x_{min}\rvert \end{cases}$
Elongation	An estimation of amount of extension of the trajectory from its centroid.	Elongation $= 1 - (\frac{1}{AR})$
Boundedness (B)	Boundedness quantifies how much a particle with diffusion coefficient D_{eff} is restricted by a circular confinement of radius r when diffusing for a period of time NΔt.	$B = \frac{D_{eff}N\Delta t}{r^2}$
Fractal Dimension (D_f)	Fractal dimension is a measure of how "complicated" a self similar figure is.	$D_f = \frac{\log(N)}{\log(NdL^{-1})}$
Trappedness (p_t)	The probability (p_t) that a particle with diffusion coefficient D_{eff} is trapped in a region (r_0) for a period of time $N\Delta t$.	$p_t = 1 - \exp(0.2048 - 0.25117(\frac{D_{eff}N\Delta t}{r_0^2}))$
Efficiency (E)	The ratio of squared net displacement to the sum of squared step lengths.	$E = \frac{(x_{N-1} - x_0)^2 + (y_{N-1} - y_0)^2}{\sum_{i=1}^{N-1}(x_i - x_{i-1})^2 + (y_i - y_{i-1})^2}$
Straightness (S)	The ratio of net displacement to the sum of step lengths.	$S = \frac{\sqrt{(x_{N-1} - x_0)^2 + (y_{N-1} - y_0)^2}}{\sum_{i=1}^{N}\sqrt{(x_i - x_{i-1})^2 + (y_i - y_{i-1})^2}}$
MSD Ratio (MSD_{n_1,n_2})	MSD ratio characterizes the shape of the MSD curve. For Brownian motion, it is 0; For restricted motion it is < 0; For directed motion it is > 0.	$MSD_{n_1,n_2} = \frac{MSD_{n_1}}{MSD_{n_2}} - \frac{n_1}{n_2}$
Frames	The total number of frames the trajectory spans.	Frames = N
D_{eff1}	Effective diffusion coefficient at 0.1 s.	$D_{eff1} = \frac{MSD_{\tau=0.1}}{4*0.1}$
D_{eff2}	Effective diffusion coefficient at 1 s.	$D_{eff2} = \frac{MSD_{\tau=1}}{4*1}$

MSD: mean squared displacement
N: number of frames
σ_{x^p}: standard deviation of the projected 2D positions
λ_1,λ_2: eigenvalues of radius of gyration tensor
D_{eff}: effective diffusion coefficient
r: radius of circular confinement
n: frame number
r_0: radius of trapped region
$\bar{\imath}_{Back}$: average background pixel intensity
τ: lag time
x^p: projected 2D position
T: gyration tensor
$\langle x\rangle$,$\langle y\rangle$: average x and y location
Δt: inverse of frame rate
d: largest distance between any two positions
L: total length (sum over all steplengths) of trajectory
σ_I: standard deviation of pixel intensities

Table B.2: Classifier metrics using nanoparticle trajectories to predict particle type (PS-COOH, PS-COOH in serum, PS-PEG, and PS-PEG in serum) in organotypic rat brain slice model using a leave-one-out train-test split (n=2 pups, n=2 slices per pup).

	Neural Network local avg. 3-1 train-test (1)		Neural Network local avg. 3-1 train-test (2)		Neural Network local avg. 3-1 train-test (3)		Neural Network local avg. 3-1 train-test (4)	
	Training	Test	Training	Test	Training	Test	Training	Test
COOH	0.786	0.210	0.776	0.533	0.696	0.735	0.760	0.506
COOH in serum	0.849	0.706	0.832	0.714	0.791	0.634	0.866	0.330
PEG	0.475	0.069	0.322	0.039	0.510	0.105	0.504	0.045
PEG in serum	0.863	0.740	0.875	0.522	0.791	0.578	0.909	0.726
Avg/Tot	0.743	0.431	0.701	0.452	0.697	0.513	0.756	0.402

C

Supplementary datasets to Chapter 3

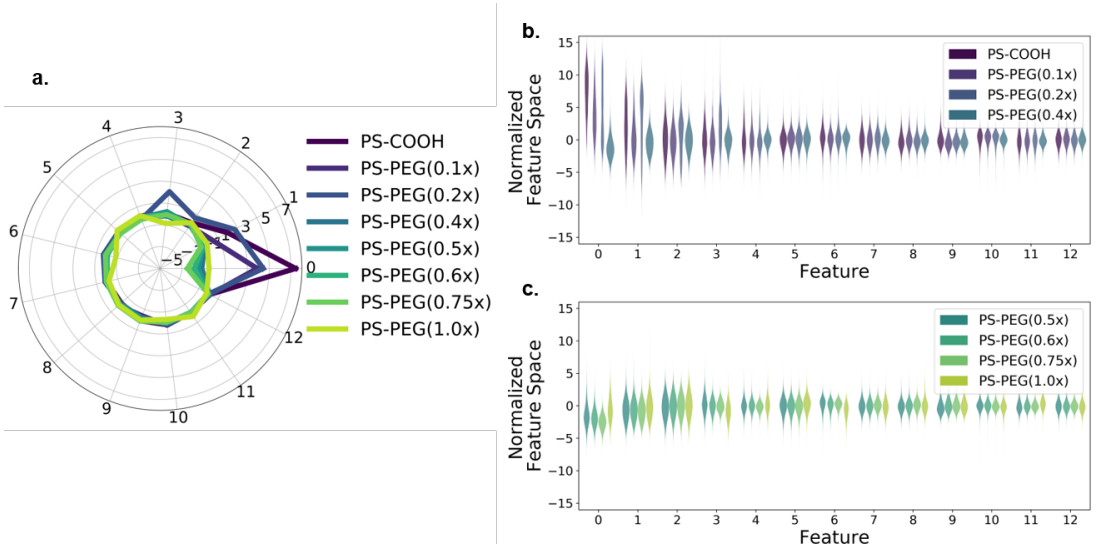

Figure C.1: PCA analysis of PEG grafting density-dependent diffusion study. (a.) Average component profile of PCA analysis stratified by PEG grafting density (dark purple: PS-COOH, light purple: PS-PEG(0.1x), blue-violent: PS-PEG(0.2x), blue-green: PS-PEG(0.4x), teal: PS-PEG(0.5x), seafoam green: PS-PEG(0.6x), light green: PS-PEG(0.75x), and yellow-green: PS-PEG(1x)). (b., c.) Principle component distribution of PCA analysis stratified by PEG grafting density.

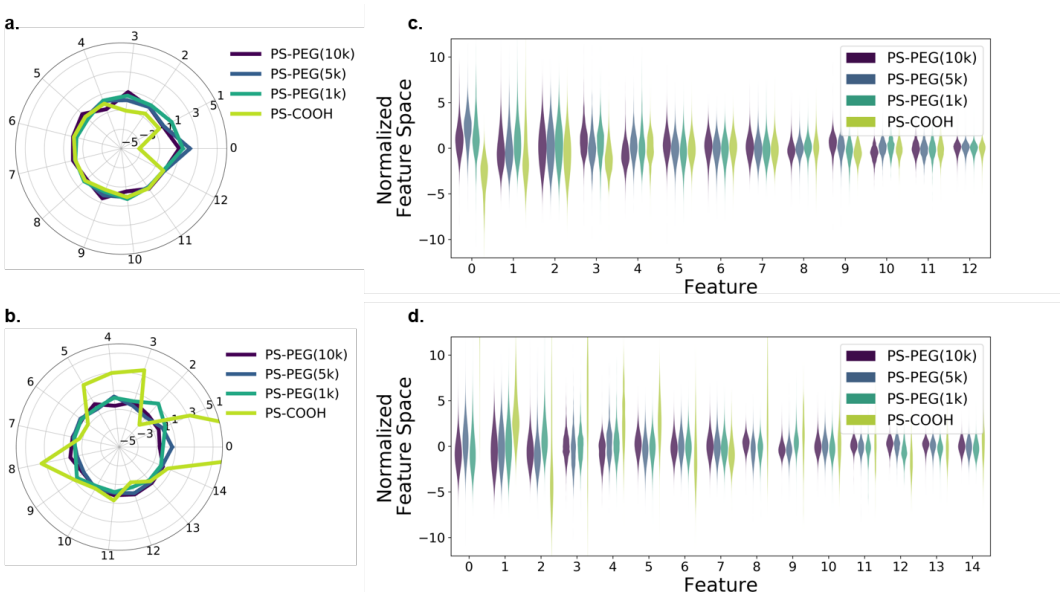

Figure C.2: PCA analysis of PEG chain length-dependent diffusion data in 0.4% agarose gels constituted with (a., c.) ACSF (2mM $CaCl_2$) and (b., d.) ACSF (3mM $CaCl_2$). (a., b.) Average component profiles of PCA analyses stratified by PEG chain length (yellow-green: PS-COOH, teal: PS-PEG(1k), blue: PS-PEG(5k), and purple: PS-PEG(10k)) for data collected in 0.4% agarose gels constituted with (a.) ACSF (2mM $CaCl_2$) and (b.) ACSF (3mM $CaCl_2$). (c., d.) Principle component distributions of PCA analyses stratified by PEG chain length for data collected in 0.4% agarose gels constituted with (c.) ACSF (2mM $CaCl_2$) and (d.) ACSF (3mM $CaCl_2$).

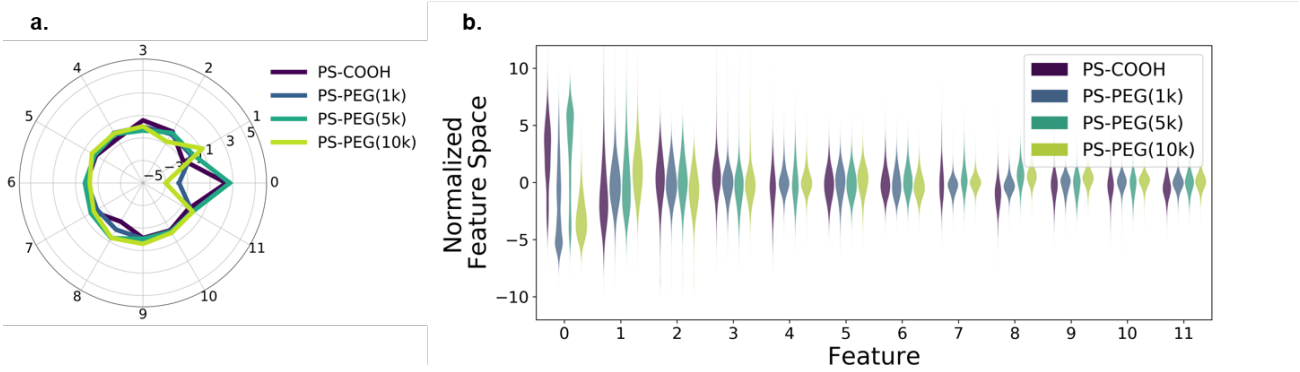

Figure C.3: PCA analysis of PEG chain length-dependent diffusion data in an organotypic brain slice model. (a.) Average component profiles of PCA analyses stratified by PEG chain length (yellow-green: PS-COOH, teal: PS-PEG(1k), blue: PS-PEG(5k), and purple: PS-PEG(10k)). (b.) Principle component distribution of PCA analysis stratified by PEG chain length.

Table C.1: Classification metrics for particles of varying PEG chain length in organotypic brain slice model (Leave-One-Out for slices 1 and 2)

	Sample Size (LOO 1)		Log Median Predictor (LOO 1)		Neural Network Predictor (LOO 1)		Sample Size (LOO 2)		Log Median Predictor (LOO 2)		Neural Network Predictor (LOO 2)	
	Training	Test	Training	Test	Training	Test	Training	Test	Training	Test	Training	Test
PS-COOH	33772	55914	0.67	0.42	0.91	0.41	87449	2187	0.60	0.58	0.93	0.78
PS-PEG(1k)	131041	85372	0.28	0.32	0.94	0.05	209745	6668	0.21	0.20	0.95	0.78
PS-PEG(5k)	134226	9163	0.38	0.11	0.89	0.25	136383	7006	0.27	0.08	0.86	0.28
PS-PEG(10k)	65294	8628	0.32	0.22	0.91	0.87	63378	10554	0.48	0.54	0.85	0.85
Avg/Tot	354333	159077	0.41	0.27	0.91	0.39	496955	26415	0.39	0.35	0.90	0.67

Table C.2: Classification metrics for particles of varying PEG chain length in organotypic brain slice model (Leave-One-Out for slices 3 and 4)

	Sample Size (LOO 3)		Log Median Predictor (LOO 3)		Neural Network Predictor (LOO 3)		Sample Size (LOO 4)		Log Median Predictor (LOO 4)		Neural Network Predictor (LOO 4)	
	Training	Test	Training	Test	Training	Test	Training	Test	Training	Test	Training	Test
PS-COOH	87488	2198	0.60	0.42	0.91	0.39	86221	3465	0.74	0.64	0.93	0.62
PS-PEG(1k)	208480	7933	0.22	0.23	0.94	0.75	163004	53409	0.35	0.05	0.95	0.93
PS-PEG(5k)	134409	8980	0.28	0.12	0.84	0.20	50043	93346	0.51	0.00	0.66	0.00
PS-PEG(10k)	67281	6641	0.49	0.44	0.86	0.84	55442	18480	0.21	0.16	0.79	0.54
Avg/Tot	497658	25752	0.40	0.30	0.89	0.55	354710	168700	0.45	0.21	0.83	0.52

Table C.3: Classification metrics for particles of varying PEG chain length in organotypic brain slice model (Leave-One-Out for slices 5 and 6)

	Sample Size (LOO 5)		Log Median Predictor (LOO 5)		Neural Network Predictor (LOO 5)		Sample Size (LOO 6)		Log Median Predictor (LOO 6)		Neural Network Predictor (LOO 6)	
	Training	Test	Training	Test	Training	Test	Training	Test	Training	Test	Training	Test
PS-COOH	85045	4601	0.62	0.46	0.94	0.60	68365	21321	0.55	0.91	0.91	0.74
PS-PEG(1k)	178947	37466	0.20	0.15	0.95	0.94	190848	25565	0.22	0.26	0.95	0.71
PS-PEG(5k)	140698	2691	0.25	0.20	0.87	0.28	121186	22203	0.25	0.04	0.85	0.34
PS-PEG(10k)	66286	7636	0.53	0.67	0.86	0.53	51929	21993	0.51	0.46	0.85	0.62
Avg/Tot	470976	52394	0.40	0.37	0.91	0.59	432328	91082	0.38	0.42	0.89	0.60

References

1. Petros, R.A., DeSimone, J.M.: Strategies in the design of nanoparticles for therapeutic applications. Nat Rev Drug Discov. 9, 615–27 (2010). doi:10.1038/nrd2591

2. Satalkar, P., Elger, B.S., Hunziker, P., Shaw, D.: Challenges of clinical translation in nanomedicine: A qualitative study. Nanomedicine: Nanotechnology, Biology and Medicine. 12, 893–900 (2016)

3. Murday, J.S., Siegel, R.W., Stein, J., Wright, J.F.: Translational nanomedicine: Status assessment and opportunities. Nanomedicine: Nanotechnology, Biology and Medicine. 5, 251–273 (2009)

4. Curtis, C., Zhang, M., Liao, R., Wood, T., Nance, E.: Systems-level thinking for nanoparticle-mediated therapeutic delivery to neurological diseases. Wiley Interdiscip Rev Nanomed Nanobiotechnol. 9, (2017). doi:10.1002/wnan.1422

5. Arnold, F.H.: Design by directed evolution. Accounts of chemical research. 31, 125–131 (1998)

6. Valencia, P.M., Farokhzad, O.C., Karnik, R., Langer, R.: Microfluidic technologies for accelerating the clinical translation of nanoparticles. Nature nanotechnology. 7, 623 (2012)

7. Dahlman, J.E., Kauffman, K.J., Xing, Y., Shaw, T.E., Mir, F.F., Dlott, C.C., Langer, R., Anderson, D.G., Wang, E.T.: Barcoded nanoparticles for high throughput in vivo discovery of targeted therapeutics. Proceedings of the National Academy of Sciences. 114, 2060–2065 (2017)

8. Alavijeh, M.S., Chishty, M., Qaiser, M.Z., Palmer, A.M.: Drug metabolism and pharmacokinetics, the blood-brain barrier, and central nervous system drug discovery. NeuroRx. 2, 554–71 (2005). doi:10.1602/neurorx.2.4.554

9. Rooy, I. van, Cakir-Tascioglu, S., Hennink, W.E., Storm, G., Schiffelers, R.M., Mastrobattista, E.: In vivo methods to study uptake of nanoparticles into the brain. Pharm Res. 28, 456–71 (2011). doi:10.1007/s11095-010-0291-7

10. Allen, T.M., Cullis, P.R.: Drug delivery systems: Entering the mainstream. Science. 303, 1818–22 (2004). doi:10.1126/science.1095833

11. Alexis, F., Pridgen, E., Molnar, L.K., Farokhzad, O.C.: Factors affecting the clearance and biodistribution of polymeric nanoparticles. Mol Pharm. 5, 505–15 (2008). doi:10.1021/mp800051m

12. Hutter, E., Boridy, S., Labrecque, S., Lalancette-Hebert, M., Kriz, J., Winnik, F.M., Maysinger, D.: Microglial response to gold nanoparticles. ACS Nano. 4, 2595–606 (2010). doi:10.1021/nn901869f

13. Neumann, H., Kotter, M.R., Franklin, R.J.: Debris clearance by microglia: An essential link between degeneration and regeneration. Brain. 132, 288–95 (2009). doi:10.1093/brain/awn109

14. Floyd, R.A., Hensley, K.: Oxidative stress in brain aging. Implications for therapeutics of neurodegenerative diseases. Neurobiol Aging. 23, 795–807 (2002)

15. Bonneh-Barkay, D., Wiley, C.A.: Brain extracellular matrix in neurodegeneration. Brain pathology. 19, 573–585 (2009)

16. Lau, L.W., Cua, R., Keough, M.B., Haylock-Jacobs, S., Yong, V.W.: Pathophysiology of the brain extracellular matrix: A new target for remyelination. Nature Reviews Neuroscience. 14, 722 (2013)

17. Dantzer, R., O'Connor, J.C., Freund, G.G., Johnson, R.W., Kelley, K.W.: From inflammation to sickness and depression: When the immune system subjugates the brain. Nature reviews neuroscience. 9, 46 (2008)

18. Ekdahl, C.T., Claasen, J.-H., Bonde, S., Kokaia, Z., Lindvall, O.: Inflammation is detrimental for neu-

rogenesis in adult brain. Proceedings of the National Academy of Sciences. 100, 13632–13637 (2003)

19. Love, S.: Oxidative stress in brain ischemia. Brain pathology. 9, 119–131 (1999)

20. Prabakaran, S., Swatton, J., Ryan, M., Huffaker, S., Huang, J.-J., Griffin, J., Wayland, M., Freeman, T., Dudbridge, F., Lilley, K., others: Mitochondrial dysfunction in schizophrenia: Evidence for compromised brain metabolism and oxidative stress. Molecular psychiatry. 9, 684 (2004)

21. Palmer, A.M., Marion, D.W., Botscheller, M.L., Swedlow, P.E., Styren, S.D., DeKosky, S.T.: Traumatic brain injury-induced excitotoxicity assessed in a controlled cortical impact model. Journal of neurochemistry. 61, 2015–2024 (1993)

22. Tabrizi, S., Cleeter, M., Xuereb, J., Taanman, J.-W., Cooper, J., Schapira, A.: Biochemical abnormalities and excitotoxicity in huntington's disease brain. Annals of Neurology: Official Journal of the American Neurological Association and the Child Neurology Society. 45, 25–32 (1999)

23. Raghupathi, R.: Cell death mechanisms following traumatic brain injury. Brain pathology. 14, 215–222 (2004)

24. Lipton, P.: Ischemic cell death in brain neurons. Physiological reviews. 79, 1431–1568 (1999)

25. Linninger, A.A., Xenos, M., Zhu, D.C., Somayaji, M.R., Kondapalli, S., Penn, R.D.: Cerebrospinal fluid flow in the normal and hydrocephalic human brain. IEEE Transactions on Biomedical Engineering. 54, 291–302 (2007)

26. Iliff, J.J., Wang, M., Liao, Y., Plogg, B.A., Peng, W., Gundersen, G.A., Benveniste, H., Vates, G.E., Deane, R., Goldman, S.A., Nagelhus, E.A., Nedergaard, M.: A paravascular pathway facilitates csf flow through the brain parenchyma and the clearance of interstitial solutes, including amyloid beta. Sci Transl Med. 4, 147ra111 (2012). doi:10.1126/scitranslmed.3003748

27. Zhao, Z., Nelson, A.R., Betsholtz, C., Zlokovic, B.V.: Establishment and dysfunction of the blood-brain barrier. Cell. 163, 1064–1078 (2015). doi:10.1016/j.cell.2015.10.067

28. Chamorro, A., Dirnagl, U., Urra, X., Planas, A.M.: Neuroprotection in acute stroke: Targeting ex-

citotoxicity, oxidative and nitrosative stress, and inflammation. Lancet Neurol. 15, 869–881 (2016). doi:10.1016/S1474-4422(16)00114-9

29. Hong, H., Kim, B.S., Im, H.I.: Pathophysiological role of neuroinflammation in neurodegenerative diseases and psychiatric disorders. Int Neurourol J. 20, S2–7 (2016). doi:10.5213/inj.1632604.302

30. Sowers, J.L., Johnson, K.M., Conrad, C., Patterson, J.T., Sowers, L.C.: The role of inflammation in brain cancer. Adv Exp Med Biol. 816, 75–105 (2014). doi:10.1007/978-3-0348-0837-8_4

31. Durymanov, M.O., Rosenkranz, A.A., Sobolev, A.S.: Current approaches for improving intratumoral accumulation and distribution of nanomedicines. Theranostics. 5, 1007–20 (2015). doi:10.7150/thno.11742

32. Kannan, R.M., Nance, E., Kannan, S., Tomalia, D.A.: Emerging concepts in dendrimer-based nanomedicine: From design principles to clinical applications. J Intern Med. 276, 579–617 (2014). doi:10.1111/joim.12280

33. Patel, T., Zhou, J., Piepmeier, J.M., Saltzman, W.M.: Polymeric nanoparticles for drug delivery to the central nervous system. Adv Drug Deliv Rev. 64, 701–5 (2012). doi:10.1016/j.addr.2011.12.006

34. Tosi, G., Bortot, B., Ruozi, B., Dolcetta, D., Vandelli, M.A., Forni, F., Severini, G.M.: Potential use of polymeric nanoparticles for drug delivery across the blood-brain barrier. Current Medicinal Chemistry. 20, 2212–2225 (2013)

35. Liu, L., Guo, K., Lu, J., Venkatraman, S.S., Luo, D., Ng, K.C., Ling, E.A., Moochhala, S., Yang, Y.Y.: Biologically active core/shell nanoparticles self-assembled from cholesterol-terminated peg-tat for drug delivery across the blood-brain barrier. Biomaterials. 29, 1509–17 (2008). doi:10.1016/j.biomaterials.2007.11.014

36. Bjugstad, K.B., Redmond, J., D. E., Lampe, K.J., Kern, D.S., Sladek, J., J. R., Mahoney, M.J.: Biocompatibility of peg-based hydrogels in primate brain. Cell Transplant. 17, 409–15 (2008)

37. Aparicio-Blanco, J., Torres-Suarez, A.I.: Glioblastoma multiforme and lipid nanocapsules: A review.

J Biomed Nanotechnol. 11, 1283–311 (2015)

38. Gastaldi, L., Battaglia, L., Peira, E., Chirio, D., Muntoni, E., Solazzi, I., Gallarate, M., Dosio, F.: Solid lipid nanoparticles as vehicles of drugs to the brain: Current state of the art. Eur J Pharm Biopharm. 87, 433–44 (2014). doi:10.1016/j.ejpb.2014.05.004

39. Velasco-Aguirre, C., Morales, F., Gallardo-Toledo, E., Guerrero, S., Giralt, E., Araya, E., Kogan, M.J.: Peptides and proteins used to enhance gold nanoparticle delivery to the brain: Preclinical approaches. Int J Nanomedicine. 10, 4919–36 (2015). doi:10.2147/IJN.S82310

40. Mo, J., He, L., Ma, B., Chen, T.: Tailoring particle size of mesoporous silica nanosystem to antagonize glioblastoma and overcome blood-brain barrier. ACS Appl Mater Interfaces. 8, 6811–25 (2016). doi:10.1021/acsami.5b11730

41. Patchin, E.S., Anderson, D.S., Silva, R.M., Uyeminami, D.L., Scott, G.M., Guo, T., Van Winkle, L.S., Pinkerton, K.E.: Size-dependent deposition, translocation, and microglial activation of inhaled silver nanoparticles in the rodent nose and brain. Environ Health Perspect. (2016). doi:10.1289/EHP234

42. Liu, Y.L., Perillo, E.P., Liu, C., Yu, P., Chou, C.K., Hung, M.C., Dunn, A.K., Yeh, H.C.: Segmentation of 3D trajectories acquired by tsunami microscope: An application to egfr trafficking. Biophysical Journal. 111, 2214–2227 (2016). doi:10.1016/j.bpj.2016.09.041

43. Dilnawaz, F., Sahoo, S.K.: Therapeutic approaches of magnetic nanoparticles for the central nervous system. Drug Discov Today. 20, 1256–64 (2015). doi:10.1016/j.drudis.2015.06.008

44. Paris-Robidas, S., Brouard, D., Emond, V., Parent, M., Calon, F.: Internalization of targeted quantum dots by brain capillary endothelial cells in vivo. J Cereb Blood Flow Metab. 36, 731–42 (2016). doi:10.1177/0271678X15608201

45. Wong, B.S., Yoong, S.L., Jagusiak, A., Panczyk, T., Ho, H.K., Ang, W.H., Pastorin, G.: Carbon nanotubes for delivery of small molecule drugs. Adv Drug Deliv Rev. 65, 1964–2015 (2013). doi:10.1016/j.addr.2013.08.005

46. Kafa, H., Wang, J.T., Rubio, N., Venner, K., Anderson, G., Pach, E., Ballesteros, B., Preston, J.E., Abbott, N.J., Al-Jamal, K.T.: The interaction of carbon nanotubes with an in vitro blood-brain barrier model and mouse brain in vivo. Biomaterials. 53, 437–52 (2015). doi:10.1016/j.biomaterials.2015.02.083

47. Albanese, A., Tang, P.S., Chan, W.C.: The effect of nanoparticle size, shape, and surface chemistry on biological systems. Annu Rev Biomed Eng. 14, 1–16 (2012). doi:10.1146/annurev-bioeng-071811-150124

48. Xu, Q.G., Boylan, N.J., Suk, J.S., Wang, Y.Y., Nance, E.A., Yang, J.C., McDonnell, P.J., Cone, R.A., Duh, E.J., Hanes, J.: Nanoparticle diffusion in, and microrheology of, the bovine vitreous ex vivo. Journal of Controlled Release. 167, 76–84 (2013). doi:10.1016/j.jconrel.2013.01.018

49. Nance, E.A., Woodworth, G.F., Sailor, K.A., Shih, T.Y., Xu, Q., Swaminathan, G., Xiang, D., Eberhart, C., Hanes, J.: A dense poly(ethylene glycol) coating improves penetration of large polymeric nanoparticles within brain tissue. Sci Transl Med. 4, 149ra119 (2012). doi:10.1126/scitranslmed.3003594

50. Mosqueira, A., Camino, P.A., Barrantes, F.J.: Cholesterol modulates acetylcholine receptor diffusion by tuning confinement sojourns and nanocluster stability. Scientific Reports. 8, (2018). doi:ARTN 11974 10.1038/s41598-018-30384-y

51. Li, B., Dou, S.X., Yuan, J.W., Liu, Y.R., Li, W., Ye, F.F., Wang, P.Y., Li, H.: Intracellular transport is accelerated in early apoptotic cells. Proceedings of the National Academy of Sciences of the United States of America. 115, 12118–12123 (2018). doi:10.1073/pnas.1810017115

52. Parveen, N., Borrenberghs, D., Rocha, S., Hendrix, J.: Single viruses on the fluorescence microscope: Imaging molecular mobility, interactions and structure sheds new light on viral replication. Viruses-Basel. 10, (2018). doi:ARTN 250 10.3390/v10050250

53. Zhang, F., Nance, E., Alnasser, Y., Kannan, R., Kannan, S.: Microglial migration and interactions with dendrimer nanoparticles are altered in the presence of neuroinflammation. J Neuroinflammation. 13, 65 (2016). doi:10.1186/s12974-016-0529-3

54. Curtis, C., Toghani, D., Wong, B., Nance, E.: Colloidal stability as a determinant of nanoparticle behavior in the brain. Colloids Surf B Biointerfaces. 170, 673–682 (2018). doi:10.1016/j.colsurfb.2018.06.050

55. James, G., Witten, D., Hastie, T., Tibshirani, R.: An introduction to statistical learning : With applications in r. Springer, New York (2013)

56. Wagner, T., Kroll, A., Haramagatti, C.R., Lipinski, H.G., Wiemann, M.: Classification and segmentation of nanoparticle diffusion trajectories in cellular micro environments. Plos One. 12, (2017). doi:ARTN e0170165 10.1371/journal.pone.0170165

57. Li, D.D., Xiong, J., Qu, A.L., Xu, T.: Three-dimensional tracking of single secretory granules in live pc12 cells. Biophysical Journal. 87, 1991–2001 (2004). doi:10.1529/biophysj.104.043281

58. Helmuth, J.A., Burckhardt, C.J., Koumoutsakos, P., Greber, U.F., Sbalzarini, I.F.: A novel supervised trajectory segmentation algorithm identifies distinct types of human adenovirus motion in host cells. Journal of Structural Biology. 159, 347–358 (2007). doi:10.1016/j.jsb.2007.04.003

59. Dosset, P., Rassam, P., Fernandez, L., Espenel, C., Rubinstein, E., Margeat, E., Milhiet, P.E.: Automatic detection of diffusion modes within biological membranes using back-propagation neural network. Bmc Bioinformatics. 17, (2016). doi:ARTN 197 10.1186/s12859-016-1064-z

60. Naftel, A., Khalid, S.: Motion trajectory learning in the dft-coefficient feature space. In: Fourth ieee international conference on computer vision systems (icvs'06). pp. 47–47. IEEE

61. Chan, K.-P., Fu, A.W.-C.: Efficient time series matching by wavelets. In: Proceedings 15th international conference on data engineering (cat. No. 99CB36337). pp. 126–133. IEEE

62. Keogh, E., Chakrabarti, K., Pazzani, M., Mehrotra, S.: Locally adaptive dimensionality reduction for indexing large time series databases. ACM Sigmod Record. 30, 151–162 (2001)

63. Cai, Y., Ng, R.: Indexing spatio-temporal trajectories with chebyshev polynomials. In: Proceedings of the 2004 acm sigmod international conference on management of data. pp. 599–610. ACM

64. Gowayyed, M.A., Torki, M., Hussein, M.E., El-Saban, M.: Histogram of oriented displacements (hod): Describing trajectories of human joints for action recognition. In: Twenty-third international joint conference on artificial intelligence

65. Li, W., Zhang, Z., Liu, Z.: Action recognition based on a bag of 3d points. In: 2010 ieee computer society conference on computer vision and pattern recognition-workshops. pp. 9–14. IEEE

66. Wang, J., Liu, Z., Wu, Y., Yuan, J.: Mining actionlet ensemble for action recognition with depth cameras. In: 2012 ieee conference on computer vision and pattern recognition. pp. 1290–1297

67. Shah, R., Romijnders, R.: Applying deep learning to basketball trajectories. arXiv preprint arXiv:1608.03793. (2016)

68. Dabiri, S., Heaslip, K.: Inferring transportation modes from gps trajectories using a convolutional neural network. Transportation research part C: emerging technologies. 86, 360–371 (2018)

69. Rausch, K., Reuter, A., Fischer, K., Schmidt, M.: Evaluation of nanoparticle aggregation in human blood serum. Biomacromolecules. 11, 2836–2839 (2010). doi:10.1021/bm100971q

70. Lacerda, S.H.D., Park, J.J., Meuse, C., Pristinski, D., Becker, M.L., Karim, A., Douglas, J.F.: Interaction of gold nanoparticles with common human blood proteins. Acs Nano. 4, 365–379 (2010). doi:10.1021/nn901187

71. Tenzer, S., Docter, D., Kuharev, J., Musyanovych, A., Fetz, V., Hecht, R., Schlenk, F., Fischer, D., Kiouptsi, K., Reinhardt, C., Landfester, K., Schild, H., Maskos, M., Knauer, S.K., Stauber, R.H.: Rapid formation of plasma protein corona critically affects nanoparticle pathophysiology. Nature Nanotechnology. 8, 772–U1000 (2013). doi:10.1038/nnano.2013.181

72. Fornaguera, C., Caldero, G., Mitjans, M., Vinardell, M.P., Solans, C., Vauthier, C.: Interactions of plga nanoparticles with blood components: Protein adsorption, coagulation, activation of the complement system and hemolysis studies. Nanoscale. 7, 6045–6058 (2015). doi:10.1039/c5nr00733j

73. French, R.A., Jacobson, A.R., Kim, B., Isley, S.L., Penn, R.L., Baveye, P.C.: Influence of ionic strength, pH, and cation valence on aggregation kinetics of titanium dioxide nanoparticles. Environmental Science & Technology. 43, 1354–1359 (2009). doi:10.1021/es802628n

74. Chen, K.L., Mylon, S.E., Elimelech, M.: Enhanced aggregation of alginate-coated iron oxide

(hematite) nanoparticles in the presence of calcium, strontium, and barium cations. Langmuir. 23, 5920–5928 (2007). doi:10.1021/la063744k

75. Zensi, A., Begley, D., Pontikis, C., Legros, C., Mihoreanu, L., Wagner, S., Buchel, C., Briesen, H. von, Kreuter, J.: Albumin nanoparticles targeted with apo e enter the cns by transcytosis and are delivered to neurones. Journal of Controlled Release. 137, 78–86 (2009). doi:10.1016/j.jconrel.2009.03.002

76. Zensi, A., Begley, D., Pontikis, C., Legros, C., Mihoreanu, L., Buchel, C., Kreuter, J.: Human serum albumin nanoparticles modified with apolipoprotein a-i cross the blood-brain barrier and enter the rodent brain. Journal of Drug Targeting. 18, 842–848 (2010). doi:10.3109/10611861x.2010.513712

77. Gulyaev, A.E., Gelperina, S.E., Skidan, I.N., Antropov, A.S., Kivman, G.Y., Kreuter, J.: Significant transport of doxorubicin into the brain with polysorbate 80-coated nanoparticles. Pharmaceutical Research. 16, 1564–1569 (1999). doi:Doi 10.1023/A:1018983904537

78. Zhang, F., Nance, E., Zhang, Z., Jasty, V., Kambhampati, S.P., Mishra, M.K., Burd, I., Romero, R., Kannan, S., Kannan, R.M.: Surface functionality affects the biodistribution and microglia-targeting of intra-amniotically delivered dendrimers. Journal of Controlled Release. 237, 61–70 (2016). doi:10.1016/j.jconrel.2016.06.046

79. Kolhar, P., Anselmo, A.C., Gupta, V., Pant, K., Prabhakarpandian, B., Ruoslahti, E., Mitragotri, S.: Using shape effects to target antibody-coated nanoparticles to lung and brain endothelium. Proceedings of the National Academy of Sciences of the United States of America. 110, 10753–10758 (2013). doi:10.1073/pnas.1308345110

80. Anselmo, A.C., Zhang, M., Kumar, S., Vogus, D.R., Menegatti, S., Helgeson, M.E., Mitragotri, S.: Elasticity of nanoparticles influences their blood circulation, phagocytosis, endocytosis, and targeting. ACS Nano. 9, 3169–77 (2015). doi:10.1021/acsnano.5b00147

81. Bourdenx, M., Daniel, J., Genin, E., Soria, F.N., Blanchard-Desce, M., Bezard, E., Dehay, B.: Nanoparticles restore lysosomal acidification defects: Implications for parkinson and other lysosomal-related diseases. Autophagy. 12, 472–83 (2016). doi:10.1080/15548627.2015.1136769

82. Sharma, R., Kim, S.Y., Sharma, A., Zhang, Z., Kambhampati, S.P., Kannan, S., Kannan, R.M.: Activated microglia targeting dendrimer-minocycline conjugate as therapeutics for neuroinflammation. Bioconjug Chem. 28, 2874–2886 (2017). doi:10.1021/acs.bioconjchem.7b00569

83. Nance, E., Kambhampati, S.P., Smith, E.S., Zhang, Z., Zhang, F., Singh, S., Johnston, M.V., Kannan, R.M., Blue, M.E., Kannan, S.: Dendrimer-mediated delivery of n-acetyl cysteine to microglia in a mouse model of rett syndrome. J Neuroinflammation. 14, 252 (2017). doi:10.1186/s12974-017-1004-5

84. Thorne, R.G., Nicholson, C.: In vivo diffusion analysis with quantum dots and dextrans predicts the width of brain extracellular space. Proc Natl Acad Sci U S A. 103, 5567–72 (2006). doi:10.1073/pnas.0509425103

85. Chaturbedy, P., Kumar, M., Salikolimi, K., Das, S., Sinha, S.H., Chatterjee, S., Suma, B.S., Kundu, T.K., Eswaramoorthy, M.: Shape-directed compartmentalized delivery of a nanoparticle-conjugated small-molecule activator of an epigenetic enzyme in the brain. J Control Release. 217, 151–9 (2015). doi:10.1016/j.jconrel.2015.08.043

86. Walters, R., Medintz, I.L., Delehanty, J.B., Stewart, M.H., Susumu, K., Huston, A.L., Dawson, P.E., Dawson, G.: The role of negative charge in the delivery of quantum dots to neurons. ASN Neuro. 7, (2015). doi:10.1177/1759091415592389

87. Kreuter, J., Petrov, V.E., Kharkevich, D.A., Alyautdin, R.N.: Influence of the type of surfactant on the analgesic effects induced by the peptide dalargin after its delivery across the blood-brain barrier using surfactant-coated nanoparticles. Journal of Controlled Release. 49, 81–87 (1997). doi:Doi 10.1016/S0168-3659(97)00061-8

88. Siesjo, B.K.: Calcium in the brain under physiological and pathological conditions. Eur Neurol. 30 Suppl 2, 3–9; discussion 39–41 (1990). doi:10.1159/000117184

89. Berridge, M.J.: Neuronal calcium signaling. Neuron. 21, 13–26 (1998)

90. Wood, J.H.: Neurobiology of cerebrospinal fluid. Plenum Press, New York (1980)

91. Monopoli, M.P., Aberg, C., Salvati, A., Dawson, K.A.: Biomolecular coronas provide the biological identity of nanosized materials. Nat Nanotechnol. 7, 779–86 (2012). doi:10.1038/nnano.2012.207

92. Immordino, M.L., Dosio, F., Cattel, L.: Stealth liposomes: Review of the basic science, rationale, and clinical applications, existing and potential. Int J Nanomedicine. 1, 297–315 (2006)

93. Bhattacharjee, S.: DLS and zeta potential - what they are and what they are not? J Control Release. 235, 337–351 (2016). doi:10.1016/j.jconrel.2016.06.017

94. Napper, D.H.: Steric stabilization. Journal of Colloid and Interface Science. 58, 390–407 (1977). doi:Doi 10.1016/0021-9797(77)90150-3

95. Milhorat, T.H.: The third circulation revisited. J Neurosurg. 42, 628–45 (1975). doi:10.3171/jns.1975.42.6.0628

96. Abbott, N.: Comparative physiology of the blood-brain barrier. In: Physiology and pharmacology of the blood-brain barrier. pp. 371–396. Springer (1992)

97. Gareri, P., Mattace, R., Nava, F., De Sarro, G.: Role of calcium in brain aging. Gen Pharmacol. 26, 1651–7 (1995)

98. Bito, L.Z., Davson, H.: Local variations in cerebrospinal fluid composition and its relationship to the composition of the extracellular fluid of the cortex. Exp Neurol. 14, 264–80 (1966)

99. Thibault, O., Gant, J.C., Landfield, P.W.: Expansion of the calcium hypothesis of brain aging and alzheimer's disease: Minding the store. Aging Cell. 6, 307–17 (2007). doi:10.1111/j.1474-9726.2007.00295.x

100. Nilsson, P., Laursen, H., Hillered, L., Hansen, A.J.: Calcium movements in traumatic brain injury: The role of glutamate receptor-operated ion channels. J Cereb Blood Flow Metab. 16, 262–70 (1996). doi:10.1097/00004647-199603000-00011

101. Michaelis, M.L., Foster, C.T., Jayawickreme, C.: Regulation of calcium levels in brain tissue from adult and aged rats. Mech Ageing Dev. 62, 291–306 (1992)

102. Nicholson, C.: Interaction between diffusion and michaelis-menten uptake of dopamine after

iontophoresis in striatum. Biophysical Journal. 68, 1699–1715 (1995). doi:Doi 10.1016/S0006-3495(95)80348-6

103. Fairless, R., Williams, S.K., Diem, R.: Dysfunction of neuronal calcium signalling in neuroinflammation and neurodegeneration. Cell Tissue Res. 357, 455–62 (2014). doi:10.1007/s00441-013-1758-8

104. Bezprozvanny, I., Hayden, M.R.: Deranged neuronal calcium signaling and huntington disease. Biochem Biophys Res Commun. 322, 1310–7 (2004). doi:10.1016/j.bbrc.2004.08.035

105. Zhang, Y., Chen, Y., Westerhoff, P., Crittenden, J.: Impact of natural organic matter and divalent cations on the stability of aqueous nanoparticles. Water Res. 43, 4249–57 (2009). doi:10.1016/j.watres.2009.06.005

106. Pavlov, M., Siegbahn, P.E.M., Sandstrom, M.: Hydration of beryllium, magnesium, calcium, and zinc ions using density functional theory. Journal of Physical Chemistry A. 102, 219–228 (1998). doi:DOI 10.1021/jp972072r

107. Deerfield, D.W., Lapadat, M.A., Spremulli, L.L., Hiskey, R.G., Pedersen, L.G.: The role of hydrated divalent metal-ions in the bridging of 2 anionic groups - an abinitio quantum chemical and molecular mechanics study of dimethyl-phosphate and formate bridged by calcium and magnesium-ions. Journal of Biomolecular Structure & Dynamics. 6, 1077–1091 (1989). doi:Doi 10.1080/07391102.1989.10506538

108. Wang, D.W., Tejerina, B., Lagzi, I., Kowalczyk, B., Grzybowski, B.A.: Bridging interactions and selective nanoparticle aggregation mediated by monovalent cations. Acs Nano. 5, 530–536 (2011). doi:10.1021/nn1025252

109. Oncsik, T., Trefalt, G., Borkovec, M., Szilagyi, I.: Specific ion effects on particle aggregation induced by monovalent salts within the hofmeister series. Langmuir. 31, 3799–3807 (2015). doi:10.1021/acs.langmuir.5b00225

110. Zyuzin, M.V., Honold, T., Carregal-Romero, S., Kantner, K., Karg, M., Parak, W.J.: Influence of temperature on the colloidal stability of polymer-coated gold nanoparticles in cell culture media.

Small. 12, 1723–1731 (2016). doi:10.1002/smll.201503232

111. Fatehah, M.O., Aziz, H.A., Stoll, S.: Stability of zno nanoparticles in solution. Influence of pH, dissolution, aggregation and disaggregation effects. Journal of Colloid Science and Biotechnology. 3, 75–84 (2014)

112. Schuster, B.S., Ensign, L.M., Allan, D.B., Suk, J.S., Hanes, J.: Particle tracking in drug and gene delivery research: State-of-the-art applications and methods. Advanced Drug Delivery Reviews. 91, 70–91 (2015). doi:10.1016/j.addr.2015.03.017

113. Gillies, G.T., Smith, J.H., Humphrey, J.A., Broaddus, W.C.: Positive pressure infusion of therapeutic agents into brain tissues: Mathematical and experimental simulations. Technol Health Care. 13, 235–43 (2005)

114. Yang, H.T., Balhoff, M.T.: Pore-network modeling of particle retention in porous media. Aiche Journal. 63, 3118–3131 (2017). doi:10.1002/aic.15593

115. Yoon, J.S., Germaine, J.T., Culligan, P.J.: Visualization of particle behavior within a porous medium: Mechanisms for particle filtration and retardation during downward transport. Water Resources Research. 42, (2006). doi:Artn W06417 10.1029/2004wr003660

116. Pernodet, N., Maaloum, M., Tinland, B.: Pore size of agarose gels by atomic force microscopy. Electrophoresis. 18, 55–58 (1997). doi:DOI 10.1002/elps.1150180111

117. Wylie, R.G., Ahsan, S., Aizawa, Y., Maxwell, K.L., Morshead, C.M., Shoichet, M.S.: Spatially controlled simultaneous patterning of multiple growth factors in three-dimensional hydrogels. Nature Materials. 10, 799–806 (2011). doi:10.1038/Nmat3101

118. DeForest, C.A., Anseth, K.S.: Advances in bioactive hydrogels to probe and direct cell fate. Annual Review of Chemical and Biomolecular Engineering, Vol 3. 3, 421–444 (2012). doi:10.1146/annurev-chembioeng-062011-080945

119. Zhang, Y.S., Khademhosseini, A.: Advances in engineering hydrogels. Science. 356, (2017).

doi:ARTN eaaf3627 10.1126/science.aaf3627

120. DeForest, C.A., Anseth, K.S.: Photoreversible patterning of biomolecules within click-based hydrogels. Angewandte Chemie-International Edition. 51, 1816–1819 (2012). doi:10.1002/anie.201106463

121. DeForest, C.A., Anseth, K.S.: Cytocompatible click-based hydrogels with dynamically tunable properties through orthogonal photoconjugation and photocleavage reactions. Nature Chemistry. 3, 925–931 (2011). doi:10.1038/Nchem.1174

122. Albanese, A., Chan, W.C.W.: Effect of gold nanoparticle aggregation on cell uptake and toxicity. Acs Nano. 5, 5478–5489 (2011). doi:10.1021/nn2007496

123. Breunig, M., Bauer, S., Goefferich, A.: Polymers and nanoparticles: Intelligent tools for intracellular targeting? European Journal of Pharmaceutics and Biopharmaceutics. 68, 112–128 (2008). doi:10.1016/j.ejpb.2007.06.010

124. Casey, J.R., Grinstein, S., Orlowski, J.: Sensors and regulators of intracellular pH. Nature Reviews Molecular Cell Biology. 11, 50–61 (2010). doi:10.1038/nrm2820

125. Brini, M., Cali, T., Ottolini, D., Carafoli, E.: Neuronal calcium signaling: Function and dysfunction. Cell Mol Life Sci. 71, 2787–814 (2014). doi:10.1007/s00018-013-1550-7

126. Davis, M.E., Chen, Z.G., Shin, D.M.: Nanoparticle therapeutics: An emerging treatment modality for cancer. Nat Rev Drug Discov. 7, 771–82 (2008). doi:10.1038/nrd2614

127. Bobo, D., Robinson, K.J., Islam, J., Thurecht, K.J., Corrie, S.R.: Nanoparticle-based medicines: A review of fda-approved materials and clinical trials to date. Pharm Res. 33, 2373–87 (2016). doi:10.1007/s11095-016-1958-5

128. Song, E., Gaudin, A., King, A.R., Seo, Y.E., Suh, H.W., Deng, Y., Cui, J., Tietjen, G.T., Huttner, A., Saltzman, W.M.: Surface chemistry governs cellular tropism of nanoparticles in the brain. Nat Commun. 8, 15322 (2017). doi:10.1038/ncomms15322

129. Duncan, G.A., Bevan, M.A.: Computational design of nanoparticle drug delivery systems for selec-

tive targeting. Nanoscale. 7, 15332–40 (2015). doi:10.1039/c5nr03691g

130. Siepmann, J., Gopferich, A.: Mathematical modeling of bioerodible, polymeric drug delivery systems. Adv Drug Deliv Rev. 48, 229–47 (2001)

131. Tseng, Y., Kole, T.P., Wirtz, D.: Micromechanical mapping of live cells by multiple-particle-tracking microrheology. Biophys J. 83, 3162–76 (2002). doi:10.1016/S0006-3495(02)75319-8

132. Yildiz, H.M., McKelvey, C.A., Marsac, P.J., Carrier, R.L.: Size selectivity of intestinal mucus to diffusing particulates is dependent on surface chemistry and exposure to lipids. J Drug Target. 23, 768–74 (2015). doi:10.3109/1061186X.2015.1086359

133. Lai, S.K., O'Hanlon, D.E., Harrold, S., Man, S.T., Wang, Y.Y., Cone, R., Hanes, J.: Rapid transport of large polymeric nanoparticles in fresh undiluted human mucus. Proc Natl Acad Sci U S A. 104, 1482–7 (2007). doi:10.1073/pnas.0608611104

134. Wolak, D.J., Thorne, R.G.: Diffusion of macromolecules in the brain: Implications for drug delivery. Mol Pharm. 10, 1492–504 (2013). doi:10.1021/mp300495e

135. Schuster, B.S., Suk, J.S., Woodworth, G.F., Hanes, J.: Nanoparticle diffusion in respiratory mucus from humans without lung disease. Biomaterials. 34, 3439–46 (2013). doi:10.1016/j.biomaterials.2013.01.064

136. Jokerst, J.V., Lobovkina, T., Zare, R.N., Gambhir, S.S.: Nanoparticle pegylation for imaging and therapy. Nanomedicine (Lond). 6, 715–28 (2011). doi:10.2217/nnm.11.19

137. Li, H.-J., Du, J.-Z., Du, X.-J., Xu, C.-F., Sun, C.-Y., Wang, H.-X., Cao, Z.-T., Yang, X.-Z., Zhu, Y.-H., Nie, S., others: Stimuli-responsive clustered nanoparticles for improved tumor penetration and therapeutic efficacy. Proceedings of the National Academy of Sciences. 113, 4164–4169 (2016)

138. Nance, E.: Brain-penetrating nanoparticles for analysis of the brain microenvironment. Methods Mol Biol. 1570, 91–104 (2017). doi:10.1007/978-1-4939-6840-4_6

139. Monopoli, M.P., Walczyk, D., Campbell, A., Elia, G., Lynch, I., Bombelli, F.B., Dawson, K.A.: Physical-chemical aspects of protein corona: Relevance to in vitro and in vivo biological impacts of

nanoparticles. J Am Chem Soc. 133, 2525–34 (2011). doi:10.1021/ja107583h

140. Lesniak, A., Fenaroli, F., Monopoli, M.P., Aberg, C., Dawson, K.A., Salvati, A.: Effects of the presence or absence of a protein corona on silica nanoparticle uptake and impact on cells. ACS Nano. 6, 5845–57 (2012). doi:10.1021/nn300223w

141. Ehrenberg, M.S., Friedman, A.E., Finkelstein, J.N., Oberdorster, G., McGrath, J.L.: The influence of protein adsorption on nanoparticle association with cultured endothelial cells. Biomaterials. 30, 603–10 (2009). doi:10.1016/j.biomaterials.2008.09.050

142. Lesniak, A., Salvati, A., Santos-Martinez, M.J., Radomski, M.W., Dawson, K.A., Aberg, C.: Nanoparticle adhesion to the cell membrane and its effect on nanoparticle uptake efficiency. J Am Chem Soc. 135, 1438–44 (2013). doi:10.1021/ja309812z

143. Chen, Z.J., Gillies, G.T., Broaddus, W.C., Prabhu, S.S., Fillmore, H., Mitchell, R.M., Corwin, F.D., Fatouros, P.P.: A realistic brain tissue phantom for intraparenchymal infusion studies. J Neurosurg. 101, 314–22 (2004). doi:10.3171/jns.2004.101.2.0314

144. Streitberger, K.J., Sack, I., Krefting, D., Pfuller, C., Braun, J., Paul, F., Wuerfel, J.: Brain viscoelasticity alteration in chronic-progressive multiple sclerosis. PLoS One. 7, e29888 (2012). doi:10.1371/journal.pone.0029888

145. Sack, I., Beierbach, B., Wuerfel, J., Klatt, D., Hamhaber, U., Papazoglou, S., Martus, P., Braun, J.: The impact of aging and gender on brain viscoelasticity. Neuroimage. 46, 652–7 (2009). doi:10.1016/j.neuroimage.2009.02.040

146. Amsden, B.: An obstruction-scaling model for diffusion in homogeneous hydrogels. Macromolecules. 32, 874–879 (1999). doi:DOI 10.1021/ma980922a

147. Verma, A., Stellacci, F.: Effect of surface properties on nanoparticle-cell interactions. Small. 6, 12–21 (2010). doi:10.1002/smll.200901158

148. Wicki, A., Witzigmann, D., Balasubramanian, V., Huwyler, J.: Nanomedicine in cancer ther-

apy: Challenges, opportunities, and clinical applications. J Control Release. 200, 138–57 (2015). doi:10.1016/j.jconrel.2014.12.030

149. Brannon-Peppas, L., Blanchette, J.O.: Nanoparticle and targeted systems for cancer therapy. Adv Drug Deliv Rev. 56, 1649–59 (2004). doi:10.1016/j.addr.2004.02.014

150. Kreuter, J.: Nanoparticulate systems for brain delivery of drugs. Adv Drug Deliv Rev. 47, 65–81 (2001)

151. Chithrani, B.D., Ghazani, A.A., Chan, W.C.: Determining the size and shape dependence of gold nanoparticle uptake into mammalian cells. Nano Lett. 6, 662–8 (2006). doi:10.1021/nl0523960

152. Arvizo, R.R., Miranda, O.R., Thompson, M.A., Pabelick, C.M., Bhattacharya, R., Robertson, J.D., Rotello, V.M., Prakash, Y.S., Mukherjee, P.: Effect of nanoparticle surface charge at the plasma membrane and beyond. Nano Lett. 10, 2543–8 (2010). doi:10.1021/nl101140t

153. Saha, K., Kim, S.T., Yan, B., Miranda, O.R., Alfonso, F.S., Shlosman, D., Rotello, V.M.: Surface functionality of nanoparticles determines cellular uptake mechanisms in mammalian cells. Small. 9, 300–305 (2013). doi:10.1002/smll.201201129

154. He, C., Hu, Y., Yin, L., Tang, C., Yin, C.: Effects of particle size and surface charge on cellular uptake and biodistribution of polymeric nanoparticles. Biomaterials. 31, 3657–66 (2010). doi:10.1016/j.biomaterials.2010.01.065

155. Huang, X., Li, L., Liu, T., Hao, N., Liu, H., Chen, D., Tang, F.: The shape effect of mesoporous silica nanoparticles on biodistribution, clearance, and biocompatibility in vivo. ACS Nano. 5, 5390–9 (2011). doi:10.1021/nn200365a

156. Frohlich, E.: The role of surface charge in cellular uptake and cytotoxicity of medical nanoparticles. Int J Nanomedicine. 7, 5577–91 (2012). doi:10.2147/IJN.S36111

157. Kim, S.T., Saha, K., Kim, C., Rotello, V.M.: The role of surface functionality in determining nanoparticle cytotoxicity. Acc Chem Res. 46, 681–91 (2013). doi:10.1021/ar3000647

158. Gref, R., Luck, M., Quellec, P., Marchand, M., Dellacherie, E., Harnisch, S., Blunk, T., Muller, R.H.: 'Stealth' corona-core nanoparticles surface modified by polyethylene glycol (peg): Influences of the corona (peg chain length and surface density) and of the core composition on phagocytic uptake and plasma protein adsorption. Colloids Surf B Biointerfaces. 18, 301–313 (2000)

159. Liu, Y., Hu, Y., Huang, L.: Influence of polyethylene glycol density and surface lipid on pharmacokinetics and biodistribution of lipid-calcium-phosphate nanoparticles. Biomaterials. 35, 3027–34 (2014). doi:10.1016/j.biomaterials.2013.12.022

160. Maldiney, T., Richard, C., Seguin, J., Wattier, N., Bessodes, M., Scherman, D.: Effect of core diameter, surface coating, and peg chain length on the biodistribution of persistent luminescence nanoparticles in mice. ACS Nano. 5, 854–62 (2011). doi:10.1021/nn101937h

161. Yang, Q., Jones, S.W., Parker, C.L., Zamboni, W.C., Bear, J.E., Lai, S.K.: Evading immune cell uptake and clearance requires peg grafting at densities substantially exceeding the minimum for brush conformation. Mol Pharm. 11, 1250–8 (2014). doi:10.1021/mp400703d

162. Pozzi, D., Colapicchioni, V., Caracciolo, G., Piovesana, S., Capriotti, A.L., Palchetti, S., De Grossi, S., Riccioli, A., Amenitsch, H., Lagana, A.: Effect of polyethyleneglycol (peg) chain length on the bio-nano-interactions between pegylated lipid nanoparticles and biological fluids: From nanostructure to uptake in cancer cells. Nanoscale. 6, 2782–92 (2014). doi:10.1039/c3nr05559k

163. Hu, Y., Xie, J., Tong, Y.W., Wang, C.H.: Effect of peg conformation and particle size on the cellular uptake efficiency of nanoparticles with the hepg2 cells. J Control Release. 118, 7–17 (2007). doi:10.1016/j.jconrel.2006.11.028

164. Perry, J.L., Reuter, K.G., Kai, M.P., Herlihy, K.P., Jones, S.W., Luft, J.C., Napier, M., Bear, J.E., DeSimone, J.M.: PEGylated print nanoparticles: The impact of peg density on protein binding, macrophage association, biodistribution, and pharmacokinetics. Nano Lett. 12, 5304–10 (2012). doi:10.1021/nl302638g

165. Birjiniuk, A., Billings, N., Nance, E., Hanes, J., Ribbeck, K., Doyle, P.S.: Single particle tracking

reveals spatial and dynamic organization of the e. Coli biofilm matrix. New J Phys. 16, 085014 (2014). doi:10.1088/1367-2630/16/8/085014

166. Sykova, E., Nicholson, C.: Diffusion in brain extracellular space. Physiol Rev. 88, 1277–340 (2008). doi:10.1152/physrev.00027.2007

167. Essa, S., Rabanel, J.M., Hildgen, P.: Characterization of rhodamine loaded peg-g-pla nanoparticles (nps): Effect of poly(ethylene glycol) grafting density. Int J Pharm. 411, 178–87 (2011). doi:10.1016/j.ijpharm.2011.02.039

168. Sofia, S.J., Premnath, V.V., Merrill, E.W.: Poly(ethylene oxide) grafted to silicon surfaces: Grafting density and protein adsorption. Macromolecules. 31, 5059–70 (1998). doi:10.1021/ma9710161

169. Mosqueira, V.C., Legrand, P., Morgat, J.L., Vert, M., Mysiakine, E., Gref, R., Devissaguet, J.P., Barratt, G.: Biodistribution of long-circulating peg-grafted nanocapsules in mice: Effects of peg chain length and density. Pharm Res. 18, 1411–9 (2001)

170. Seneca, S., Simon, J., Weber, C., Ghazaryan, A., Ethirajan, A., Mailaender, V., Morsbach, S., Landfester, K.: How low can you go? Low densities of poly(ethylene glycol) surfactants attract stealth proteins. Macromolecular Bioscience. 18, 1800075 (2018). doi:10.1002/mabi.201800075

171. Natte, K., Friedrich, J.F., Wohlrab, S., Lutzki, J., Klitzing, R. von, Osterle, W., Orts-Gil, G.: Impact of polymer shell on the formation and time evolution of nanoparticle-protein corona. Colloids Surf B Biointerfaces. 104, 213–20 (2013). doi:10.1016/j.colsurfb.2012.11.019

172. Xue, W., Liu, Y., Zhang, N., Yao, Y., Ma, P., Wen, H., Huang, S., Luo, Y., Fan, H.: Effects of core size and peg coating layer of iron oxide nanoparticles on the distribution and metabolism in mice. Int J Nanomedicine. 13, 5719–5731 (2018). doi:10.2147/IJN.S165451

173. Ait Bachir, Z., Huang, Y., He, M., Huang, L., Hou, X., Chen, R., Gao, F.: Effects of peg surface density and chain length on the pharmacokinetics and biodistribution of methotrexate-loaded chitosan nanoparticles. Int J Nanomedicine. 13, 5657–5671 (2018). doi:10.2147/IJN.S167443

174. Yang, C., Gao, S., Dagnaes-Hansen, F., Jakobsen, M., Kjems, J.: Impact of peg chain length on the physical properties and bioactivity of pegylated chitosan/siRNA nanoparticles in vitro and in vivo. ACS Appl Mater Interfaces. 9, 12203–12216 (2017). doi:10.1021/acsami.6b16556

175. Li, Z., Han, X., Zhai, Y., Lian, H., Zhang, D., Zhang, W., Wang, Y., He, Z., Liu, Z., Sun, J.: Critical determinant of intestinal permeability and oral bioavailability of pegylated all trans-retinoic acid prodrug-based nanomicelles: Chain length of poly (ethylene glycol) corona. Colloids Surf B Biointerfaces. 130, 133–40 (2015). doi:10.1016/j.colsurfb.2015.03.036

176. Daou, T.J., Li, L., Reiss, P., Josserand, V., Texier, I.: Effect of poly(ethylene glycol) length on the in vivo behavior of coated quantum dots. Langmuir. 25, 3040–4 (2009). doi:10.1021/la8035083

177. Cheng, D., Wen, Y., Wang, L., An, X., Zhu, X., Ni, Y.: Adsorption of polyethylene glycol (peg) onto cellulose nano-crystals to improve its dispersity. Carbohydr Polym. 123, 157–63 (2015). doi:10.1016/j.carbpol.2015.01.035

178. Xu, Q., Ensign, L.M., Boylan, N.J., Schon, A., Gong, X., Yang, J.C., Lamb, N.W., Cai, S., Yu, T., Freire, E., Hanes, J.: Impact of surface polyethylene glycol (peg) density on biodegradable nanoparticle transport in mucus ex vivo and distribution in vivo. ACS Nano. 9, 9217–27 (2015). doi:10.1021/acsnano.5b03876

179. Curtis, C., Rokem, A., Nance, E.: Journal of Open Source Software. 4, 989 (2019). doi:10.21105/joss.00989

180. Tinevez, J.Y., Perry, N., Schindelin, J., Hoopes, G.M., Reynolds, G.D., Laplantine, E., Bednarek, S.Y., Shorte, S.L., Eliceiri, K.W.: TrackMate: An open and extensible platform for single-particle tracking. Methods. 115, 80–90 (2017). doi:10.1016/j.ymeth.2016.09.016

181. Zimprich, A., Ostereicher, M.A., Becker, L., Dirscherl, P., Ernst, L., Fuchs, H., Gailus-Durner, V., Garrett, L., Giesert, F., Glasl, L., Hummel, A., Rozman, J., Angelis, M.H. de, Vogt-Weisenhorn, D., Wurst, W., Holter, S.M.: Analysis of locomotor behavior in the german mouse clinic. J Neurosci Methods. 300, 77–91 (2018). doi:10.1016/j.jneumeth.2017.05.005